Using Reduced Dimensional Models to Interpret Spectral Signatures of Large Amplitude Motions of OH Bonds

Rachel Huchmala

A dissertation
submitted in partial fulfillment of the
requirements for the degree of

Doctor of Philosophy

University of Washington

2023

Reading Committee:
Anne McCoy, Chair
Stefan Stoll
Sotiris Xantheas

Program Authorized to Offer Degree:
Chemistry

University of Washington

Abstract

Using Reduced Dimensional Models to Interpret Spectral Signatures of Large Amplitude Motions of OH Bonds

Rachel Huchmala

Chair of the Supervisory Committee:
Anne McCoy
Chemistry

Understanding the spectral signatures of hydrogen bonding is an ongoing topic of study in physical chemistry. Determining the origins of these spectral signatures will lead to increased understanding of the underlying physics and couplings associated with hydrogen bonding. This work provides insights into the manifestation of large amplitude motions involving OH bonds in various regions of the vibrational spectrum in order to understand the spectral signatures of hydrogen bonding, using small, gas-phase molecular and protonated clusters of water. Additionally, multiple methods for solving the vibrational Schrödinger equation are used to extract meaningful conclusions from reduced dimensional models.

To start, an adiabatic separation is employed to create a two-dimensional model in order to study the two quanta transition of an OH stretch with the corresponding OO stretching vibration between a hydrogen bonded pair in protonated water clusters with 2-4 water molecules ($H^+(H_2O)_2$ - $H^+(H_2O)_4$). The results of this method are then compared to a full two-dimensional model to assess the validity of the approximation. Both models are used to better understand the origins of the intensity. Experimentally, in this two quanta transition, $H^+(H_2O)_2$ has the largest relative intensity, followed by $H^+(H_2O)_4$, while $H^+(H_2O)_3$ shows no intensity. This work showed that the relative intensity of the OH stretching and OO stretching vibrations reflects the changes in the frequency and anharmonicity of the OH vi-

bration with OO stretch excitation. A conclusion that could only be drawn from the ability to decompose the components of the intensity, allowed by the use of the adiabatic approximation, which shows qualitative agreement with the full two-dimensional model. Ultimately it is found that the direction of the change in the OO stretching frequency upon excitation of the OH stretching frequency is associated with the strength of the ionic hydrogen bond, similar to the effects seen in the frequency of the OH stretching fundamental transition.

Elaborating on this idea, the origins of the intensity of the two quanta transition involving the OH stretch and HOH bend (stretch-bend) within one water molecule are investigated. When looking at the experimental band profiles of the OH stretch and stretch-bend transition, initially they look quite different. The OH stretch transition feature has a strong intensity and its corresponding band contour is symmetric. The stretch-bend band contour is less intense, and has a more constant intensity across the frequency range. Keeping this in mind, the experimental vibrational spectrum of the $H^+(H_2O)_{21}$ cluster was analyzed. Within this cluster it was found the symmetry of the OH stretch transition feature is caused by competing effects. The intensity decreases with hydrogen bond strength, but there is a larger density of transitions in the higher frequency range. Therefore, if one divides the profile of the OH stretch by the calculated intensity of the individual OH stretch transitions within the cluster, the resulting profile is in good agreement with the stretch-bend transition.

Further investigation into the origin of the stretch-bend transition intensity shows that it is driven by electrical anharmonicity, or higher order terms of the dipole moment surface. More specifically, it is found that the quadratic bilinear term of the dipole expansion ($\partial^2\mu/\partial\theta_{\mathrm{HOH}}\partial r_{\mathrm{OH}}$) is the largest contributor to the intensity of the transition. To better understand the origin of the intensity, the change in charge distribution with r_{OH} and θ_{HOH} displacement was investigated. This study showed that when θ_{HOH} is extended the partial charges on the hydrogen atoms generally increase, but this effect is partially cancelled by a decrease in the charge of hydrogen atoms when a hydrogen bond is broken. The extent of

this cancellation increases with hydrogen bond strength, creating the more constant intensity across the stretch-bend transition band contour. Additionally, the mixing of vibrational modes causes near degeneracy splittings therefore leading to the breadth of the stretch-bend region seen in large water clusters and the bulk, but overall it is found that excluding this mixing leads to a similar integrated intensity across the region.

Finally, the assignments of the OH-stretching fundamental and overtone regions (Δv_{OH} = 1–5) of the vibrational spectra of gas phase tert-butyl hydroperoxide (TBHP) are assigned using a reduced dimensional reaction path model. A comparison between theory and experiment illustrates the necessity for treatments that include OH-stretch and COOH torsion (τ) explicitly in order to unravel the spectral features observed in the OH-stretching overtones (Δv_{OH} = 1-5) of TBHP. A linear treatment of the transition dipole moment fails in capturing the intensity of the OH-stretch-torsion features, requiring the incorporation of higher order terms in the expansion of the dipole surface used in reduced dimensions to obtain intensities that agree with experimental findings. This model was extended to the carbon-centered hydroperoxyalkyl radical, becoming a three-dimensional model including the rotation of the CH_2 group (ϕ), which is a result of the loss of the hydrogen atom in the formation of the molecule. Both molecules have a double well potential in the torsion coordinate, and excitation of the OH stretching overtones is complicated by this potential landscape. For TBHP, it was found that the tunneling splitting of the torsion states was large enough to produce multiple transitions to the OH excited states that carried intensity, therefore leading to some of the breadth seen in the spectral regions of these transitions. Although, in the carbon-centered hydroperoxyalkyl radical the torsion potential is no longer symmetric, the tunneling splitting decreases and no evidence was found that the tunnelling doublets were leading to the breadth of the feature.

TABLE OF CONTENTS

LIST OF FIGURES

LIST OF TABLES

ACKNOWLEDGMENTS

The completion of one's doctoral degree is a reflection of their own dedication and perseverance, but I couldn't have done it without guidance and support. I would like to take the time to recognize and thank the people who helped me along this journey.

To my advisor Dr. Anne B. McCoy, thank you for teaching me how to stand up for and believe in myself, while I learned so many things from you I know without these two skills this document would have never been completed. Thank you for teaching me how to pose research questions and answer them. Thank you for being patient with me, along with my allergy to I/O and my need to "give power to big words". I know I am a better scientist and a better person because I had you as a mentor.

To the members of the McCoy Group, past and present, thank you for being so welcoming and kind. Dr. Victor Lee, Dr. Mark Boyer, and Dr. Ryan DiRisio, thank you for your guidance. It is my hope that some of your impact on me is reflected in the work in the following pages but more importantly in the scientist I become. Jacob Finney, thank you for being along for this wild ride with me. I am so grateful to have you as a friend. Yarra Hassan, thank you for dealing with having me as a desk mate while navigating all the stress of your first year. I wouldn't have made it without your secret stash of cookies.

To my family, Paul and Sarah Huchmala, thank you for your unwavering support from however far away and believing in me and this path I chose, especially on the days when I didn't believe in myself.

To everyone I've been grateful to call a friend in the UW Chemistry Department, thank you. Thank you for discovering a new city with me, navigating grad school with me, supporting me in my work and my life, and helping me be more than just a graduate student.

To Dr. Jose Parra, D.O. and Dr. Kayla Christy, D.V.M., thank you for all your support from when we met at Northern Arizona University through us all becoming doctors (although I am not "that kind"). Thank you for teaching me how to work hard and play harder. I am so proud of both of you and hope whatever comes next leads to more time spent together.

To my partner, Robert Hoppe, just thank you. I would never recommend a five year long distance relationship to anyone, but I am so glad that we have made it work. Thank you for all your support, dealing with your flight delays with grace, and learning how to perfectly sync Netflix so we could watch tv together over the phone. I can't wait to do life with you, with less distance.

Finally to my canine companion, Remus, I don't think we will ever know who saved who but I sure am glad you made it so I got to spend the last two years of my PhD taking daily walks and having weekend adventures.

DEDICATION

To my mother, Frances Marie Huchmala, through this and everything that comes of it, may your memory carry on.

Chapter 1

INTRODUCTION

1.1 Hydrogen Bonding

While there is no argument that water is essential to life as we know it, many of the effects of its physical properties are still under debate. Specifically, the anomalous properties of water due to its ability to hydrogen bond. A hydrogen bond is defined as a specific intermolecular dipole-dipole interaction between molecules with hydrogen atoms and molecules with the strong electronegative atoms oxygen, nitrogen, and fluorine. In the bulk, water has complex hydrogen bonding networks, which lead to the most unique properties of water, such as the fact that solid water has a lower density than liquid water. Microscopically, hydrogen bonding is dynamic, creating ever-changing hydrogen bonding networks that facilitate proton-transfer and these constant rearrangements strongly influence on the spectral signatures of water.[7,8] Most often, these networks cause broadening of spectroscopic signatures often convoluting the infrared (IR) region of the electromagnetic spectrum, making identification of other molecules in a sample nearly impossible by IR detection methods. In addition to this, by studying cold gas phase clusters of water, it has been determined that depending on the connectivity of water molecules and if the cluster is charged (by either adding an extra proton or removing one) the frequencies of individual transitions involving the OH stretching vibrational states vary drastically.[9–12] Ultimately, these dynamic interactions keep researchers invested in understanding the structure of water clusters,[13–15] how their structure affects their spectra,[16,17] and how spectra of water clusters can inform the underlying molecular structure.[18–20]

1.2 Modeling Vibrational Spectroscopy in Reduced Dimensional Spaces

With the exponential increase in computational power over the last decade, the possibilities to approach a complex problem are ever-growing. With increased accuracy comes increased computational expense. Striking a balance between accuracy and expense has become essential in theoretical chemistry research. Additionally, these large calculations often return large amounts of data that can make extracting meaningful insights difficult. This has caused researchers to adjust the way they approach problems and determine what the most important outcome of their work is. The goal of the present work is to use simple, strategic approaches to solving the vibrational Schrödinger equation in order to interpret the underlying molecular physics that drives spectroscopic signatures unique to hydrogen bonding networks. We take advantage of lower cost but still accurate electronic structure calculations using second order Møller–Plesset perturbation theory (MP2) and the augmented double and triple zeta Dunning basis sets (aug-cc-pVDZ and aug-cc-pVTZ).[21–23] These basis sets are correlation-consistent, polarized, and valence only. The augmented identifier comes from the addition of diffuse functions which are necessary for accurately describing electrons far from the nucleus but essential to long-range interactions, negative charges and most importantly, hydrogen bonds. This work utilizes the implementation of these methods in the Gaussian program package.[3] Once geometries of the molecules of interest are optimized, potential energy surfaces and dipole surfaces are obtained from electronic structure. Then, multiple methods are used to collect vibrational information.

To simulate a vibrational spectrum, one needs two things: the frequency of the transition and the intensity of that transition. Transition frequencies are the difference between the energy of the ground state and the energy of the excited state of each transition. The intensity of the transition is not as straight forward to calculate and requires the vibrational wave functions of a state as well as the derivatives of the dipole moment. The usual starting point for calculating intensities of vibrational transitions is the linear dipole/harmonic oscillator approximation, which is based on a quadratic potential and a linear expansion of the dipole

surface. This approximation is a reflection of the lowest order non-zero terms in each of the expansions. While this is a good starting point, transitions of more than one quantum of excitation are rigorously zero. In order to calculate multi-quanta transitions, one must include higher order terms (which can also be thought of as anharmonicities) in the potential energy surface (mechanical anharmoncities) or in the dipole function (electrical anharmonicites).[24]

One of the ways to do this is through vibrational perturbation theory. In this method, higher-order terms are added incrementally into the potential and dipole functions.[25] Second-order vibrational perturbation theory (VPT2) is commonly used in quantum chemistry packages, and includes up to cubic terms in the potential energy and quadratic terms in the dipole function.[3,26] In recent work, VPT2 methods were used in determining possible isomers of the protonated water hexamer ($H^+(H_2O)_6$) in the vibrational spectrum of $H^+(H_2O)_6$ and its deuterated analog, $D^+(D_2O)_6$.[27] While these "black box" methods are good for quick calculations and confirmations, they do not provide the flexibility that reduced dimensional models can. In order to examine this, one must first understand the dimensionality of a vibrational model.

The vibrational Hamiltonian of any molecule has $3N_{atoms} - 6$ dimensions as the molecule has $3N_{atoms} - 6$ vibrations, where the N_{atoms} refers to the number of atoms in the molecule. In the harmonic oscillator approximation, the wave function is assumed to be a direct product of $3N_{atoms} - 6$ uncoupled, one-dimensional quantum harmonic oscillators that follow the vibrational normal modes of the system of interest. When looking at an isolated water molecule, using this method in its full dimensionality is not computationally demanding, but it quickly becomes intractable as the number of water molecules, or atoms, one wishes to study increases. Further, the addition of more water molecules introduces the addition of hydrogen bonds, which introduces anharmonicites that cause the harmonic approximation to break down. This work aims to push past the harmonic approximation by focusing on specific transitions of the systems of interest, therefore reducing the dimensionality and allowing for higher order terms in the potential energy and dipole surfaces to be used in the calculation of the spectrum without greatly increasing the computational expense.

1.3 Overview of Work

When two water molecules are hydrogen bonded they form what is called a donor-acceptor pair, where the water molecule that contributes the hydrogen atom is the donor, and the other is the acceptor. The intricacies of the coupling and anharmonicities of the vibrational motions between this donor-acceptor pair is reflected in their spectra. One specific manifestation is in the intensity of the transition to the state with one quantum of excitation in the hydrogen-bound OH stretch and one quantum of excitation in the donor-acceptor OO stretch. Specifically, this transition was investigated in $H^+(H_2O)_2$, $H^+(H_2O)_3$, and $H^+(H_2O)_4$ because experimentally each system shows a different intensity relative to that of the OH stretching transition.[13,28,29] A two-dimensional model was developed to understand the origins of this change in intensity. In addition to this, an adiabatic separation of the high-frequency OH and low-frequency OO stretching vibration was employed in order to create a 1+1 type models. Working in reduced dimensions allowed for several low-order expansions of the dipole surface to be probed.[30] This work also tested the extent to which reduced dimensional models can accurately describe these systems to allow the large cost of a full dimensional calculation to be circumvented in future studies.

Moving to a higher energy region of the vibrational spectrum, the two quanta transition to the state with one quantum of excitation in the OH stretch and another quantum of excitation in the HOH bend (stretch-bend) was investigated next. This region shows a similar spread of transition frequencies to the OH-stretching fundamental region (3000-3800 cm^{-1}), but the two regions show distinctive intensity patterns.[31] These two factors lead to the possibility of characterizing the populations of local hydrogen-bond environments found in larger hydrogen-bonding networks, for example water clusters or clathrate cages. Before studies of this type can be carried out, it is crucial to understand what is causing the intensity in the stretch-bend transitions. An investigation into the changes in the charge distribution across H_2O and $(H_2O)_2$, as the OH bond and HOH angle are displaced is conducted in order to uncover the origins of the intensity. Additionally, the effects of the collective nature of the

OH stretching and HOH bending vibrations are probed to further understand the intensity.

The assignments of the OH-stretching fundamental and overtone regions ($\Delta v_{\mathrm{OH}} = 1$–$5$) of the vibrational spectra of gas phase tert-butyl hydroperoxide (TBHP), collected by experimental collaborators,[4,32] are investigated by reduced dimensional reaction path models developed based on the work of Miller, Handy and Adams.[33] These compounds are abundant in Earth's atmosphere which makes understanding their spectral signatures important for analyzing the composition of Earth's atmosphere as well as subtracting out Earth's atmosphere from ground-based observations of celestial bodies. The models developed contain the OH stretch and COOH torsion explicitly in order to capture the coupling of these motions and their effects on transitions with excitation in the OH stretching vibrations.[34] In addition to the study of TBHP, this model is adapted to study the carbon-centered hydroperoxyalkyl radical, which is formed when a hydrogen atom is removed from one of the methyl groups of TBHP. While these molecules only differ by one atom, the complexity of their vibrational landscapes is much different. Most notably, the potential energy surface as a function of the COOH torsion is a symmetric double well in TBHP, which creates distinctly split tunnelling doublets when calculating the energy levels. In the carbon-centered radical, the loss of the hydrogen atom forms a CH_2 group, which introduces another low-energy torsion into the molecule and breaks the symmetry of the potential along the COOH coordinate.[35]

Chapter 2

EXPLORING THE ORIGINS OF SPECTRAL SIGNATURES OF STRONG HYDROGEN BONDING IN PROTONATED WATER CLUSTERS

Reproduced in part with permission from [Rachel M. Huchmala and Anne B. McCoy. Exploring the Origins of Spectral Signatures of Strong Hydrogen Bonding in Protonated Water Clusters. *J. Phys. Chem. A* **2022**,126 (8), 1360-1368]. Copyright [2022] American Chemical Society.

2.1 Introduction

The vibrational spectrum of a molecule or molecular cluster encodes a vast array of information about the strength of bonds and the effect of the local environment on the bond strength.[14,36–38] If we treat vibrations as harmonic oscillators, and assume that the dipole moment is a linear function of the vibrational coordinates, only the $1 \leftarrow 0$ transition for each of the infrared (IR) active modes can carry intensity. Inclusion of anharmonicity of the individual oscillators or couplings among these oscillators allows for transitions to states with two or more quanta of excitation in one or multiple vibrations. Higher order terms in the dipole moment surface also contribute to the intensity of transitions to excited states. These two contributions are encoding complementary information. The potential provides information about how the forces along one coordinate are affected by the displacement of another vibrational degree of freedom. In contrast, higher order terms in the dipole moment encode information about changes in the charge distribution with vibrational excitation.[39–41] In this study, we explore the contributions of higher order terms in the potential and dipole surfaces to the intensity of combination transitions involving vibrations associated with ionic-

hydrogen bonds and the donor and acceptor oxygen atoms to obtain a clearer picture of what can be learned about the underlying electronic structure from the position and relative intensities of such combination transitions.

The frequency difference between the high frequency OH stretching vibration (r_{O_DH}) and a low-frequency donor/acceptor OO stretching vibration ($R_{O_AO_D}$), illustrated in Figure 2.1, suggests an adiabatic separation of these two vibrations.[13,42] Within this model, the potential coupling between these vibrations is reflected in changes in the potential in the lower frequency vibration upon excitation of the higher frequency one. As earlier studies have shown, the leading contribution to this potential coupling arises from a cubic term in the expansion of the potential, which is linear in the low-frequency vibration and quadratic in the higher frequency one.[43] Within the adiabatic approximation, the introduction of this cubic coupling term leads to a shift in the minimum in the potential along $R_{O_AO_D}$, which depends on the number of quanta of excitation in the O_DH stretching vibration. Within this model, the intensity of transitions to states with excitation in both these stretches can be accounted for within a vibrational Franck-Condon analysis. If the potentials for the two modes are harmonic and the coupling is cubic, the Franck-Condon intensities can be evaluated analytically within the adiabatic approximation.[43] Recent work of Henderson and Jordan[44] explored the role of higher order terms in the potential when describing the couplings between an OH stretch and the in-plane rocking modes of the anion in either $HCO_2^- \cdot (H_2O)$ or $NO_3^- \cdot (H_2O)$. That work showed that a multidimensional adiabatic model was necessary to reproduce the experimental vibrational spectra of these water-ion complexes.

Adiabatic models provide an intuitive approach, and have been shown to anticipate that the observed intensity arises from shifts in the equilibrium $R_{O_AO_D}$ bond length with excitation of the O_DH stretching vibration in $H^+(H_2O)_4$.[13] While this can be the primary source of intensity, a second contribution comes from the change in the transition moment for the OH oscillator as $R_{O_AO_D}$ is adjusted. Such a change is anticipated by the fact that the intensity of the OH vibrational transition increases as the frequency decreases or the hydrogen bond

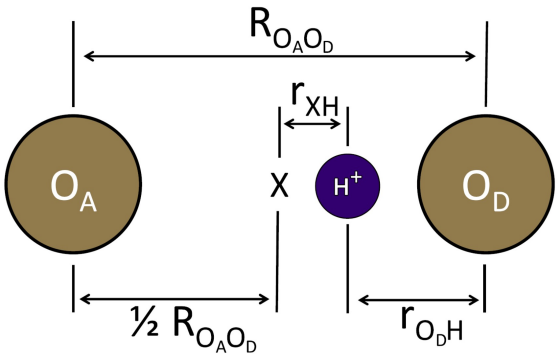

Figure 2.1: Coordinates used in this study.

becomes stronger.[9,11,18,45] This leads us to expect a linear (or higher-order) dependence of the transition moment for the OH oscillator on $R_{\mathrm{O_A O_D}}$. This will not be captured in the vibrational Franck-Condon picture, which assumes a constant transition moment.

In the present study, we explore the roles of higher order terms in the expansion of the dipole moment (electrical anharmonicity) and higher order terms in the expansion of the potential surface (mechanical anharmonicity) in determining the intensity of the combination transition involving the $\mathrm{O_A O_D}$ stretch and the displacement of the shared proton along this axis in strongly hydrogen bonded systems. As examples, we will focus on protonated water clusters with two to four water molecules. These clusters have $\mathrm{O_D H}$ stretching frequencies that vary from 1000 $\mathrm{cm^{-1}}$ to 2600 $\mathrm{cm^{-1}}$.[9,13,28,29,36,46] At the same time, transitions have been assigned by experiment and theory to combinations of the shared proton stretch and the displacement of the donor and acceptor in $\mathrm{H^+(H_2O)_2}$[28,47] and $\mathrm{H^+(H_2O)_4}$,[13,48] but not in the case of $\mathrm{H^+(H_2O)_3}$.

2.2 Theory

The coordinates used to develop the two-dimensional model that is explored in this study are defined as the distance between the oxygen atoms in the donating hydronium molecule and the accepting water molecule, $R_{O_AO_D}$ (referred to as R_{OO} in the following discussion), and the distance between the shared proton and the center of R_{OO}, r_{XH}. As seen in Figure 2.1, r_{XH} is defined such that its value decreases as the proton moves away from O_D and toward O_A. For the purpose of this study, we will focus on two-dimensional cuts through the potentials and dipole surfaces for $H^+(H_2O)_2$, $H^+(H_2O)_3$ and $H^+(H_2O)_4$. Specifically, the electronic energy, evaluated at the MP2/aug-cc-pVDZ level of theory/basis,[49] is minimized under the constraint that O$\cdots$H-O are collinear. Once optimized, a two dimensional scan is performed as a function of R_{OO} and r_{XH}, with all other coordinates constrained to their values in the optimized geometry. We elect to use the XH distance for these scans, rather than the distance between the shared proton and either the donor or acceptor oxygen atom, for two reasons. First, in this coordinate system, there is no kinetic coupling between the two vibrations under consideration. Second, the use of r_{XH} coordinate does not introduce a bias toward the geometries where the excess proton is bound to the donating or accepting oxygen atom. This is particularly important in $H^+(H_2O)_2$, where in the optimized structure the hydrogen atom is nearly at the midpoint between the donor and acceptor oxygen atoms. Also, for a given value of R_{OO} the cuts of the potential along r_{XH}, r_{O_DH}, and r_{O_AH} differ by only constant shift, and are equivalent within the adiabatic treatments described below.

The Hamiltonian for the two dimensional system is

$$H_{2D} = \frac{p_{XH}^2}{2\mu_{H\cdots OO}} + \frac{p_{OO}^2}{2\mu_{OO}} + V(r_{XH}, R_{OO}) \tag{2.1}$$

where μ_{AB} represents the reduced mass of the interacting particles. The associated energies, $E_{n_{XH},n_{OO}}$, and wave functions, $\Psi_{n_{XH},n_{OO}}(R_{OO}, r_{XH})$, are evaluated using several approaches. First, we diagonalize the two-dimensional Hamiltonian directly in a discrete variable repre-

sentation (DVR) on the range from $-\infty$ to ∞, as described by Colbert and Miller.[50] This calculation allows us to assess the impact of approximations on the calculated transition frequencies and intensities, and explore the origins of the intensities of the transition to states with one quantum of excitation in the OH and OO stretch in these ions. The approximations that will be explored include replacing the potential and dipole surfaces with low-order expansions in the displacements of these coordinates from their values in the optimized structures. We will also explore the adiabatic separation of the low frequency OO stretching vibration and the high frequency OH stretching vibration.

In order to determine the effects of higher order terms on the potential, we start by considering a system of two harmonic oscillators, expressed in terms of the displacements of R_{OO} and the $\mathrm{O_DH}$ distance, r_{OH}, from their equilibrium values. In this model, these two oscillators are only coupled through kinetic coupling terms as

$$H_{\mathrm{HO}} = \frac{p_{\mathrm{OH}}^2}{2\mu_{\mathrm{OH}}} + \frac{p_{\mathrm{OO}}^2}{2\mu_{\mathrm{OO}}} - \frac{p_{\mathrm{OH}}P_{\mathrm{OO}}}{m_{\mathrm{O}}} + \frac{F_{rr}}{2}\Delta r_{\mathrm{OH}}^2 + \frac{F_{RR}}{2}\Delta R_{\mathrm{OO}}^2 \tag{2.2}$$

where F_{RR} and F_{rr} are the quadratic force constants in the R_{OO} and r_{OH} respectively. Re-expressing this Hamiltonian in terms of the ΔR_{OO} and Δr_{XH} coordinates used in this study, the Hamiltonian becomes

$$H_{\mathrm{HO}} = \frac{p_{\mathrm{XH}}^2}{2\mu_{\mathrm{H\cdots OO}}} + \frac{p_{\mathrm{OO}}^2}{2\mu_{\mathrm{OO}}} + \frac{1}{2}(F_{RR} + \frac{1}{4}F_{rr})\Delta R_{\mathrm{OO}}^2 + \frac{1}{2}F_{rr}\Delta r_{\mathrm{XH}}^2 - \frac{1}{2}F_{rr}\Delta R_{\mathrm{OO}}\Delta r_{\mathrm{XH}} \tag{2.3}$$

In the discussion that follows, we will refer to this Hamiltonian as the harmonic model.

This model can be extended by introducing the lowest-order terms that could be responsible for the coupling between the high and low-frequency vibrations, specifically the $1/2F_{rrR}\Delta r^2\Delta R$ term in the expansion of the potential. The introduction of this cubic coupling term leads to a shift in the high frequency mode that is proportional to the displacement of the lower frequency vibrational coordinate. This analysis will be performed in Δr_{OH} and ΔR_{OO}. As the kinetic coupling between these two vibrations in Equation 2.2 leads

to a small shift in the harmonic frequencies of these two vibrations, it will not be considered in this analysis. This model was described by Myshakin *et al.*[43] and further explored by Hamm and Stock[51] and Relph *et al.*[52] We have applied this model to studies of complexes of nitrate and formate ion with water[53,54] and $H_2OCH^+ \cdot Ar$.[55] In this approach, the Hamiltonian is expressed in terms of dimensionless coordinates, $q = \sqrt{\hbar/\mu_{OH}\omega_{OH}}\,\Delta r_{OH}$ and $Q = \sqrt{\hbar/\mu_{OO}\omega_{OO}}\,\Delta R_{OO}$ with $\lambda = \omega_{OH}\mu_{OH}F_{rrR}\sqrt{\mu_{OO}\omega_{OO}/\hbar^3}$.

$$H_{\text{cubic}} = \frac{\omega_{OH}}{2}\left[p^2 + \left(1 + \frac{\lambda}{\omega_{OH}}Q\right)q^2\right] + \frac{\omega_{OO}}{2}\left(P^2 + Q^2\right) \tag{2.4}$$

Analysis of this model within an adiabatic treatment, and expanding the energies to first order in λ/ω_{OH} results in analytical expressions for the energies in cm^{-1},

$$E_{n_{OH},n_{OO}} = \omega_{OH}\left(n_{OH} + \frac{1}{2}\right) + \omega_{OO}\left(n_{OO} + \frac{1}{2}\right) - \frac{\lambda^2}{8\omega_{OO}}\left(n_{OH} + \frac{1}{2}\right)^2 \tag{2.5}$$

and the Franck-Condon intensities for the transition to states with one quantum in the OH stretch and n_{OO} quanta of excitation in the OO stretch

$$I \propto \left(\omega_{OH} - \frac{\lambda^2}{32\omega_{OO}} + n_{OO}\omega_{OO}\right)\left(\frac{\exp\left[-\Delta Q_{n_{OH}}^2/2\right]\left(\Delta Q_{n_{OH}}\right)^{2n_{OO}}}{2^{n_{OO}}\left(n_{OO}\right)!}\right) \tag{2.6}$$

where

$$\Delta Q_{n_{OH}} = -\frac{\lambda n_{OH}}{2\omega_{OO}} \tag{2.7}$$

For the purpose of the discussion that follows, we will refer to this model as the harmonic adiabatic model.[43] Additionally, we present the values of the parameters for the harmonic and harmonic adiabatic models in Table 2.1.

Table 2.1: Parameters used in harmonic and harmonic adiabatic calculations. Dipole derivatives are taken at the minimum of the potential energy surface and are listed in Debye Bohr^{-1} or Debye Bohr^{-2} and frequencies and λ in cm^{-1}.

	$H^+(H_2O)_4$	$H^+(H_2O)_3$	$H^+(H_2O)_2$
$\frac{\partial \mu_x}{\partial r_{\mathrm{XH}}}$	-3.51	-3.99	-5.10
$\frac{\partial \mu_x^2}{\partial r_{\mathrm{XH}}^2}$	3.88	3.84	-0.04
$\frac{\partial \mu_y}{\partial r_{\mathrm{XH}}}$	0.31	0.35	0.08
$\frac{\partial \mu_y^2}{\partial r_{\mathrm{XH}}^2}$	-0.27	-0.34	-0.01
$\frac{\partial \mu_z}{\partial r_{\mathrm{XH}}}$	-0.11	0.14	-0.17
$\frac{\partial \mu_z^2}{\partial r_{\mathrm{XH}}^2}$	0.14	-0.07	-0.006
ω_{OO} [a]	362.3	413.5	-
ω_{OH} [a]	2909.4	2525.5	-
λ	101.5	103.1	-

[a] Harmonic frequencies obtained from the second derivative at the minimum of the corresponding one dimensional potential.

We can also apply the adiabatic approximation to the solution of H_{2D} in eq 2.1. In this approach, we define

$$h_{\mathrm{XH}}(R_{\mathrm{OO}}) = \frac{p_{\mathrm{XH}}^2}{2\mu_{\mathrm{H\cdots OO}}} + V(r_{\mathrm{XH}}, R_{\mathrm{OO}}) \tag{2.8}$$

and solve

$$h_{\mathrm{XH}}(R_{\mathrm{OO}})\psi_{n_{\mathrm{XH}}}(r_{\mathrm{XH}}; R_{\mathrm{OO}}) = \epsilon_{n_{\mathrm{XH}}}(R_{\mathrm{OO}})\psi_{n_{\mathrm{XH}}}(r_{\mathrm{XH}}; R_{\mathrm{OO}}) \tag{2.9}$$

The Hamiltonian for the OO stretch becomes

$$\left[\frac{p_{\mathrm{OO}}^2}{2\mu_{\mathrm{OO}}} + \epsilon_{n_{\mathrm{XH}}}(R_{\mathrm{OO}})\right]\phi_{n_{\mathrm{OO}}}^{(n_{\mathrm{XH}})}(R_{\mathrm{OO}}) = E_{n_{\mathrm{XH}},n_{\mathrm{OO}}}^{(ad)}\phi_{n_{\mathrm{OO}}}^{(n_{\mathrm{XH}})}(R_{\mathrm{OO}}) \tag{2.10}$$

and wave functions, $\Psi_{n_{\mathrm{XH}},n_{\mathrm{OO}}}(R_{\mathrm{OO}}, r_{\mathrm{XH}})$ are approximated by

$$\Psi_{n_{\mathrm{XH}},n_{\mathrm{OO}}}^{(ad)}(R_{\mathrm{OO}}, r_{\mathrm{XH}}) = \psi_{n_{\mathrm{XH}}}(r_{\mathrm{XH}}; R_{\mathrm{OO}})\phi_{n_{\mathrm{OO}}}^{(n_{\mathrm{XH}})}(R_{\mathrm{OO}}) \tag{2.11}$$

Within this approximation,

$$I \propto \nu_{n_{\mathrm{XH}},n_{\mathrm{OO}}\leftarrow 0}\left|\langle\phi_0^{(0)}|\,\vec{f}_{0,n_{\mathrm{XH}}}\,|\phi_{n_{\mathrm{OO}}}^{(n_{\mathrm{XH}})}\rangle\right|^2 \tag{2.12}$$

where $\nu_{n_{\mathrm{XH}},n_{\mathrm{OO}}\leftarrow 0}$ is the transition frequency and

$$\vec{f}_{0,n_{\mathrm{XH}}} = \langle\psi_0|\,\vec{\mu}\,|\psi_{n_{\mathrm{XH}}}\rangle \tag{2.13}$$

is the transition moment in the XH stretch. Within the vibrational Franck-Condon approximation, $\vec{f}_{0,n_{\mathrm{XH}}}$ is taken to be a constant.

In order to investigate which terms in the dipole surface provide the primary contribution to the observed intensity, the intensities are calculated using the Franck-Condon approximation, the full dipole moment surface and polynomial expansions of the dipole moment about the equilibrium configuration in Δr_{XH}. All of these dipoles are rotated to the axes shown in

Figure 2.2, such that the O_D-H$\cdots O_A$ lies along the x-axis.

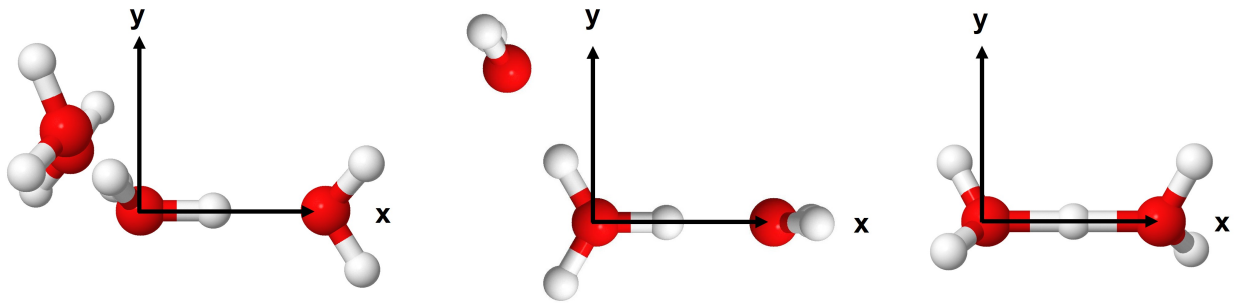

Figure 2.2: Structures and orientation of $H^+(H_2O)_4$, $H^+(H_2O)_3$, and $H^+(H_2O)_2$ used in this study. In all cases the structures are optimized with the constraint that the O_D-H$\cdots O_A$ angle is 180°, and aligned along the x-axis. In $H^+(H_2O)_3$ all three oxygen atoms are in the xy plane, while in $H^+(H_2O)_4$, the bisector of the OO_DO angle is in the xy plane.

2.3 Results & Discussion

Much of the discussion that follows will focus on the ratio of the intensity of the combination band involving excitation in both the OO stretch and the hydrogen-bonded OH stretch, OH + OO, to the intensity of the transition to the $n_{OH} = 1$ level of the OH stretch,

$$\rho_{OO} = \left(\frac{I_{OH+OO}}{I_{OH}} \right) \times 100 \tag{2.14}$$

Before exploring the origins of the intensity in this combination band, how it is affected by the environment, and how this is captured by the approximations described in the previous section, it is useful to review what is seen in the experimental spectra.

The experimental spectrum, obtained by jet cooled predissociation IR, of $H^+(H_2O)_4$[13,46] contains a strong, broad peak at 2650 cm^{-1}, which has been assigned to the transition to the state with one quantum of excitation in the hydrogen-bonded OH stretch in the hydronium core. The spectrum also contains a weaker broad feature that is centered at 3017 cm^{-1}.

Experimental work in the terahertz region by Esser *et al.*[56] identifies the transition to the state with one quantum of excitation in the OO stretch of interest at 316 cm^{-1}. Comparing this frequency to the 367 cm^{-1} splitting between the features at 3017 and 2650 cm^{-1}, Doung *et al.*[13] assigned the feature at 3017 cm^{-1} to the OH + OO transition. Indeed such a transition is predicted to have a large intensity based on the VPT2 calculation.

In $H^+(H_2O)_3$ the feature that has been assigned to the transition to the state with one quantum of excitation in the hydrogen-bonded OH stretch, which is centered at 2066 cm^{-1}, is more structured than the feature that is assigned to the corresponding transition in $H^+(H_2O)_4$.[29,46,57] This increased structure has been ascribed to near degeneracies between the the state with one quantum of excitation in the OH stretching vibration and states with two quanta of excitation in lower frequency vibrations that correspond to the hindered rotation of the hydronium core.[10,29] Despite the greater structure, no features in the spectrum for $H^+(H_2O)_3$ have been assigned to the combination band involving the OH and OO stretches. Additionally, the intensity in the region where this feature should appear is small.[29,46]

Finally, the experimental spectrum of $H^+(H_2O)_2$[28] shows a large peak at 1047 cm^{-1} as well as peaks that were assigned to transitions to states with one quantum of excitation in the OH stretch and both one and two quanta of excitation in the OO stretch. These assignments were made based on MCTDH calculations of Vendrell *et al.*[47]

It is interesting that the combination band involving a transition to the state with excitation in both the OO and bound OH stretches have been assigned in $H^+(H_2O)_2$ and $H^+(H_2O)_4$, but not in $H^+(H_2O)_3$. This observation is particularly surprising in light of the fact that the frequency of the associated OH stretch blueshifts from $H^+(H_2O)_2$ to $H^+(H_2O)_4$, indicating a weakening of the ionic hydrogen bond as the number of molecules solvating the hydronium core is increased. These trends lead to the question of what factors are responsible for the surprising shifts in the relative intensities of these two transitions, ρ_{OO} defined in Equation 2.14, with solvation of the hydronium core.

2.3.1 Expectations from the Adiabatic Potentials

As noted above the large difference between the OH and OO vibrational frequencies leads to the expectation that an adiabatic separation of these motions will provide a reasonable approach for exploring the spectral implications of the coupling between the OH and OO stretching vibrations in these ions (see Equations 2.8 and 2.9). In the adiabatic approach, separate OO potentials, $\epsilon_{n_{\mathrm{XH}}}(R_{\mathrm{OO}})$, are evaluated for each of the vibrational states in the OH stretch. The resulting potentials are plotted in Figure 2.3 for $n_{\mathrm{XH}} = 0$ and 1 with blue and red curves, respectively. A grey dashed line is added to show the position of the minimum in the $\epsilon_0(R_{\mathrm{OO}})$ adiabatic potential. As seen in these plots, in the case of $H^+(H_2O)_2$, the value of R_{OO} at the minimum in the adiabatic potential increases by 0.06 Å when n_{XH} is increased from 0 to 1. In contrast, in $H^+(H_2O)_4$, the value of R_{OO} at the minimum of $\epsilon_1(R_{\mathrm{OO}})$ is shifted to by -0.03 Å compared to the location of the minimum in $\epsilon_0(R_{\mathrm{OO}})$. In the case of $H^+(H_2O)_3$, no shift in the minimum is observed. The trends in the sizes of ρ_{OO} described above correlate to the magnitude of the shift of the minima in these potentials as is expected for a Franck-Condon calculation of these intensities.

The above trends can be rationalized by the fact that in the case of $H^+(H_2O)_2$, the equilibrium structure has the shared proton roughly equidistant between the donor and acceptor water molecules, and the most probable configuration corresponds to this structure. When the OH stretching vibration is excited, there is a node in the wave function at the optimized position of the shared proton, and the probability amplitude shifts so that the maxima are closer to the oxygen atoms. This shifts the system from a symmetric proton-bound $H^+(H_2O)_2$ to a structure that more closely resembles a hydronium ion that is solvated by a water molecule. The latter structure is anticipated to have a larger R_{OO} separation than the former. In contrast in $H^+(H_2O)_4$ the system starts in a structure that corresponds to a solvated hydronium ion. Excitation of the bound OH bond drives the system toward geometries where there is increased probability that the proton will be in a more equally shared geometry. This results in the observed decrease in R_{OO} with OH vibrational excitation.

$H^+(H_2O)_3$ represents an intermediate situation, and this is reflected by the undetectable change in R_{OO} with vibrational excitation.

While the adiabatic treatment can provide insights into the general trends in the values of ρ_{OO}, the additional question arises whether the adiabatic treatment is sufficient to anticipate the intensities of the transition to the state with one quantum of excitation in the OO as well as the OH stretch, or if these intensities are providing additional information about the effects that are not captured by the adiabatic treatment.

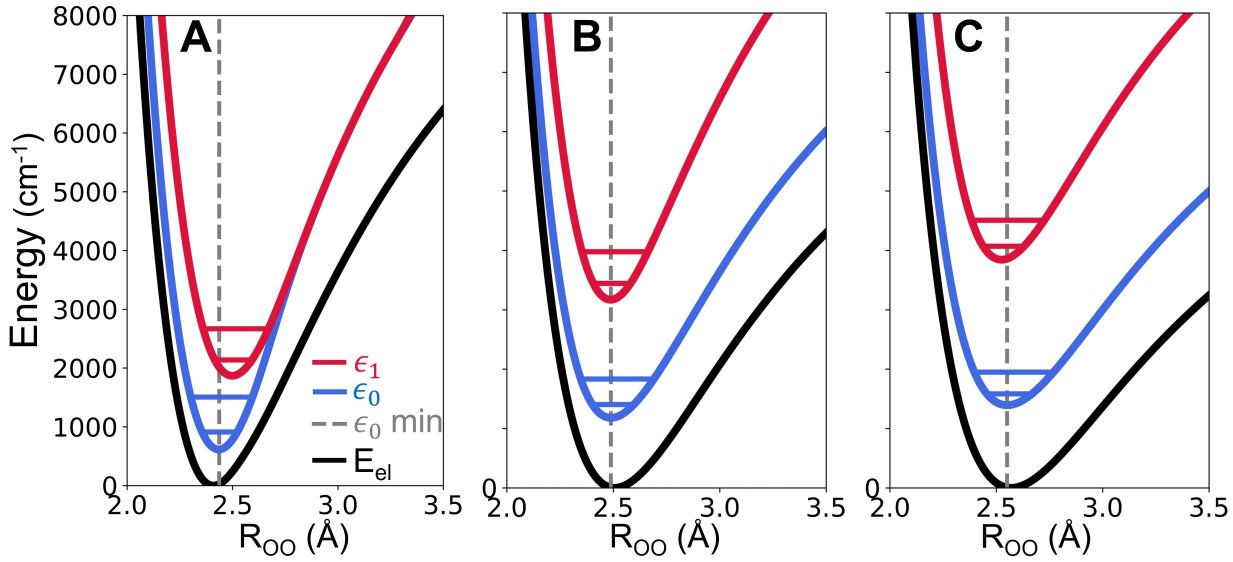

Figure 2.3: Adiabatic potentials for the ground, ϵ_0 (plotted in blue), and first excited, ϵ_1 (plotted in red) states of (A) $H^+(H_2O)_2$, (B) $H^+(H_2O)_3$, and (C) $H^+(H_2O)_4$. The black curve provides the cut through the two-dimensional potential as a function of R_{OO} where the value of r_{XH} is adjusted to minimize the potential energy, while the grey dashed line in each plot shows the minimum in the ϵ_0 adiabatic potential.

2.3.2 $H^+(H_2O)_4$

In exploring the factors that lead to the intensity of the transition to the state with one quantum of excitation in both the OO and OH stretches in $H^+(H_2O)_4$, we will begin with the results of the two-dimensional calculations. The results of this model are provided in

the column labeled 2D in Table 2.2. This model predicts frequencies of the states with one quantum in the OH stretch of 2529 cm^{-1}, with the OH + OO transition having a frequency of 2959 cm^{-1}. These values are in reasonable agreement with the positions and relative intensities of the measured transition that have been assigned to excitation to these states, which are observed at 2650 and 3017 cm^{-1}.[13] The differences between the calculated and measured transition frequencies are attributed to the use of a reduced dimensional treatment. Vibrational perturbation theory calculations performed at the same level of electronic structure theory give frequencies of 2639 and 2957 cm^{-1} for these two transitions, while VCI calculations using a potential surface that was based on CCSD(T)/aug-cc-pVTZ level calculations give energies of 2659 and 3023 cm^{-1}.[13]

In addition to looking at various approximations of the potential energy, we also considered low order expansions of the dipole surface. Specifically, we compare the results obtained when we use the full dipole surface (indicated by "Full" in Table 2.2) to those obtained when the dipole surface is approximated by a linear or quadratic expansion in Δr_{XH}. Other terms in the expansion of the dipole surface were also considered, but we found that they provided much smaller corrections to the results compared to these two terms.

As the results reported in Table 2.2 indicate, the quadratic and full expansions of the dipole surface provide similar values for ρ_{OO}, while the linear expansion gives values that are roughly a factor of two larger. Similar trends are found when the adiabatic approximation is used. Here, the linear expansion of the dipole provides results that are comparable to those obtained when a Franck-Condon approximation is employed, while the introduction of the quadratic terms brings the results in line with those obtained when the full dipole surface is used. This observation that the quadratic terms are needed to obtain a good approximation to the full dipole surface is supported by plots of the x-component of the dipole surface as functions of R_{OO} and r_{XH} as shown in Figures 2.4 and 2.5. In these plots, it is clear that the shape of the full dipole moment is underestimated by the linear approximation, although it is well-captured by the quadratic expansion.

Table 2.2: Vibrational Frequencies and ρ_{OO} Values for $H^+(H_2O)_4$ Obtained Using Various Approximations.

State	$\mathbf{E}_{n_{XH},n_{OO}}$ (cm^{-1})			
(n_{XH}, n_{OO})	2D[a]	Adiabatic[b]	Harmonic[c,d]	Harmonic Adiabatic[d,e]
$E_{1,0}$	2528.7	2488.1	2954.1	2905.9
$E_{0,1}$	360.3	368.0	356.8	362.3
$E_{1,1} - E_{1,0}$	430.8	438.5	356.6	362.3
$E_{1,1}$	2959.4	2926.6	3310.7	3268.2
			ρ_{OO}[f]	
Dipole Expansion	2D[a]	Adiabatic[b]	Harmonic[c,d]	Harmonic Adiabatic[d,e]
Full[g]	2.8%	1.4%	0.46%	-
Quadratic in XH[d,h]	2.3%	1.1%	0.68%	-
Linear in XH[d,h]	5.9%	3.6%	0.0%	-
Franck-Condon[i]	-	4.3%	0.0%	0.98%

[a] Full two-dimensional potential.
[b] Equations 2.8 - 2.11.
[c] Equation 2.3.
[d] Parameters for this model are provided in Table 2.1.
[e] Equations 2.4 - 2.5.
[f] Equation 2.14. The corresponding intensities are reported in Table 2.3.
[g] Full two-dimensional dipole function.
[h] Linear or quadratic expansion of the potential in the OH stretch (Δr_{XH}) about the equilibrium geometry.
[i] Equations 2.12 - 2.13.

Table 2.3: Absolute Intensities for $H^+(H_2O)_4$ (in km mol^{-1}) from the Two-Dimensional and Adiabatic Models.

Dipole	**2D**		**Adiabatic**	
Expansion	$I_{1,0}$	$I_{1,1}$	$I_{1,0}$	$I_{1,1}$
Full	2067.5	58.0	2147.4	30.1
Quadratic in XH	2093.4	48.9	2185.8	23.3
Linear in XH	1602.7	94.0	1706.5	62.0

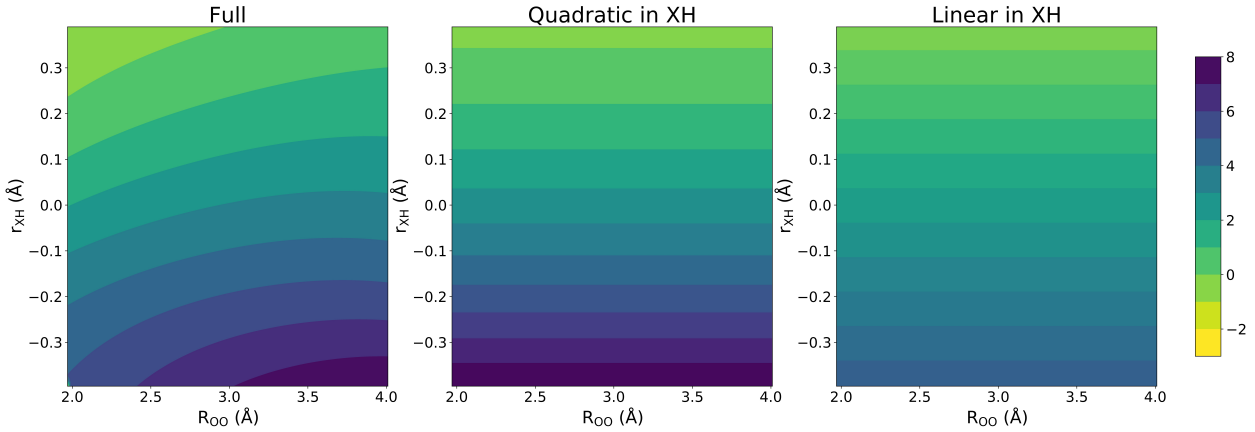

Figure 2.4: Two-dimensional dipole surface (left) with the quadratic expansion in r_{XH} (center) and linear expansion in r_{XH} (right) for $H^+(H_2O)_4$. The expansions are taken about the equilibrium geometry, $r_{\mathrm{XH}} = 0.2722$ Å and $R_{\mathrm{OO}} = 2.5696$ Å.

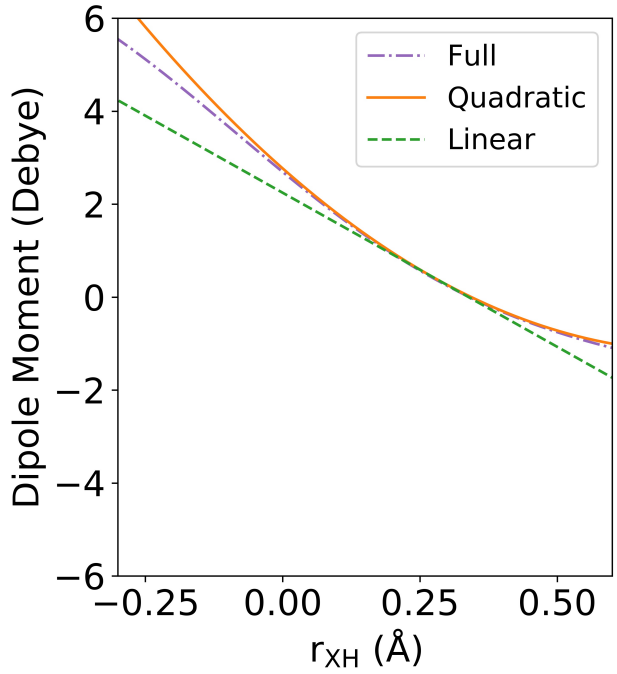

Figure 2.5: One-dimensional cuts of the dipole moment surface and expansions (Figure 2.4) at the equilibrium r_{OO} (2.5696 Å) for $H^+(H_2O)_4$. The purple dot and dashed line provides the cut through the full dipole surface (left in Figure 2.4), the orange solid line the quadratic expansion (center in Figure 2.4) and the green dashed line the linear expansion (right in Figure 2.4). Expansions are taken about the equilibrium r_{XH} distance (0.2722 Å).

The similarity of the results obtained from the Franck-Condon approximation and when a linear expansion of the dipole moment is employed should not be surprising. The Franck-Condon approximation assumes a constant transition moment for the OH stretching vibration. This would be achieved by a linear dipole/harmonic oscillator treatment of the spectrum. The transition moment that is obtained when the linear expansion of the dipole moment in Δr_{XH} is used in the adiabatic treatment is shown with the green dashed line in Figure 2.6A. In this panel, we focus on the x-component of the transition moment, which lies along the O$\cdots$H-O axis (see Figure 2.2). We choose to focus on this component as the contributions from the y and z components are roughly an order of magnitude smaller than the x-component as is indicated by the sizes of components of $\partial\vec{\mu}/\partial r_{\mathrm{XH}}$ and $\partial^2\vec{\mu}/\partial r_{\mathrm{XH}}^2$ provided in Table 2.1.

While the green curve in Figure 2.6A shows a small slope, it is nearly constant over the R_{OO} distances that are sampled by the ground state wave function in the OO stretching vibration (roughly 2.57$\pm$0.1 Å). As is seen in Figure 2.6B-D, as R_{OO} is increased, the width of the wave functions decrease and the average value of r_{XH} shifts to more positive values. This reflects the increased localization of the proton on the hydronium core, and the associated higher frequency of the OH vibration as the separation between the donor and acceptor increases. Turning to the expectations from a harmonic analysis with a dipole moment that is a linear funciton of the displacement of r_{XH}, this increase in frequency correlates to a decrease in the magnitude of the transition moment as

$$\left\langle n_{\mathrm{XH}}=0\left|\frac{\partial\mu}{\partial r_{\mathrm{XH}}}\Delta r_{\mathrm{XH}}\right|n_{\mathrm{XH}}=1\right\rangle=\sqrt{\frac{\hbar}{2\mu_{\mathrm{XH}}\omega_{\mathrm{XH}}}}\left(\frac{\partial\mu_{\mathrm{XH}}}{\partial r_{\mathrm{XH}}}\right) \tag{2.15}$$

The slight increase in ω_{XH} with increasing R_{OO} results in the non-zero slope of the green dashed line in Figure 2.6A. In other words, the fact that the transition moment changes with R_{OO} when the dipole moment is a linear function of Δr_{XH} reflects potential couplings between these coordinates. The introduction of the quadratic term in Δr_{XH} in the expansion of the dipole moment function results in a further increase in the magnitude of the x-component

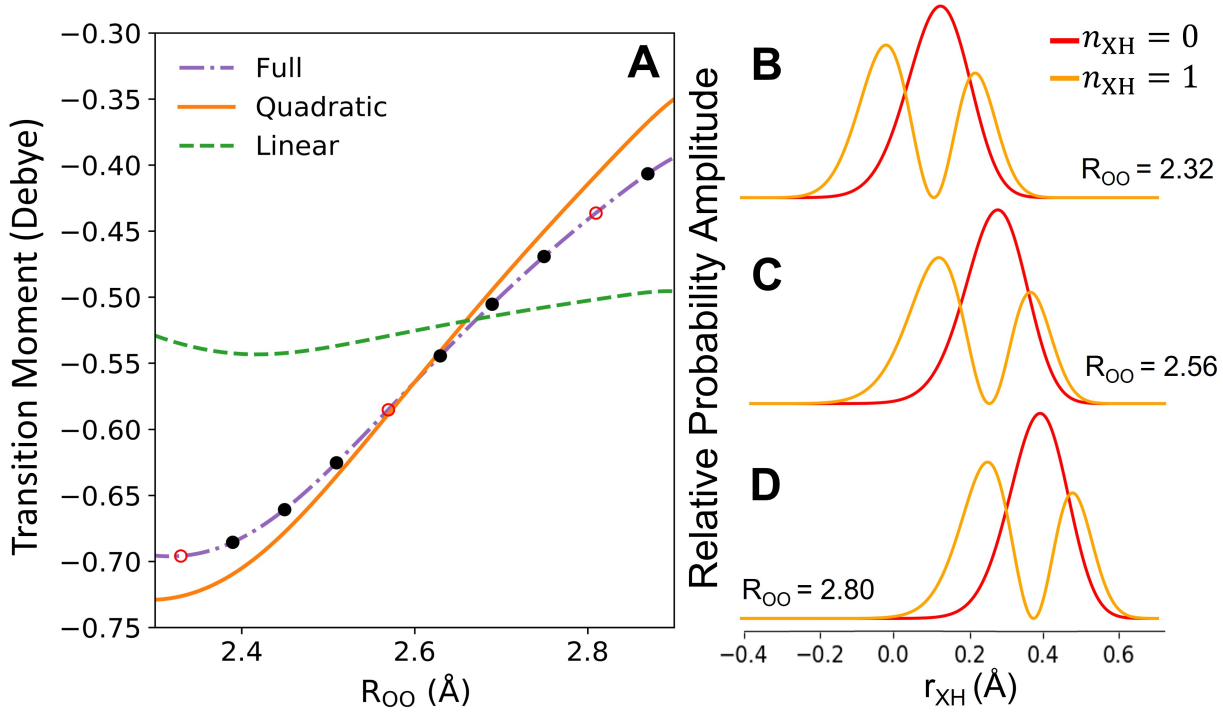

Figure 2.6: (A) The x-component of the transition moment for $H^+(H_2O)_4$ (see Figure 2.2 for the definition of the axes), plotted as a function of R_{OO}. In these plots, the x-component of the transition moment has been calculated using Equation 2.13 with the full dipole surface (dot-dashed purple line), a linear expansion of the dipole surface in Δr_{XH} (green dashed line) and a quadratic expansion of the dipole surface in Δr_{XH} (solid orange curve). The circles provide the values of R_{OO} at which the dipole moment was calculated, while the open red circles are the values of R_{OO} at which the wave functions in panels B-D were evaluated. (B)-(D) The probability amplitudes corresponding to the ground and first excited states in the OH stretching vibration are projected onto r_{XH} for (B) $R_{OO} = 2.32$ Å, (C) $R_{OO} = 2.56$ Å, and (D) $R_{OO} = 2.80$ Å, where 2.56 Å corresponds to the minimum in the potential for $H^+(H_2O)_4$.

of $\partial\vec{\mu}/\partial r_{\mathrm{XH}}$ as r_{XH} is decreased. This leads to the observed increase in the magnitude of the transition moment with decreased R_{OO} as at shorter R_{OO} the equilibrium r_{XH} value becomes smaller, indicative of a stronger hydrogen bond, as is shown in Figure 2.6B-D.

Interestingly, the introduction of the bilinear term in the expansion of the dipole surface, that depends on both Δr_{XH} and ΔR_{OO} does not have a significant effect on the value of ρ_{OO}. This leads us to conclude that the primary contributions to the intensity, beyond the Franck-Condon treatment, arise from the potential coupling between the OO and OH stretching vibrations as well as both mechanical and electrical anharmonicity of the OH stretching vibration.

Similar trends are seen when the harmonic model (Equations 2.2 and 2.15) is used. Again the intensity of the OH + OO transition arises almost entirely from the quadratic term in the expansion of the dipole moment surface. When the harmonic adiabatic model (Equations 2.4 - 2.5) is employed, the OH + OO transition is expected to have an intensity that is larger than the intensity obtained from the harmonic system when the full dipole moment is considered. This further illustrates the central role of the shift of R_{OO} with OH vibrational excitation in the determination of the magnitude of ρ_{OO}.

In addition to the relative intensities, Table 2.2 provides the frequencies obtained by applying these four approximations. There are a few noteworthy results. First, there is a shift of 40 to 50 cm^{-1} between both the adiabatic and 2D and the harmonic adiabatic and harmonic frequencies. These shifts reflect the approximate treatment of the couplings between the two vibrations within the adiabatic approaches. Specifically, in the harmonic adiabatic treatment the kinetic coupling between these two vibrations is set to zero. More interestingly, the frequency of the OO stretch increases by 70 cm^{-1} with OH vibrational excitation. This shift to higher energy is consistent with the OO bond becoming stronger with OH excitation, which is also reflected in the shorter equilibrium R_{OO} in the ϵ_1 surface relative to the ϵ_0 surface (Figure 2.3C). It is also consistent with the measured 316 cm^{-1} frequency of the OO stretch, compared to the 367 cm^{-1} difference between the position of the features associated with the transition to the state with one quantum of excitation in

the OH stretch (2650 cm^{-1}) and the transition to the state with one quantum of excitation in both the OH and OO stretches (3017 cm^{-1}).[13,56]

2.3.3 $H^+(H_2O)_2$

Next we consider $H^+(H_2O)_2$, where the results are reported in Table 2.4. As spectral features have been assigned to transitions to states with one quantum of excitation in the OH stretch and both one and two quanta in the OO stretch, we report values for both $\rho_{OO}^{(1)}$ and $\rho_{OO}^{(2)}$. Here, $\rho_{OO}^{(n_{XH})}$ provides the ratio of the intensity of the transition to the state with one quantum in the OH stretch and n_{XH} quanta of excitation in the OO stretch to the intensity of the transition to the state with only one quantum of excitation in the OH stretch.

Looking at the trends in the $\rho_{OO}^{(n_{XH})}$ values from both the adiabatic treatments and when the full two-dimensional potential is considered, we find that the values obtained using the full dipole surface are nearly identical to those obtained when a linear expansion of the dipole surface in Δr_{XH} is used. Further, when an adiabatic separation of the OO and OH stretching vibrations is employed the results obtained using the linear expansion of the dipole surface differ from those obtained from a Franck-Condon treatment of the intensities. Introducing quadratic terms in Δr_{XH} to the expansion of the dipole moment surface has no significant effect on the result. This last observation is consistent with the fact that $r_{XH} = 0.002$ Å at the optimized geometry used in this study and that the potential surface for $H^+(H_2O)_2$ is nearly symmetric with respect to displacements of r_{XH} from this value. Therefore, by symmetry, the component of the dipole moment along the OO axis should be an odd function of the displacement of the hydrogen atom from its equilibrium value. Further, the deviation between the Franck-Condon intensities and those obtained when a linear expansion of the dipole surface in Δr_{XH} is used is consistent with the significant slope of the transition moment for the OO stretch excitation, shown in the green dashed line in Figure 2.7A. The shape of this curve is nearly identical to the curve of the transition moments obtained when the full dipole surface is used (purple dot-dashed line in Figure 2.7A). The primary difference between these two curves comes through a shift of roughly 0.06 D. The similarity of these

Table 2.4: Vibrational Frequencies and $\mathbf{P}_{\mathrm{OO}}^{(\mathbf{n}_{\mathrm{XH}})}$ Values for $H^+(H_2O)_2$ Obtained Using Various Approximations.

State		$\mathbf{E}_{n_{\mathrm{XH}},n_{\mathrm{OO}}}$ (cm^{-1})
$(n_{\mathrm{XH}}, n_{\mathrm{OO}})$	2D[a]	Adiabatic[b]
$E_{1,0}$	1256.6	1224.5
$E_{0,1}$	592.5	593.0
$E_{1,0} - E_{1,1}$	528.5	530.4
$E_{1,1}$	1785.0	1754.9
$E_{1,2}$	2299.2	2271.2
		$\rho_{\mathrm{OO}}^{(1)}$ [c]
Expansion	2D[a]	Adiabatic[b]
Full[d]	27%	24%
Quadratic in XH[e]	27%	23%
Linear in XH[e]	27%	23%
Franck-Condon[f]	-	39%
		$\rho_{\mathrm{OO}}^{(2)}$ [c]
Expansion	2D[a]	Adiabatic[b]
Full[d]	4.9%	4.3%
Quadratic in XH[e]	4.8%	4.2%
Linear in XH[e]	4.8%	4.2%
Franck-Condon[f]	-	9.0%

[a] Full two-dimensional potential.
[b] Equations 2.8 - 2.11.
[c] Equation 2.14. The corresponding intensities are reported in Table 2.5.
[d] Full two-dimensional dipole function.
[e] Linear or quadratic expansion of the potential in the OH stretch (Δr_{XH}) about the equilibrium geometry.
[f] Equations 2.12 - 2.13.

Table 2.5: Absolute Intensities for $H^+(H_2O)_2$ (in km mol^{-1}) from the Two-Dimensional and Adiabatic Models.

Dipole	**2D**			**Adiabatic**		
Expansion	$I_{1,0}$	$I_{1,1}$	$I_{1,2}$	$I_{1,0}$	$I_{1,1}$	$I_{1,2}$
Full	2741.2	747.6	134.7	2762.8	654.3	118.2
Quadratic in XH	3090.7	830.9	149.8	3117.8	726.1	131.5
Linear in XH	3091.2	831.1	149.8	3117.9	726.1	131.5

two curves explains the small changes observed in the $\rho_{OO}^{(n_{XH})}$ values when the dipole surface is approximated by a low-order expansion in Δr_{XH}, but does not explain the curvature in the linear expansion (green dashed line). One would expect that a linear expansion of the dipole surface would yield a nearly constant transition moment, as was observed for $H^+(H_2O)_4$.

The above trends indicate that the intensity of the OH + OO transition with one or two quanta in the OO stretch reflects anharmonicity in the potential leading to a R_{OO} dependence of the transition moment due to the dependence of this quantity on the OH stretching frequency demonstrated by Equation 2.15. While in $H^+(H_2O)_4$, the energy differences between the states with $n_{XH} = 0$ and 1 shown in Figure 2.6B-D are 2546, 2491 and 2852 cm^{-1}, respectively. The corresponding energy differences for the states of $H^+(H_2O)_2$ plotted in Figure 2.7B-D are 2963, 1574 and 697 cm^{-1}, respectively. Based on Equation 2.15 the larger changes in the OH stretching frequency in $H^+(H_2O)_2$ compared to $H^+(H_2O)_4$ will lead to the observed significant decrease in the magnitude of the transition moment with decreased R_{OO} and the deviation of the results obtained using a linear expansion of the dipole surface and those resulting from a Franck-Condon treatment of the intensities.

In addition to the values of ρ_{OO}, Table 2.4 provides the frequencies obtained using the full two dimensional potential and the adiabatic approximation. As with the tetramer, the values of $E_{0,1}$ deviate significantly from $E_{1,1} - E_{1,0}$, although in this case $E_{0,1}$ is 64 cm^{-1} larger. Similar trends are seen in the experimental spectra, where $E_{1,1} - E_{1,0} = 423$ cm^{-1}, while $E_{1,2} - E_{1,1} = 408$ cm^{-1}.[28,47] The change in OO stretching frequency reflects the weakening

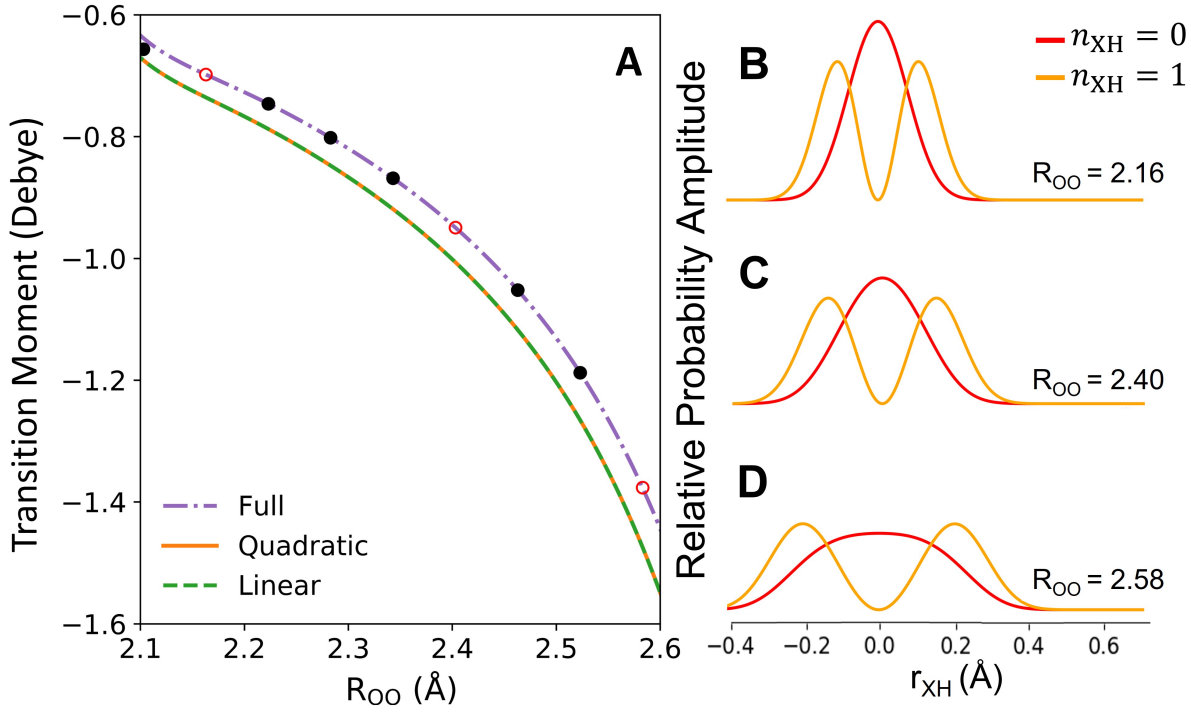

Figure 2.7: The same as Figure 2.6 for $H^+(H_2O)_2$ where in (B)-(D) The probability amplitudes corresponding to the ground and first excited states in the OH stretching vibration are projected onto r_{XH} for (B) $R_{OO} = 2.16$ Å, (C) $R_{OO} = 2.40$ Å, and (D) $R_{OO} = 2.58$ Å, where 2.40 Å corresponds to the minimum in the potential for $H^+(H_2O)_2$.

of the O_DO_A interaction with OH vibrational excitation, discussed above, and is consistent with the associated increase in the minimum value of R_{OO} with OH vibrational excitation. In contrast to $H^+(H_2O)_4$, we do not report results for harmonic analyses of $H^+(H_2O)_2$ due to the much larger anharmonicity of the OH stretching vibration in this system. This is manifested in several ways including the very low frequency of the OH stretching vibration and the breadth of the ground state wave functions shown in Figure 2.7B-D.

2.3.4 $H^+(H_2O)_3$

As noted above, $H^+(H_2O)_3$ represents an intermediate situation between $H^+(H_2O)_2$ and $H^+(H_2O)_4$. The results for this system are provided in Table 2.6. While there are some changes in the calculated values of ρ_{OO} depending on the nature of the approximations that are used, all are smaller than 1% and often below 0.25%. As such, we treat these values as being nearly zero, which is consistent with the experimental findings. This is also consistent with the 0 Å shift between the positions of the minima in $\epsilon_0(R_{OO})$ and $\epsilon_1(R_{OO})$ for this system (see Figure 2.3B).

While the transitions to states with one quantum in both the OH and OO stretching vibrations show negligible intensity, the frequency of the OO stretching vibration is affected by OH excitation. In fact, the difference between $E_{0,1}$ and $E_{1,1} - E_{1,0}$ exceeds +100 cm^{-1}, which is larger than was found for $H^+(H_2O)_4$. The larger shifts reflect the more anharmonic OH stretching vibration in $H^+(H_2O)_3$ than in $H^+(H_2O)_4$, as can be seen in Figure 2.8.

Table 2.6: Vibrational Frequencies and ρ_{OO} Values for $H^+(H_2O)_3$ Obtained Using Various Approximations.

State	$\mathbf{E}_{n_{XH},n_{OO}}$ (cm^{-1})			
(n_{XH}, n_{OO})	2D[a]	Adiabatic[b]	Harmonic[c,d]	Harmonic Adiabatic[d,e]
$E_{1,0}$	2069.6	2040.7	2564.9	2522.3
$E_{0,1}$	422.7	432.7	406.9	413.5
$E_{1,1} - E_{1,0}$	533.5	534.48	406.9	413.5
$E_{1,1}$	2603.3	2575.2	2971.9	2935.8
			ρ_{OO}[f]	
Dipole Expansion	2D[a]	Adiabatic[b]	Harmonic[c,d]	Harmonic Adiabatic[d,e]
Full[g]	0.22%	0.01%	0.31%	-
Quadratic in XH[d,h]	0.08%	0.08%	0.49%	-
Linear in XH[d,h]	0.95%	0.16%	0.00%	-
Franck-Condon[i]	-	0.38%	0.0%	0.78%

[a] Full two-dimensional potential.
[b] Equations 2.8 - 2.11.
[c] Equation 2.3.
[d] Parameters for this model are provided in Table 2.1.
[e] Equations 2.4 - 2.5.
[f] Equation 2.14. The corresponding intensities are reported in Table 2.7.
[g] Full two-dimensional dipole function.
[h] Linear or quadratic expansion of the potential in the OH stretch (Δr_{XH}) about the equilibrium geometry.
[i] Equations 2.12 - 2.13.

Table 2.7: Absolute Intensities for $H^+(H_2O)_3$ (in km mol^{-1}) from the Two-Dimensional and Adiabatic Models.

Dipole	**2D**		**Adiabatic**	
Expansion	$I_{1,0}$	$I_{1,1}$	$I_{1,0}$	$I_{1,1}$
Full	2603.4	5.7	2698.9	0.2
Quadratic in XH	2725.2	2.07	2865.2	2.2
Linear in XH	2093.2	19.9	2224.2	3.5

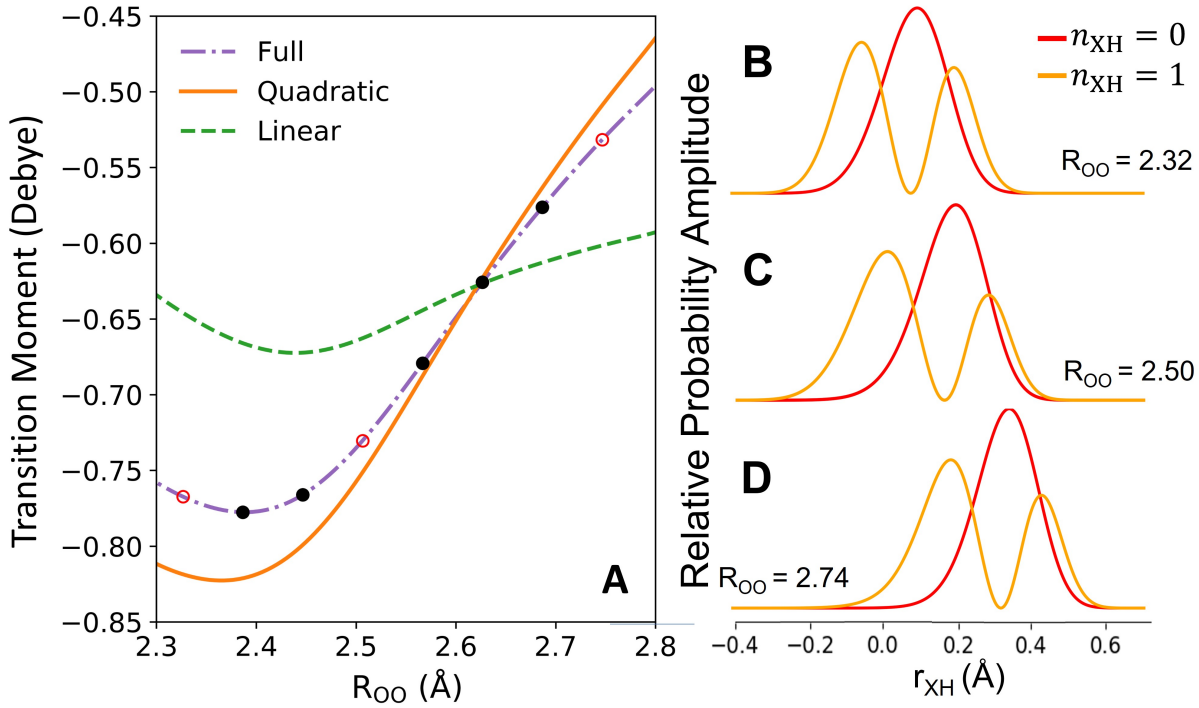

Figure 2.8: The same as Figure 2.6 for $H^+(H_2O)_2$ where in (B)-(D) The probability amplitudes corresponding to the ground and first excited states in the OH stretching vibration are projected onto r_{XH} for (B) $R_{OO} = 2.32$ Å, (C) $R_{OO} = 2.50$ Å, and (D) $R_{OO} = 2.74$ Å, where 2.50 Å corresponds to the minimum in the potential for $H^+(H_2O)_3$.

2.4 Conclusions

We explored the spectral consequence of changes in the hydrogen-bonding environment, which weaken the hydrogen bond strength through investigations of the complexes generated by solvating hydronium with one to three water molecules using a two-dimensional description of the potentials and dipole surfaces for these ions. Through this study, we were able to elucidate the origins of the changes in the intensities of the transitions to states with excitation in both the hydrogen bonding OH and the donor-acceptor OO stretching vibrations of these clusters. It was found that the relative intensity of this transition reflects changes in the frequency and anharmonicity of the OH vibration with OO stretch excitation. This is also reflected in shifts in the OO stretch frequency with OH vibrational excitation. Taken together, this work points to several signatures of the strength of strong hydrogen bonds that compliment the information encoded in the bands associated to excitation of the OH stretching vibration.

Chapter 3

CHARACTER OF THE OH STRETCH-BEND COMBINATION BAND IN THE VIBRATIONAL SPECTRA OF THE "MAGIC" NUMBER $H_3O^+(H_2O)_{20}$ AND $D_3O^+(D_2O)_{20}$ CLUSTER IONS

3.1 Introduction

The vibrational spectrum of water in the OH stretching region is widely used to provide structural information on the local hydrogen bonding environments adopted by water molecules in extended hydrogen-bonding networks.[20,58–61] The spectrum of water, reproduced in Figure 3.1(a) and b, is an archetypal example of this. The broad envelope associated with the OH stretch fundamental reflects the extreme distortions of water molecules according to the topology of the extended hydrogen-bond network.[18,62–64] The local contributions to this band contour are found to conform to the usual spectroscopic trends associated with strong hydrogen bonds in which the intensities and breadths of the fundamental transitions increase with increasing red shift from the free OH frequency.[45,65] As such, the shape of the OH stretching band in water results from an overexpression of the contributions from sites with large red-shifts, in part accounting for the bell-shaped envelope in both the H_2O and D_2O isotopologues indicated in Figure 3.1(a) and 3.1(b), respectively. Another contribution that affects the low energy region arises from strong Fermi-resonance coupling with the overtone

of the HOH/DOD bending vibration.[18,66] Here we are concerned with the relatively weak absorption band corresponding to the excitation of the v=1 levels in both the OH stretch and HOH bending modes, hereafter denoted stretch-bend. This occurs near 5000 cm^{-1} in H_2O and 4000 cm^{-1} in D_2O. The stretch-bend bands are widely used in astronomical studies[1,67,68] due to their smaller cross sections, which allows for acquisition of unsaturated spectra.

The stretch-bend combination bands in liquid H_2O and D_2O are depicted in the expanded inset at the right of Figure 3.1(a) and 3.1(b). For both isotopologues, the stretch-bend bands are clearly asymmetric, with a sharp rise on the high energy side and slow falling tail on the low energy side. Here we address the origin of the differences between the OH stretching and combination band shapes by analyzing the spectra of the cryogenically cooled $H_3O^+(H_2O)_{20}$ and $D_3O^+(D_2O)_{20}$ cluster ions, both of which have been discussed earlier in the regions of the OH(D) stretching modes as well as lower frequency motions that yield bands down to 200 cm^{-1}.[2,69] The spectrum of the D_2-tagged $D_3O^+(D_2O)_{20}$ cluster is presented in Figure 3.1c in the 200-4500 cm^{-1} region. We note that near IR measurements of smaller water clusters and protonated water clusters (n=1-7) were obtained in gas phase as well as matrix isolation.[70–73] Here we extend that work to the larger (n=20) clusters because the OH(D) band envelopes are much broader, reflecting the wide range of local hydrogen bond sites afforded by the distorted cage structures derived from the twelve five membered ring motifs. For example, the spectrum of the 200 K $Cs^+(H_2O)_{20}$ cluster is qualitatively similar to that of the air-water interface obtained with surface-sensitive sum-frequency spectroscopy, since both regimes display non-bonded OH groups.[74–78] Although the cluster systems over-emphasize the free OH feature relative to the fully coordinated bulk regime, the n=20 cluster systems nonetheless enable quantitative assessment of the evolution of oscillator strength across the stretch-bend band envelope associated with well-defined hydrogen-bonding network sites.

Analysis of the OH fundamental spectra displayed by the 'magic' number $H_3O^+(H_2O)_{20}$ and $D_3O^+(D_2O)_{20}$ clusters revealed that these cluster ions adapt distorted pentagonal dodecahedron (DPD) cage structures with the hydronium ion resting on the surface and a water molecule embedded inside of it.[2,69] This arrangement features various types of hydrogen-

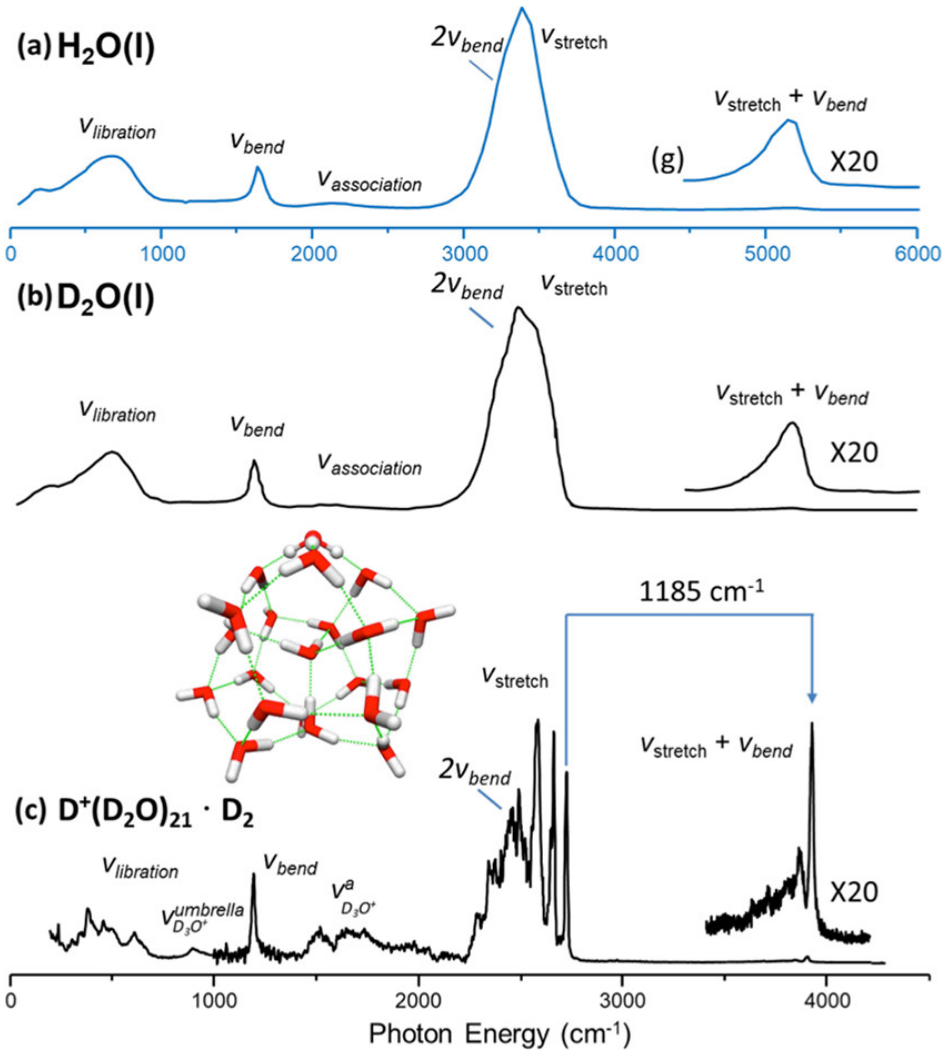

Figure 3.1: (a), (b) IR spectra of liquid H_2O and D_2O, respectively. The comparison between the $\nu_{stretch}$ and the $\nu_{stretch} + \nu_{bend}$ regions illustrates the changes in the band envelopes associated with the OH/OD stretching fundamental and the combination band (expanded inserts on right) arising from excitation of the v=1 levels of the OH/OD stretch and intramolecular bend. (Adapted from Hale *et. al.*[1]) (c) Inset, representative low energy structure (PD_0) and the vibrational predissociation spectrum of D_2-tagged $D_3O^+(D_2O)_{20}$. Spectrum in (c) 200-3000 cm^{-1} is reproduced from Fournier *et. al.*,[2] while that in the 3000-4500 cm^{-1} region is reported in this work.

bonding configurations that differ according to number of donor (D) and acceptor (A) hydrogen-bonds at each site, as well as the topologies of the water molecules in the second hydration shell around each site.[79] Note that there are many low energy isomers that conform to the overall the DPD structure at the trap temperature (20 K).[80,81] This feature has the advantage in simulating bulk water behavior because it enhances the diversity of hydrogen-bonding environments that can be experimentally accessed in the cold cluster regime.[15,45,81,82] With this in mind, Figure 3.2(a) presents a representative structure (denoted PD0) to illustrate the basic topology of the cage. The corresponding D_2-tagged spectrum of the $D_3O^+(D_2O)_{20}$ isotopologue is presented in Figure 3.1(c). The band at 1185 cm^{-1} is traced to the DOD bending fundamentals while the features in the 1400-2200 cm^{-1} range arise from the hydronium (D_3O^+) stretches.[83] Several sharp features appear in the higher energy OD stretching region along with a more congested lower energy band envelope spanning the range 2300 – 2550 cm^{-1}. Comparison with the liquid D_2O spectrum in Figure 3.1(b) indicates that the range of the cluster response occurs over a similar range as that found in the condensed phase. In this work, we extend the $D_3O^+(D_2O)_{20}$ spectral survey to include the range of the stretch-bend combination band at the right of Figure 3.1(c). This reveals a very weak feature displaced by 1185 cm^{-1} above the free OD band at 2731 cm^{-1}.

Unlike the OD stretching region, the highest energy stretch-bend band (at 3916 cm^{-1}) dominates the band envelope with much weaker absorptions degrading the profile on the lower energy side. The band pattern is compared on a common energy axis in Figure 3.2 to illustrate the fact that three of the higher energy bands labeled $OD_b^{ADD'}$, OD_b^{ADD} and OD_{free}^{AAD}, are derived from features in the fundamental region. The 2200-2400 cm^{-1} envelope contains contributions from both the bound OD of the AAD waters and the OD stretches from the AADD water (colored red and blue in the structure and peak labels in Figure 3.2, respectively). The ADD′ water molecules (yellow) next to the hydronium have more red-shifted OD stretches compared to those of the ADD waters (orange), consistent with the latter being located farther from the charge defect. That is, the larger redshift of the ADD water molecules adjacent to the hydronium ion results from partial positive charge delocal-

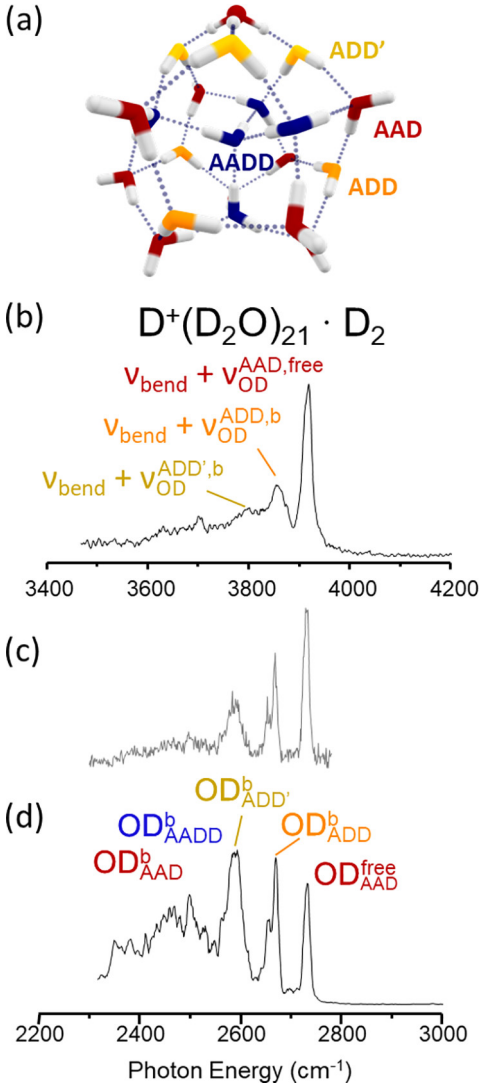

Figure 3.2: (a) Representative $D_3O^+(D_2O)_{20}$ structure (denoted PD_0) with water molecules color-coded according to the number of hydrogen bonds accepted and donated (e.g., AAD denotes acceptor-acceptor-donor); (b) vibrational spectrum of the OD stretch-DOD bend combination (denoted stretch-bend) band observed for D_2-tagged $D_3O^+(D_2O)_{20}$; (c) combination band envelope red shifted by 1185 cm^{-1} (one quanta of DOD bend) to line up with the highest energy fundamental feature in (d). The spectrum in (c) is normalized by the calculated intensities of the OH stretch fundamental transitions at the harmonic level. The peak frequencies are collected in Table 3.1

ization onto them, which acts to weaken their OH bonds.[9] The highest energy fundamental corresponds to the free OD stretches on the AAD water molecules (red). The identification of common OD stretching modes in both the fundamental and stretch-bend regions allows for quantitative evaluation of the anharmonic coupling between these motions for a few of the sites, with the values indicated in Table 3.1. The free OD, for example, is displaced by 1185 cm^{-1}, which is very close to the value of the bending fundamental in the bare D_2O molecule. As such, the anharmonic coupling is quite small. Similarly, the ADD molecules displacement of 1191 cm^{-1} is consistent with the expected increase in the bend frequency upon donation of hydrogen bonds.

Table 3.1: Frequencies and Full Width Half Maximum (FWHM) of the Fundamental OH/OD Stretching Bands and Their Corresponding Combination Bands.

Fundamental Peak label	Fundamental Frequency (cm^{-1})	Fundamental FWHM (cm^{-1})	Combination Frequency (cm^{-1})	Combination FWHM (cm^{-1})	Difference (cm^{-1})
OD, OD + DOD bend (1197 cm^{-1})					
OD^{AAD}_{free}	2731	13	3916	21	1185
OD^{AAD}_{bound}	2670	12	3861	20	1191
$OD^{AAD'}_{bound}$	2584	-	3789	-	1205
OH, OH + HOH bend (1629 cm^{-1})					
OD^{AAD}_{free}	3699	11	5307	30	1608
OD^{AAD}_{bound}	3592	17	5195	40	1603

The fact that anharmonic coupling between the bend and stretching modes is small, in turn, indicates that the oscillator strength in the stretch-bend band is not derived primarily mechanical anharmonicity. One aspect of the difference in band shapes between the OH stretch fundamental and the stretch-bend band envelope is that the fundamental exhibits the usual hydrogen bonding trend that the more red shifted bands arising from more strongly bound OH groups increase almost linearly in the red shift.[84] This effect enhances the lower energy region of the envelope beyond the number of transitions at play. It therefore appears that the intensities of the stretch-bend transitions involving low frequency OH stretch

fundamentals are not enhanced like those of the OH stretch fundamentals. As an empirical test of this conjecture, Figure 3.2(c) presents the shape of the fundamental band envelope renormalized so that the intensities are divided by the calculated harmonic band strengths (effectively the same as dividing by the red shift). This shape is much more representative of that displayed by the experimental stretch-bend envelope. We next address the theoretical analysis describing why this difference occurs.

3.2 Theory

We explore the origins of the intensity in the transitions to the states with one quantum of excitation in both the HOH bend and one of the OH stretches by considering the behavior of an isolated water molecule. If we calculate the spectrum of water within a harmonic oscillator approximation and assume that the dipole moment can be approximated by a linear expansion in the associated vibrational coordinates (r_{OH} and θ_{HOH} for the OH stretch and HOH intramolecular bend, respectively):

$$\mu\left(r_{\mathrm{OH}}, \theta_{\mathrm{HOH}}\right) = \mu_{eq} + \frac{\partial \mu}{\partial r_{\mathrm{OH}}} \Delta r_{\mathrm{OH}} + \frac{\partial \mu}{\partial \theta_{\mathrm{HOH}}} \Delta \theta_{\mathrm{HOH}} \tag{3.1}$$

the stretch-bend transition will not carry any intensity. This is evident from the form of the transition dipole matrix element given by:

$$\langle \Psi_{stretch}(v=1)\Psi_{bend}(v=1)|\, \mu \,|\Psi_{stretch}(v=0)\Psi_{bend}(v=0)\rangle = 0 \tag{3.2}$$

which follows because the $\Psi_{vib} = \Psi_{stretch}(\Delta r_{\mathrm{OH}})\Psi_{bend}(\theta)$ product basis functions are orthonormal, one-dimensional functions for each normal mode. On the other hand, treating the wave functions as anharmonic oscillators and introducing higher order terms in the expansion of the electric dipole surface can both yield oscillator strength in the combination band. These effects are commonly discussed as mechanical and electrical anharmonicities, respectively.[39] In the case of electrical anharmonicity, the term:

$$\frac{\partial^2 \mu}{\partial r_{\mathrm{OH}} \partial \theta} \Delta r_{\mathrm{OH}} \Delta \theta_{\mathrm{HOH}} \tag{3.3}$$

in the Taylor expansion of the dipole moment will result in a non-zero matrix value for the element in Equation 3.2 since the arguments of both wavefunctions now appear in the matrix element. A useful way to cast this term is to formulate it as:

$$\frac{\partial^2 \mu}{\partial r_{\mathrm{OH}} \partial \theta} = \frac{\partial \mu}{\partial \theta_{\mathrm{HOH}}} \left(\frac{\partial \mu}{\partial r_{\mathrm{OH}}} \right) \tag{3.4}$$

and recognize that the oscillator strength of the fundamental is proportional to $\left(\frac{\partial \mu}{\partial r_{\mathrm{OH}}}\right)^2$. This emphasizes that it is not the intensity of the OH stretch fundamental that drives IR excitation of the stretch-bend band, but rather by how much its intensity changes upon displacement of the angle, θ_{HOH}. This dependence manifests as a twist in the shape of the dipole surface in which the slope along the $\mathrm{r_{OH}}$ axis changes along θ_{HOH}.

3.3 Results & Discussion

While both mechanical and electrical effects contribute to oscillator strength for the stretch-bend transitions, analysis of water dimer using second order perturbation theory (based on internal coordinates),[25] we find that the leading contribution indeed comes from the quadratic term in the expansion of the dipole moment operator (Equation 3.3). Additionally, in contrast to earlier studies of the OH stretch overtone of the water dimer where there is a partial cancellation of the contributions to the intensity from higher order terms in the potential and dipole surface, these two contributions often have the same sign when we consider the intensity of the stretch-bend transition.[85,86]

In Figure 3.3, we plot cuts through the dipole surfaces for the water monomer (Figure 3.3(a)), dimer (Figure 3.3(b)), and two hydrogen bonding arrangements of a water molecule embedded in the water hexamer (Figure 3.3(c) and 3.3(d)). The latter two differ according to whether the water molecule in question accepts (A) or donates (D) a hydrogen bond,

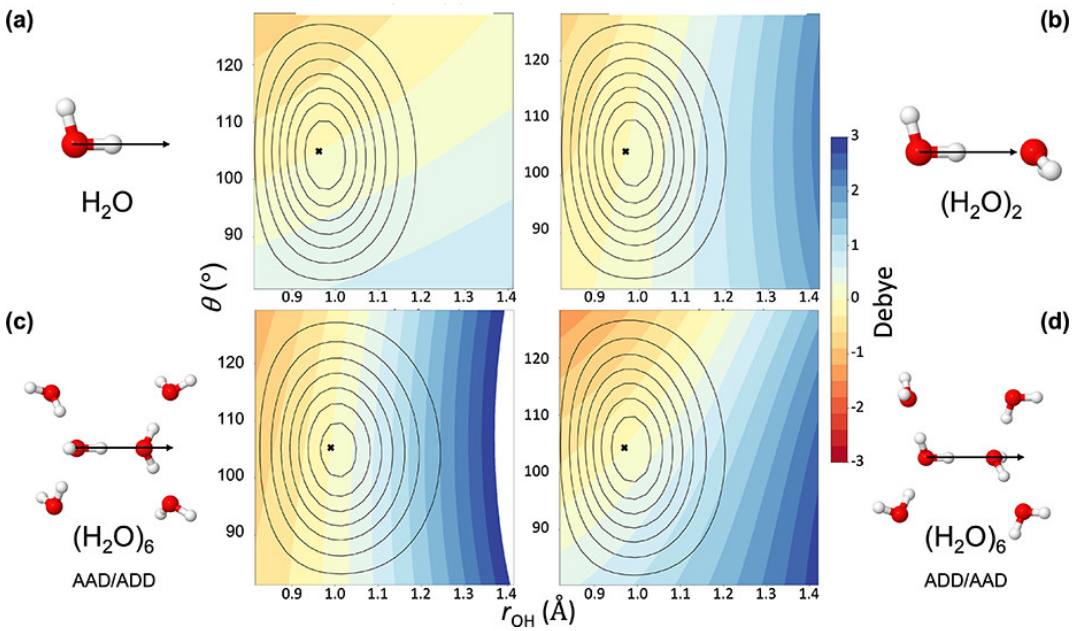

Figure 3.3: Contour maps of the component of the electric dipole moment along the OHO axis (denoted above by black arrow in the inset structures) after subtracting off the value at the equilibrium geometry (black x in each plot) as functions of the HOH bending angle (°) and the OH bond length (Å). The color bar provides index for the magnitude of the dipole moment (Debye). The v=0 vibrational wave functions are plotted as black contours where the innermost line corresponds to a value of 0.1 and the outermost is 0.01.

and the analogous environment of the water molecule attached to the it. These geometries were adapted from a recent study,[18] and span a wide range of hydrogen bond strengths. Specifically, the strongest hydrogen bonding environment is represented by the arrangement shown Figure 3.3(c), while the weakest hydrogen bonding environment is reflected by the arrangement shown in Figure 3.3(d). The most striking difference among these plots is their range and the slopes, particularly with respect to the OH bond length. The trends are consistent, for example, with the intensity of the OH stretch fundamental transition increasing with bond length and hence hydrogen-bond strength.[19,87] For the purpose of the present discussion, the important characteristic of these surfaces is the mixed second derivative (Equation 3.3) More specifically, the value of the second derivative for the weakest hydrogen bonding situation (and smallest red shift) is 90% that of a strongly bound OH group with an associated large red shift in the fundamental. In contrast, the values of $\frac{\partial \mu}{\partial r_{\mathrm{OH}}}$ differ by as much of a factor of 3.

In Figure 3.4 we show the calculated harmonic intensities (based on a quadratic expansion of the dipole moment and harmonic wave functions - see Chapter 4 for more details) for local OH oscillators in a variety of hydrogen-bonded complexes (see Figure 3.5 for structures). The intensities of transitions to the v_{OH}=1 levels are displayed in Figure 3.4(a) and increase roughly linearly by about a factor of 34 with increasing red shift, consistent with the observed shape of the OH stretch fundamental envelope.[65,87] On the other hand, the intensities of the stretch-bend transitions are much less sensitive to the frequency, spanning a range of only about a factor of 5. The specific transitions are grouped according to their local hydrogen-bonding environments as indicated in the insets. There is a much weaker correlation between the stretch-bend intensities and the red shift, which explains the dramatic differences in the intensity profiles of the OH stretch fundamentals and stretch-bend band systems displayed in Figure 3.2(c) and 3.2(d). In particular, the dominance of the free OH(D) feature is mostly due to the larger number of nearly degenerate oscillators that fall in this frequency range.

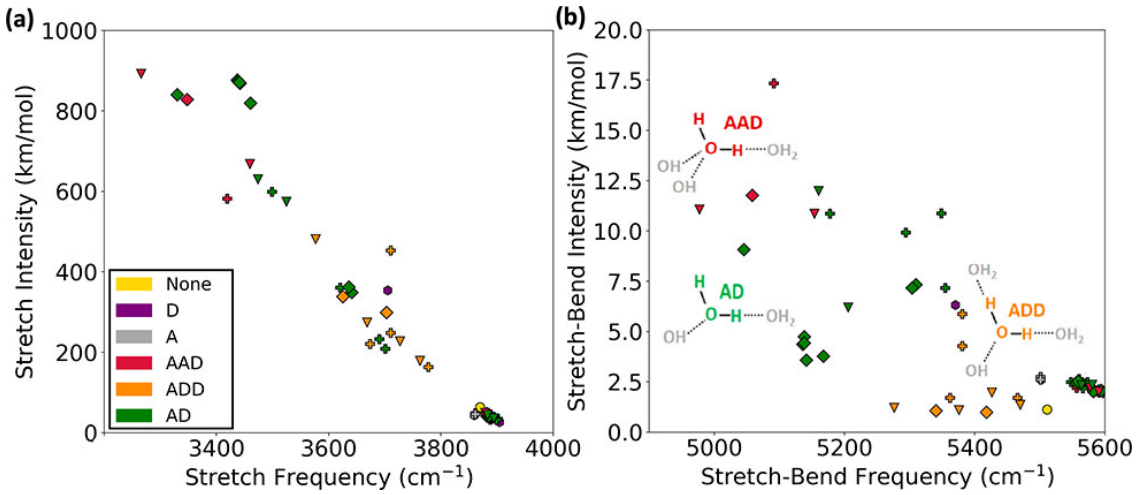

Figure 3.4: Plots of intensity (km mol^{-1}) as a function of the harmonic frequency (cm^{-1}) for transitions to states with (a) one quantum of excitation in the OH stretch, and (b) one quantum of excitation in the OH stretch and one quantum of excitation in the corresponding HOH bend. The colors indicate different hydrogen bonding environments, while the markers represent different structures (circle: H_2O, triangle: $(H_2O)_2$, plus sign: $(H_2O)_4$-Cage, x: $(H_2O)_4$-Three-One, large diamond: $(H_2O)_5$-Cage, thin diamond: $(H_2O)_5$-Ring, square: $(H_2O)_6$-Cage, see Figure 3.5 for the structures).

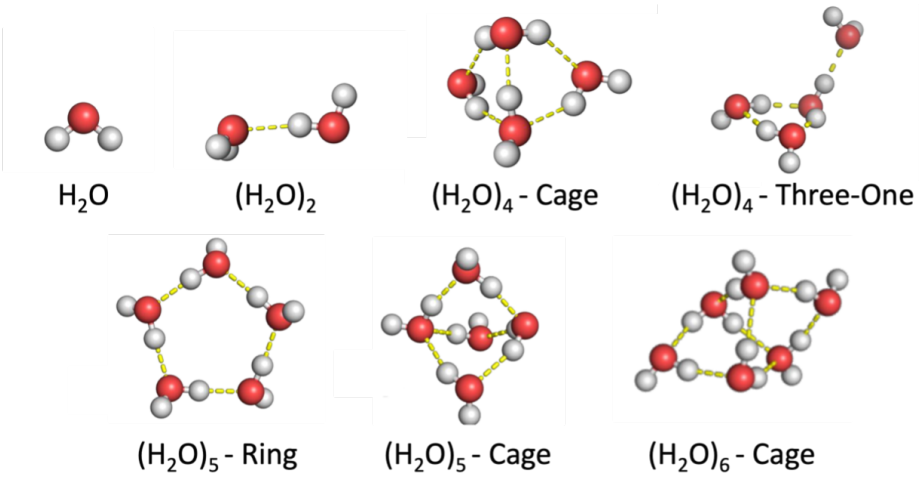

Figure 3.5: Structures used to obtain the data used in Figure 3.4. Each geometry is optimized at the MP2/aug-cc-pVDZ level and then harmonic calculations for each 1 H_2O, rest D_2O isotopologue are conducted.[3] This set of water clusters was used because of the size and variety of geometries and hydrogen bonding environments.

3.4 Conclusions

The differences in the shapes of the OH fundamental and SB envelopes in the spectrum of liquid water are present in the much smaller $H_3O^+(H_2O)_{20}$ and $D_3O^+(D_2O)_{20}$ cluster spectra. This is useful because the cold cluster systems provide well defined hydrogen-bonding environments that can be treated theoretically, yielding a microscopic picture of the origin of the effect. To simulate the observed absorption profile, it remains to include other factors that contribute to the intensity profile, such as variations in the intrinsic linewidths of individual transitions as well as anharmonic interactions such as the Fermi resonance between the OH stretch and the HOH intramolecular bend overtone.[79]

We have reported the experimental spectra in the HOH bend-OH stretch combination band region involving excitation of states with one quantum in each mode for the D_2-tagged $H_3O^+(H_2O)_{20}$ and $D_3O^+(D_2O)_{20}$ clusters. Sharp features in both OH stretch fundamental and SB band envelopes enable estimates of the anharmonic coupling at play in molecules in two of the network sites associated with the water cage. The mechanical anharmonic coupling is relatively weak. The combination band intensity pattern differs significantly from that of the fundamental OH(OD) region. This phenomenon is explained by the stretch-bend transtions intensities' insensitivity of hydrogen-bond environment, whereas for the stretch fundamentals the red shift dramatically enhances the transition moment. This difference is traced to the behavior of the mixed second derivative of the electric dipole moment with respect to the OH stretch displacement and the HOH bond angle. In essence, the intensity of the OH fundamental is not strongly dependent on the bond angle, which is needed to drive oscillator strength in the combination band. As a result, the combination band is most representative of the populations of OH oscillators embedded in different hydrogen-bond environments, modified by the spectral linewidths.

Chapter 4

USING THE INTENSITY OF THE OH STRETCH-BEND COMBINATION BAND TO ELUCIDATE THE HYDROGEN BONDING ENVIRONMENT IN WATER CLUSTERS

4.1 Introduction

The vibrational spectra of hydrogen-bonded networks present in liquid water and water clusters play an important role in our understanding the strengths of the individual hydrogen bonds.[9,18,20,58,59,88,89] For example, the spectrum of liquid water has a broad feature centered at 3300 cm^{-1}, which has been assigned to the $\Delta v = 1$ transition in the OH stretching vibrations. Previous work has shown that the breadth of this feature reflects the shift in the frequencies of individual OH stretching vibrations in response to their local hydrogen-bonding environment.[18,63,64,90] This sensitivity of the frequency to the local environment can be used to deconvolute the measured spectrum into contributions that reflect these local environments.[18,91] A logical next step would be to use this deconvolution to enumerate the OH oscillators in specific hydrogen-bonding environments.

This procedure is complicated by the fact that as the frequencies of the OH vibrations red shift with hydrogen bond strength, the associated intensities of these transitions increase and the density of OH vibrational states decreases. The combination of these effects leads to the observed roughly symmetrical peak in the spectrum of water centered at 3300 cm^{-1}, as shown in Figure 4.1. Recent work of Johnson and co-workers,[18,69,90] has demonstrated that the overall contour of this spectral region is reproduced in the spectrum of clusters containing twenty water molecules. Studies of these size-selected clusters have the advantage that through a combination of isotopic substitution and comparison with harmonic calculations of the spectra, one can assign the individual transitions that make up this band contour.[18,45,90]

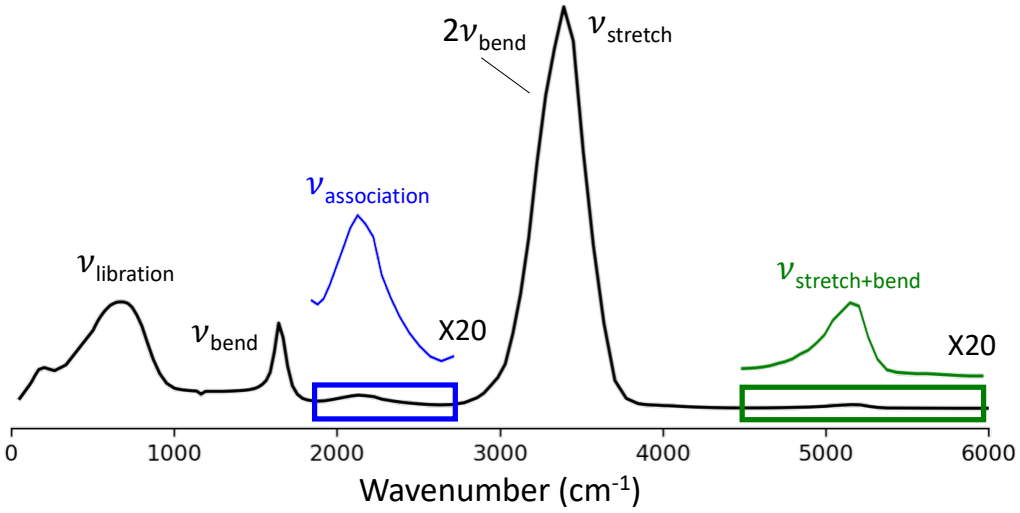

Figure 4.1: Infrared spectrum of liquid water,[1] data obtained from G.M. Hale and M.R. Querry, Appl. Opt. 12, 555-563, (1973).

While the region of the water spectrum that is assigned to $\Delta v_{\mathrm{OH}} = 1$ transitions is logically the first place to look for spectral signatures of hydrogen bonding, there is information encoded in other spectral regions. These include the peak at 800 cm^{-1} that involves excitation of low-frequency stretching and hindered rotational (or librational) motions, the so-called association band near 2100 cm^{-1}, which is shown in blue in Figure 4.1, and the peak at 5200 cm^{-1}, which corresponds to transitions to states with one quantum of excitation in both the OH stretching and the corresponding HOH bending vibrations. While the feature at 3300 cm^{-1} is roughly symmetric, the peak at 2100 cm^{-1} has a longer distribution on the high energy side, while the asymmetry of the peak at 5200 cm^{-1} has intensity that extends further on the red side.

We can rationalize the shape of the peak centered at 2100 cm^{-1} by treating it as a convolution of the low-energy peak (labeled $\nu_{\mathrm{libration}}$ in Figure 4.1) and the peak at 1600 cm^{-1}. This is consistent with the assignment of this feature to transitions to states with one quantum of excitation in the HOH bend and one in the low-frequency hindered rotations of the water molecules.[92,93] Further analysis of the origins of the intensity of this transition

showed that it could be accounted for by considering quadratic terms in the dipole surface that involve displacements of the HOH angle and rotation of the water molecule in the molecular plane. The magnitude of these terms reflects changes in charge distribution as hydrogen bonds are broken and reformed.[24,39]

The peak at 5200 cm^{-1}, which has been assigned to transitions to states with one quantum of excitation in the OH stretching and HOH bending vibrations in the same water molecule, does not have the roughly symmetric shape one would obtain by convoluting the spectral features labeled ν_{stretch} and ν_{bend} in Figure 4.1. In a recent study, we showed that we can recover the band contour of this so-called stretch-bend transition by dividing the intensities of the OH stretch band at 3300 cm^{-1} by the corresponding frequency-dependent intensities of individual OH oscillators.[31] This led us to conclude that the intensities of the stretch-bend transitions are much less sensitive to the hydrogen-bonding environment compared to the corresponding $\Delta v_{\text{OH}} = 1$ transitions. This conclusion was further confirmed by calculations of the intensities of both of these transitions for a series of water clusters using harmonic wave functions and a quadratic expansion of the dipole moment surface.

While that work identified differences between the behavior of the intensities of the OH stretch and stretch-bend transitions, it did not address the deeper question of why there is such a large difference between the dependence of the intensity on the strength of the hydrogen bond in these two spectral regions. The present study focuses on understanding the origin of this difference using several models. In the first part of the study, we develop a two-dimensional model that includes an OH bond length and HOH angle, and identify the terms in the expansion of the dipole moment that have the largest contributions to the intensity of the stretch-bend transitions. We also explore how the relative sizes of the terms in the expansion of the dipole moment are affected by hydrogen bond formation. In a second set of calculations we focus on the contributions to the dipole moment that arise from the large amplitude vibrational motions, which result in changes in the dipole moment based on a fixed-charge model. Comparison of the calculated dipole moment obtained from this fixed-charge model to those obtained using cuts through the calculated dipole function allows us

to explore how changes in the charge distribution affect the sizes of the individual terms in the expansion of the dipole moment function and how hydrogen-bonding affects these trends. These studies focus on an isolated water molecule and transitions involving the bound and free OH bonds in the donor water molecule in $(H_2O)_2$. Finally, we explore how the collective nature of the OH stretching and HOH bending motions affect the overall intensity of the stretch-bend transitions through a series of harmonic calculations involving various isomers of $(H_2O)_2$, $(H_2O)_4$ and $(H_2O)_6$.

4.2 Theory

To begin investigating the origins of the intensity of the two quanta stretch-bend transition, we first define the intensity as[94]

$$I = 2.506[\text{cm D}^{-2}\text{ km mol}^{-1}]\ \nu_{\text{SB}}\left|\langle \text{SB}|\,\vec{\mu}\,|\text{GS}\rangle\right|^2 \tag{4.1}$$

where ν_{SB} is the frequency of the stretch-bend transition in cm^{-1}, $|\text{GS}\rangle$ represents the ground state, and $|\text{SB}\rangle$ represents the stretch-bend excited state. When $|\text{GS}\rangle$ and $|\text{SB}\rangle$ are approximated by products of harmonic oscillator eigenstates, and $\vec{\mu}$ is a linear function of the vibrational coordinates, the intensity will be zero. To move beyond the harmonic approximation for $|\text{GS}\rangle$ and $|\text{SB}\rangle$, we start by considering the solutions to the two-dimensional Hamiltonian that describes the OH stretching vibration, r_{OH}, and the associated HOH bending vibration, θ_{HOH}

$$H = \frac{p_r^2}{2\mu_r} + \frac{1}{4}p_\theta^2 G_{\theta\theta} + \frac{1}{4}G_{\theta\theta}p_\theta^2 + \frac{1}{2}p_r p_\theta G_{r\theta} + \frac{1}{2}G_{r\theta}p_\theta p_r + \frac{\hbar^2}{4}\left(\frac{\partial^2 G_{\theta\theta}}{\partial\theta_{\text{HOH}}^2}\right) + V(r_{\text{OH}},\theta_{\text{HOH}}) \tag{4.2}$$

Here

$$G_{\theta\theta} = \frac{1}{\mu_r r_{\text{OH}}^2} + \frac{1}{\mu_r r_e^2} - \frac{2\cos\theta_{\text{HOH}}}{m_{\text{O}} r_{\text{OH}} r_e} \tag{4.3}$$

and

$$G_{r\theta} = -\frac{\sin\theta_{\mathrm{HOH}}}{m_{\mathrm{O}} r_e} \tag{4.4}$$

are Wilson $G-$matrix[8] elements, where r_e represents the OH bond length from the reference structure. The calculation utilizes a two-dimensional discrete variable representation on a 31×31 grid in r_{OH} and θ_{HOH},[50] and follows the approach described previously.[95] The potential and dipole surfaces used are obtained by displacing θ_{HOH} over a range of $-56°$ to $+64°$ in increments of $4°$, while r_{OH} is displaced from -0.30 Å to $+0.45$ Å in increments of 0.025 Å. These displacements are made according to the z-matrix presented in Table 4.1 and the coordinates presented in Table 4.2

4.2.1 Higher Order Terms in the Potential and Dipole Surfaces

To explore the contributions of higher order terms of the expansion of the dipole moment surface on the stretch-bend intensity in Equation 4.1, we partition the dipole moment surface as

$$\vec{\mu}(r_{\mathrm{OH}}, \theta_{\mathrm{HOH}}) = \vec{\mu}_{eq} + \vec{\mu}_{\mathrm{1st}}(r_{\mathrm{OH}}, \theta_{\mathrm{HOH}}) + \vec{\mu}_{\mathrm{2nd-D}}(r_{\mathrm{OH}}, \theta_{\mathrm{HOH}}) + \vec{\mu}_{\mathrm{2nd-B}}(r_{\mathrm{OH}}, \theta_{\mathrm{HOH}}) + \cdots \tag{4.5}$$

where

$$\vec{\mu}_{\mathrm{1st}}(r_{\mathrm{OH}}, \theta_{\mathrm{HOH}}) = \left(\frac{\partial\vec{\mu}}{\partial r_{\mathrm{OH}}}\right)_{eq} \Delta r_{\mathrm{OH}} + \left(\frac{\partial\vec{\mu}}{\partial\theta_{\mathrm{HOH}}}\right)_{eq} \Delta\theta_{\mathrm{HOH}} \tag{4.6}$$

$$\vec{\mu}_{\mathrm{2nd-D}}(r_{\mathrm{OH}}, \theta_{\mathrm{HOH}}) = \frac{1}{2}\left[\left(\frac{\partial^2\vec{\mu}}{\partial r_{\mathrm{OH}}^2}\right)_{eq} \Delta r_{\mathrm{OH}}^2 + \left(\frac{\partial^2\vec{\mu}}{\partial\theta_{\mathrm{HOH}}^2}\right)_{eq} \Delta\theta_{\mathrm{HOH}}^2\right] \tag{4.7}$$

$$\vec{\mu}_{\mathrm{2nd-B}}(r_{\mathrm{OH}}, \theta_{\mathrm{HOH}}) = \left(\frac{\partial^2\vec{\mu}}{\partial r_{\mathrm{OH}}\partial\theta_{\mathrm{HOH}}}\right)_{eq} \Delta r_{\mathrm{OH}}\Delta\theta_{\mathrm{HOH}} \tag{4.8}$$

and the dipole moment is evaluated at the MP2/aug-cc-pVTZ level of theory/basis using Gaussian 16.[3] In the discussion that follows we will differentiate between the two types of quadratic terms by calling the ones that involve second derivatives with respect to a single coordinate diagonal (Equation 4.7), and quadratic terms that involve derivatives with respect to both r_{OH} and θ_{HOH} bilinear (Equation 4.8).

To obtain the expansion of the dipole moment, we evaluate the energies and dipole moment components at the MP2/aug-cc-pVTZ level of theory and basis for a selected set of OH bond lengths, r_{OH}, and HOH angles, θ_{HOH}. In this analysis, we consider both the bound OH and free OH in $(H_2O)_2$ as well as one of the OH bonds in H_2O. In each system, r_{OH} is displaced from its value in the reference structure by ± 0.0125 Å in increments of 0.00625 Å and θ_{HOH} is displaced by $\pm 2^\circ$ in increments of 1°.

4.2.2 Changes in the Charge Distribution

As we consider the contributions to the intensity from the dipole moment, we further divide the contributions into those that come from displacements of the atoms, assuming fixed charges, and those that result from changes in the charge distribution of the cluster with vibrational excitation. Since the Mulliken charges rarely reproduce the dipole moment, we define the fixed charges so they reproduce the dipole moment of the chosen reference structure.

To obtain the fixed charges used in this model, the charges on the oxygen and hydrogen atoms are chosen to reproduce the dipole moment in the reference structures.

For the isolated water molecule, the two hydrogen atoms are equivalent by symmetry, the net charge is zero, and the dipole moment lies along the bisector of θ_{HOH}. With this information, we define

$$q_{\mathrm{H}} = -\frac{q_{\mathrm{O}}}{2} \tag{4.9}$$

and q_{O} can be evaluated algebraically.

To extend this approach to $(H_2O)_2$, there are two non-zero components of the dipole

moment, the two that are in the plane of the donor water molecule. There are also five unique charges, since the charges of the two hydrogen atoms in the accepting water molecule are equal by symmetry. Evaluation of the fixed charges that reproduce the dipole moment of $(H_2O)_2$ require the introduction of three additional constraints. Since there is little charge transfer between the donor and acceptor water molecule, we assume that the net charges of the water molecules are both zero. For the acceptor water molecule, this leads to the requirement that

$$q_{\rm H}^{\rm (A)} = -\frac{q_{\rm O}^{\rm (A)}}{2} \tag{4.10}$$

which is the same as the constraint used to obtain the fixed charges for the isolated water molecule. The charges of the two hydrogen atoms in the donor are not expected to be equal. On the basis of the Mulliken and NBO charges evaluated at the MP2/aug-cc-pVTZ level of theory/basis, we find that $q_{\rm H}^{\rm (D,b)} \approx 1.46\ q_{\rm H}^{\rm (D,f)}$, where b and f denote the bound OH and free OH in the donor water molecule, respectively. This leads to the relationship

$$q_{\rm H}^{\rm D,b} = -\left(\frac{1.46}{2.46}\right) q_{\rm O}^{\rm D} \tag{4.11}$$

$$q_{\rm H}^{\rm D,f} = -\left(\frac{1}{2.46}\right) q_{\rm O}^{\rm D} \tag{4.12}$$

The above relationships allow us to evaluate the values of $q_{\rm O}^{\rm D}$ and $q_{\rm O}^{\rm A}$ so as to reproduce the dipole moment of $(H_2O)_2$ in the reference structure.

To aide in the comparison of the results of the fixed charge model to the full dipole surface, we rotate the molecule such that the OH bond of interest lies along the $x-$axis and the dipole moment is in the xy plane. We then displace that OH bond length from its value in the reference structure in increments of 0.025 Å. The angle is displaced in increments of 4.0° relative to this structure, with the angle between the OO axis and the biscector of the $\theta_{\rm HOH}$ in the bound water molecule in $(H_2O)_2$ constrained to its value in the reference

structure.

For all the calculations described above, we use the the minimum energy structure, evaluated at the MP2/aug-cc-pVTZ level of theory/basis (see Table 4.2 for the coordinates) for an isolated water. When the displacements are made, the other OH bond length is constrained to its value in the minimum energy configuration. In $(H_2O)_2$, the reference structure corresponds to the minimum energy structure obtained when the angle between the donor oxygen atom, the hydrogen-bonding hydrogen atom, and the acceptor oxygen atom (OHO) is constrained to be 180° (see Table 4.2 for the coordinates of the reference structure). In this case, displacements of r_{OH} and θ_{HOH} are made while constraining all other coordinates, including the angle between the bisector of the HOH angle in the donor water molecule and the vector along the OO axis, to their values in this reference structure. These calculations provide a the potential and dipole surface, evaluated on a 5×5 grid, and five-point finite difference schemes are used to calculate the dipole derivatives used in this study.

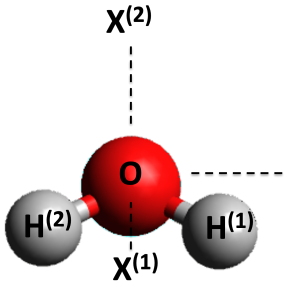

Table 4.1: Format of the Z-Matrices Used in This Study.

A	B	r_{AB}	C	θ_{ABC}	D	Ψ^a_{ABCD}
O_1						
$X_1^{(1)}$	O_1	R^b_{OX}				
$X_1^{(2)}$	O_1	R_{OX}	$X_1^{(1)}$	90		
$H_1^{(1)}$	O_1	$r_{O_1H_1^{(1)}}$	$X_1^{(1)}$	$(\theta_{H_1^{(1)}O_1H_1^{(2)}})/2$	$X_1^{(2)}$	90
$H_1^{(2)}$	O_1	$r_{O_1H_1^{(2)}}$	$X_1^{(1)}$	$(\theta_{H_1^{(1)}O_1H_1^{(2)}})/2$	$X_1^{(2)}$	-90
O_2	O_1	$R_{O_1O_2}$	$X_1^{(2)}$	$\Theta_{O_2O_1X_1^{(2)}}$	$X_1^{(1)}$	$\Psi_{O_2O_1X_1^{(2)}X_1^{(1)}}$
$X_2^{(1)}$	O_2	R_{OX}	O_1	$\Theta_{O_1O_2X_2^{(1)}}$	$X_1^{(2)}$	$\Psi_{X_2^{(1)}O_2O_1X_1^{(2)}}$
$X_2^{(2)}$	O_2	R_{OX}	$X_2^{(1)}$	90	O_1	$\Psi_{X_2^{(2)}O_2X_2^{(1)}O_1}$
$H_2^{(1)}$	O_2	$r_{O_2H_2^{(1)}}$	$X_2^{(1)}$	$(\theta_{H_2^{(1)}O_2H_2^{(2)}})/2$	$X_2^{(2)}$	90
$H_2^{(2)}$	O_2	$r_{O_2H_2^{(2)}}$	$X_2^{(1)}$	$(\theta_{H_2^{(1)}O_2H_2^{(2)}})/2$	$X_2^{(2)}$	-90
				...		

[a] Ψ_{ABCD} is defined as the angle between the plane containing atoms A, B and C, and the plane containing atoms B, C and D.

b R_{OX} defines the distance of the dummy atoms from the oxygen atom and its value is arbitrary.

Table 4.2: Internal Coordinates that Define the Reference Structures.

H_2O		$(H_2O)_2$[a]			
Coordinate	Value	Coordinate	Value	Coordinate	Value
r_{OH_1}	0.9614 Å	$r_{O_1H_1^{(1)}}$	0.9622 Å	$\Theta_{O_2O_2X_1^{(2)}}$	41.3228°
$r_{OH_2} = r_{OH_1}$	0.9614 Å	$r_{O_1H_1^{(2)}} = r_{O_1H_1^{(1)}}$	0.9622 Å	$\Theta_{O_1O_2X_2^{(1)}} = \theta_{H_2^{(1)}O_2H_2^{(2)}}/2$	52.0915°
θ^b_{HOH}	104.1116°	$R_{O_1O_2}$	2.9164 Å	$\theta_{H_2^{(1)}O_2H_2^{(2)}}$	104.1830°
		$r^b_{O_2H_2^{(1)}}$	0.9604 Å	$\Psi_{O_2O_1X_1^{(2)}X_1^{(1)}}$	180°
		$r'^b_{O_2H_2^{(2)}}$	0.9683 Å	$\Psi_{X_2^{(1)}O_2O_1X_1^{(2)}}$	180°
		$\theta^b_{H_1^{(1)}O_1H_1^{(2)}}$	104.5942°	$\Psi_{X_2^{(2)}O_2X_2^{(1)}O_1}$	90°

[a] Based on the $z-$matrix defined in Table 4.1.
[b] Coordinates that are scanned to obtain the dipole expansion.

4.2.3 Mode Coupling

To explore the possible contributions from the delocalization of the normal mode vibrational motions on the intensities of the stretch-bend transitions, we perform a series of harmonic calculations of the intensities of the transitions to the stretch-bend states in which terms are removed from the quadratic expansion of the Hamiltonian. For an isolated water molecule, this is straightforward since there are only three vibrational degrees of freedom, the two OH stretching vibrations and the HOH bending vibration. In a normal mode picture, the nominal symmetric stretching vibration contains a small contribution from the HOH bending vibration, while the bending vibration contains a small contribution from the symmetric OH stretching vibration. This could lead one to expect that some of the intensity in the stretch-bend combination transition could come from the intensity of the nominal local mode symmetric stretch or bend overtone excitation. For an isolated water molecule at the harmonic level of approximation, this can be sorted out by performing the normal mode analysis in internal coordinates (displacements of the OH bond lengths and HOH angle) and removing the off-diagonal terms in the force constant ($F-$) and Wilson $G-$matrices.[8] Such an analysis will be referred to as local mode or lm, while the full normal mode analysis is denoted as nm.

The analogous analysis for water clusters is complicated by the fact that the internal coordinates are not uniquely defined. To allow us to removed selected types of couplings from the harmonic analysis, two dummy atoms are added to each water molecule, $X^{(1)}$ and $X^{(2)}$. The first dummy atom, $X^{(1)}$, is located along the bisector of θ_{HOH}, while the second dummy atom lies directly above the oxygen atom so that the $OX^{(2)}$ vector is perpendicular to the HOH plane. This described by the $z-$matrix provided in Table 4.1 for $(H_2O)_2$, and we follow the same pattern for the larger clusters. In this way, we can separate displacements of the HOH angles and OH bond lengths, from the intermolecular motions, which include the OO distances and the relative orientations of the water molecules, which are defined in terms of the dummy atoms and the oxygen atoms.

With the coordinates defined, a series of harmonic calculations are performed based on the above choice of coordinates in which selected off-diagonal elements of the $F-$ and $G-$matrices are set to zero. These calculations include: a local mode (lm) description analogous to the one described above in which each of the OH, and HOH vibrations are decoupled from all other vibrational motions; a model in which only the OH stretching vibrations in the same water molecular are coupled (OH); a model in which the three internal coordinates in each water molecule are coupled, while the vibrations associated with different water molecules are decoupled (HOH); and finally a model in which all $3n_{\text{water}}$ intramolecular vibrations are coupled, but they remain decoupled from the intermolecular vibrations (intra). This analysis allows us to disentangle the contributions to the intensity of the stretch-bend transitions that are coming from properties of individual water molecules from those that reflect collective effects.

4.3 Results & Discussion

To explore the differences in the correlations between the intensities of the transitions to the states with one quantum of excitation in the OH stretching vibration and the corresponding stretch-bend transitions, in Figure 4.3 we plot the ratios of the calculated intensities of these two transitions when they involve the two OH bonds in the same water molecule. In this analysis, we focus on water molecules that donate one hydrogen bond, which are identified as D, AD and AAD in the inset to Figure 4.3. For a water molecule that contains one bound OH bond and one free OH bond we denote the associated transition intensities as I_{bound} and I_{free}, respectively. We find that the frequencies and intensities of the transitions associated with the free OH oscillator show little sensitivity to the hydrogen-bonding environment. This contrasts the case for the OH that forms the hydrogen bond, where transition frequency red shifts and intensity increases with increased hydrogen bond strength. As such the value of the plotted intensity ratio provides a measure of the sensitivity of the intensity of the transition involving the bound OH oscillator on the hydrogen-bonding environment. Additionally, the hydrogen bonds in these water molecules are typically stronger than those formed by water

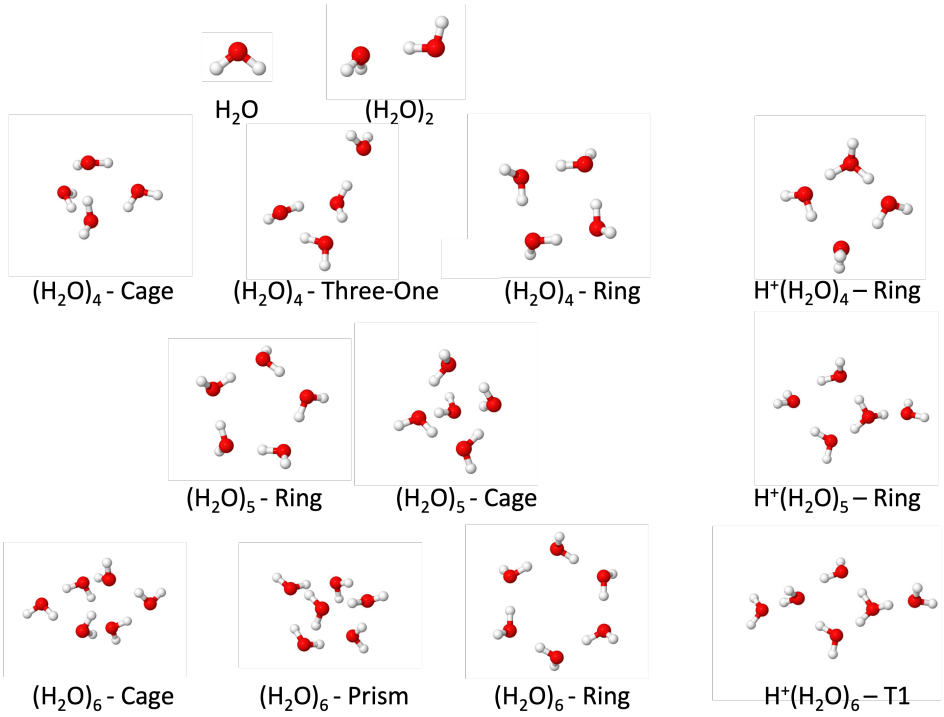

Figure 4.2: Structures of the clusters considered in these studies.

molecules that donate to two hydrogen bonds, making the OH stretching transition of the bound OH oscillator in a single donor water molecule more red-shifted and intense compared to those associated with the transitions arising from OH oscillators in water molecules that donate to two hydrogen bonds.[18,64,90] Focusing on the water molecules that donate a single hydrogen bond allows us to capture the full range of hydrogen-bonding interaction strengths.

The results plotted in Figure 4.3 illustrate the greater sensitivity of $I_{\text{bound}}/I_{\text{free}}$ for the $\Delta v_{\text{OH}} = 1$ transition compared to the corresponding intensity ratio for the stretch-bend transition. On the other hand, these results do not address the question as to why this is the case. Additionally, the calculation of the intensity ratio using displacements of r_{OH} and θ_{HOH}, as described in our earlier study and in the Supporting Information, does not fully account for mode coupling or anharmonicities.[31] To understand the origin of the insensitivity of the intensities of the stretch-bend transitions to the hydrogen-bonding environment, we will

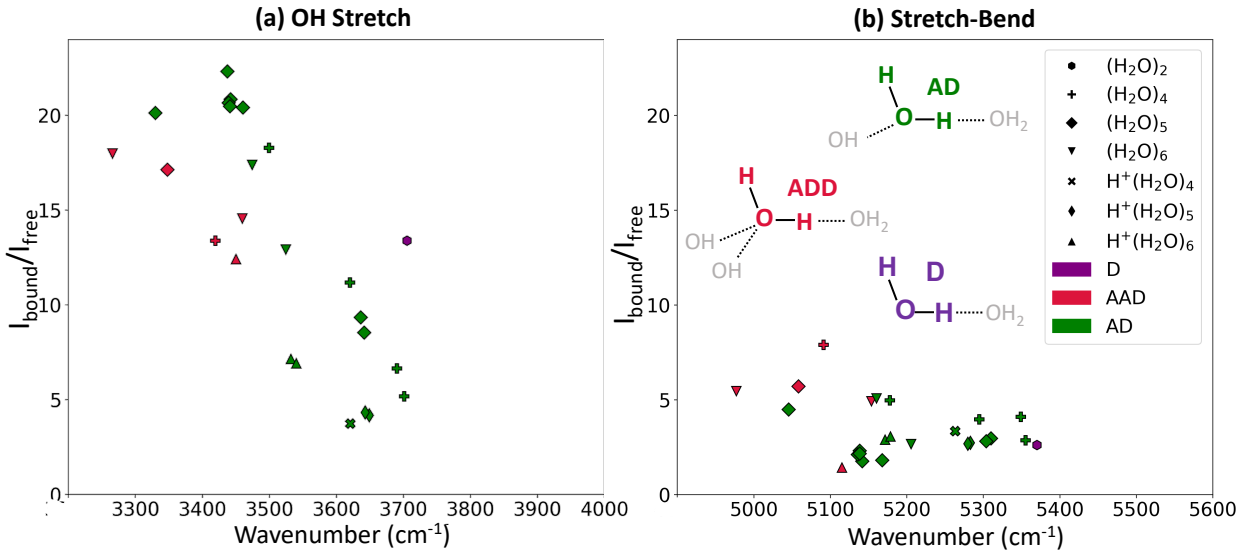

Figure 4.3: Comparison of the ratios of the intensities of transitions involving a bound OH bond (I_{bound}) to a free OH bond (I_{free}) in a single water molecule for transitions to the state with (a) one quantum of excitation in the OH stretch and (b) one quantum of excitation in both the OH stretch and HOH bend, plotted as functions of the calculated harmonic frequencies of the transitions. The markers indicate size of the water clusters (see Figure 4.2 for the isomers studied), while purple symbols indicate single donor water molecules (D), green symbols are used for water molecules that form and accept one hydrogen bond (AD), and red symbols indicate water molecules in AAD environments (see inset in panel(b)).

start by exploring the role of the higher order terms in the expansion of the dipole moment and potential in determining the intensities of the stretch-bend transitions. We also explore how much of this effect can be captured by a fixed-charge model of the dipole moment, and the possible role of changes in the charge distribution with OH stretching vibration in determining the intensities of these transitions. Often the normal mode vibrations in both isolated water molecules and assemblies of water molecules are not well-described as the motion of a single OH stretching or HOH bending vibration, and we will conclude this discussion by probing the role of mode mixing at the harmonic level on the understanding of these intensity patterns.

4.3.1 Higher Order Terms in the Potential and Dipole Surfaces

The usual starting point for calculating intensities of vibrational transitions is the linear dipole/harmonic oscillator approximation, which is based on a quadratic expansion of the potential surface and a linear expansion for the dipole moment surface. These choices reflect the lowest order non-zero terms in the expansions of these functions. This pair of approximations predicts only transitions that change the number of quanta in one oscillator by one. As a result, within these approximations the intensity of any two quanta transition is zero. The intensity of two quanta transitions will arise from some combination of higher order terms (or anharmonicity) in the expansion of either the potential (mechanical) or the dipole (electrical) surface. To explore the contributions of these two effects on the calculated intensity for the stretch-bend transition, in Table 4.3 we report the intensity of the stretch-bend transition based on various orders of expansion of the two-dimensional dipole moment surface up to second order using the full two-dimensional potential surface. For these calculations, both the potential and dipole surfaces are evaluated as functions of one of the OH bond lengths and the HOH angle at the MP2/aug-cc-pVTZ level of theory/basis as implemented in Gaussian 16[3] using the Hamiltonian and dipole surfaces described by Eqs. 4.2 and 4.5, respectively. We also report the results when the full two-dimensional dipole surface is used with the full potential (Full/Full) and when second order expansions of the

Table 4.3: Calculated Intensities (in km mol^{-1}) for the Stretch-Bend Transition Based on the Two-Dimensional Model.

Potential Dipole	Full[a] Full[b]	Full 1st + 2nd[c]	Full 1st + 2nd-B[d]	Full 1st	Full 2nd-B[e]	2nd 2nd
H_2O	1.67	1.67	1.65	0.262	1.12	1.24
$(H_2O)_2$ free	2.91	3.01	2.93	0.198	2.34	2.68
$(H_2O)_2$ bound	5.02	4.93	5.93	0.675	3.15	2.51

[a] Calculated using the two-dimensional potential energy surface, evaluated at the MP2/aug-cc-pVTZ level of theory/basis.
[b] Calculated using the two-dimensional dipole surface, evaluated at the MP2/aug-cc-pVTZ level of theory/basis.
[c] Calculated using $\vec{\mu}_{1\text{st}}$, $\vec{\mu}_{2\text{nd}-\text{B}}$, and $\vec{\mu}_{2\text{nd}-\text{D}}$ in Equation 4.5.
[d] Calculated using $\vec{\mu}_{1\text{st}}$ and $\vec{\mu}_{2\text{nd}-\text{B}}$ in Equation 4.5.
[e] Calculated using only $\vec{\mu}_{2\text{nd}-\text{B}}$ in Equation 4.5.

potential and dipole surfaces are used (2nd/2nd). Comparing the intensities obtained using the second order expansions of the potential and dipole surfaces to those obtained when the full surfaces are used, we find this quadratic approximation captures between 50% and 92% of the calculated intensity for the three OH bonds considered in Table 4.3. Notably, the largest differences are found for the bound OH in $(H_2O)_2$.

Focusing on the isolated water molecule, and looking at how the calculated intensity changes as various terms are added to the expansion, it is clear that the bilinear terms in the second order dipole expansion (Full/2nd-B) provide the leading contribution. When the intensity obtained using the Full/2nd-B approximation is compared to the results obtained using a higher order expansion of the dipole moment surface (Full/Full), we find that taken alone this term accounts for two thirds of the calculated intensity. TThe terms that have the next most important contribution are the first order terms in the expansion of the dipole surface, and the contribution from $\partial\vec{\mu}/\partial\theta_{\text{HOH}}$ is slightly larger than the $\partial\vec{\mu}/\partial r_{\text{OH}}$ term. That these terms contribute to the calculated intensity of the stretch-bend transition reflects anharmonicity in the wave function, or mechanical anharmonicities. While the calculated intensity is small when only the linear terms in the expansion of the dipole moment are

considered (Full/1st), these terms cause a notable increase in the calculated intensity when combined with the second-order bilinear term in the expansion of the dipole moment (Full/1st + 2nd-B compared to Full/2nd-B). Finally, the contribution from $\vec{\mu}_{\mathrm{2nd-D}}$ is small for H_2O (Full/1st + 2nd compared to Full/1st + 2nd-B).

Moving from an isolated water molecule to $(H_2O)_2$, allows us to consider the effects of hydrogen bonding on the above observations by comparing the results for the bound OH and free OH bonds in the donor water molecule. The sizes of the various contributions to the intensity for the transitions involving the free OH bond closely follow the trends discussed above for stretch-bend transitions involving a single OH bond in an isolated water molecule. When we compare the intensity of the stretch-bend transition involving bound OH to that of the free OH, we find that while the intensities for the transitions involving the bound OH are larger than those involving the free OH, the differences are generally smaller than a factor of two. Interestingly, when quadratic expansions of the potential and dipole surface are used (2nd/2nd), the two intensities are nearly identical. As with an isolated water molecule, most of the calculated intensity of the stretch-bend transition involving the bound OH is captured when a quadratic expansion of the dipole surface is used, and the leading contribution comes from the bilinear term in the quadratic expansion of the dipole moment.

Closer examination of the contributions to the intensity of the stretch-bend transition involving the bound OH stretch shows that the terms that involve first and second derivatives of the dipole moment with respect to the OH stretching vibration are larger than those involving the derivatives with respect to bending vibration. The importance of the terms in $\vec{\mu}_{\mathrm{2nd-D}}$ in determining the magnitude of the matrix element of the dipole moment function reflects the couplings (both quadratic and higher order) between the OH stretching vibrations and the HOH bending vibrations. The first derivative of the dipole moment with respect to the bound OH stretching vibration is much larger than the corresponding derivative with respect to the free OH. As Kjaergaard *et al.* showed for the two quanta transition that involves the bound OH stretch in $(H_2O)_2$, the first and second derivatives of the dipole moment with respect to r_{OH} for the bound OH have opposite signs, while the derivatives

with respect to r_{OH} for the free OH have the same signs.[96] In that work, the authors used this difference in signs of the linear and quadratic terms in the expansion of the dipole moment to explain the similarity of the overtone intensities for the bound OH and free OH stretches in $(H_2O)_2$. A similar argument can be used to understand why the introduction of the first and second derivatives with respect to the OH stretching vibration in the expansion of the dipole moment change the relative intensities of the stretch-bend transitions in the free OH and bound OH.

4.3.2 Changes in the Charge Distribution

The above analysis revealed the importance of the inclusion of the bilinear terms in the expansion of the dipole surface in the calculation of the stretch-bend intensity, but did not explain the lower sensitivity of the magnitude of this term to the hydrogen-bonding environment compared the corresponding $\partial\vec{\mu}/\partial r_{OH}$ term. Both the bilinear term and the $\partial\vec{\mu}/\partial r_{OH}$ term in the expansion of the dipole contain two contributions. The first reflects the changes in the dipole moment due to the displacement of the atoms, each of which can be considered to have a constant partial charge. In addition to this fixed-charge contribution, the charge distribution will change with the displacement of atoms. The second of these contributions will be particularly notable when hydrogen bonds are broken. This change in the charge distribution can be accounted for by adjusting the partial charges on the original atoms, and results in what Nesbitt and co-workers have referred to as charge sloshing.[40,97,98] Such charge sloshing is anticipated to be partially responsible for the loss of sensitivity of the intensity of the stretch-bend transition to the hydrogen-bonding environment, compared to the corresponding OH stretch intensity. To more fully understand the origins of this behavior we explore the contributions from displacements of fixed charges and charge sloshing to the second derivatives of the dipole moment with respect to r_{OH} and θ_{HOH}. The results of this analysis are plotted in Figure 4.4.

As described above, the charges used for the fixed-charge model are developed to reproduce the dipole moment of the reference structures of H_2O and $(H_2O)_2$, and their values

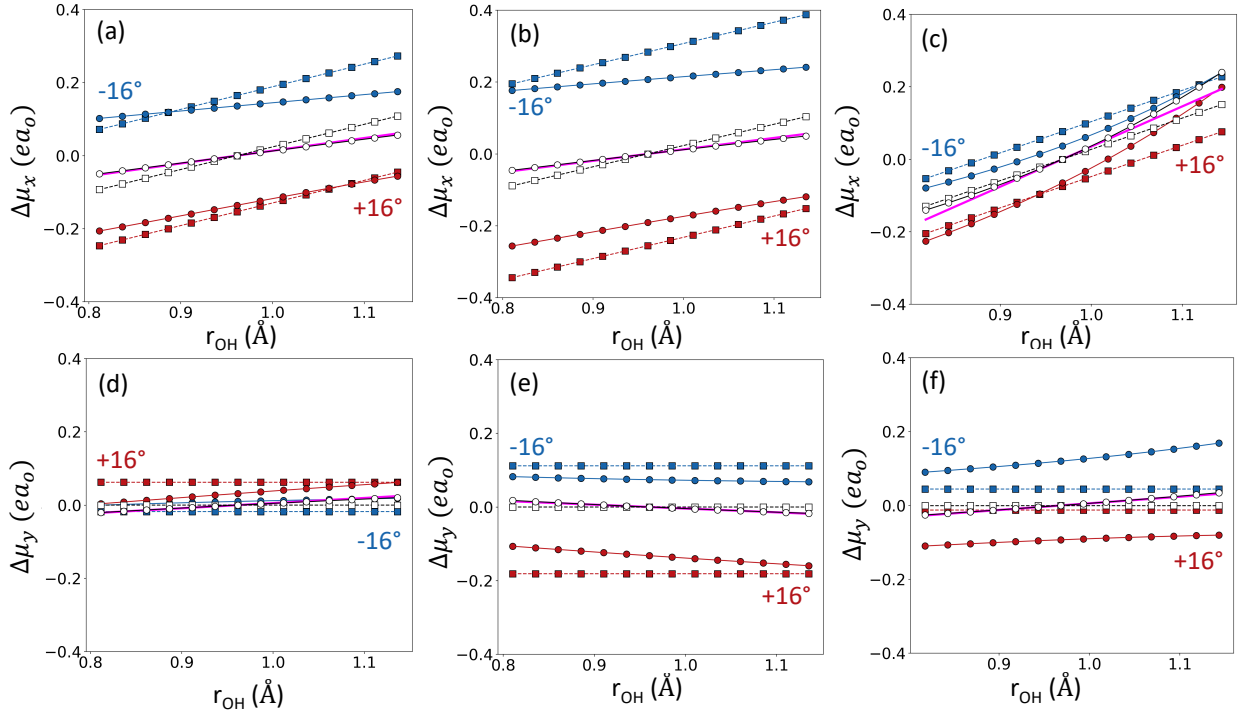

Figure 4.4: Comparison of the change in the components of the dipole moment from their values in the reference structure as r_{OH} is stretched. The $x-$axis is along the OH bond of interest and the $y-$axis is in symmetry plane of the molecule. The values of μ_x for the reference structures are (a) 0.4498 ea_0, (b) -0.2837 ea_0, and (c) 1.176 ea_0, and the corresponding values of μ_y are (d) -0.5769 ea_0, (e) 1.142 ea_0, and (f) -0.0047 ea_0. Circles/solid lines provide the results obtained using the dipole function, while squares/dashed lines provide the results obtained using the fixed charge model. The color of the marker denotes the value of the θ_{HOH} angle, where white symbols are evaluated at the value of θ_{HOH} in the reference structure, data plotted in blue are evaluated at configurations for which θ_{HOH} is decreased by 16° and results plotted in red were evaluated at geometries for which θ_{HOH} has been increased by 16°.

Table 4.4: Values of the Fixed Charges Used in These Studies.

	O	H
H_2O	-0.3274	0.1637
$(H_2O)_2$-A[a]	-0.3268	0.1634
$(H_2O)_2$-D[b]	-0.7698	0.4568[c] 0.3129[d]

[a] Acceptor water molecule in $(H_2O)_2$.
[b] Donor water molecule in $(H_2O)_2$.
[c] Charge of the H in the bound OH.
[d] Charge of the H in the free OH.

are reported in Table 4.4. To simplify comparisons among the three OH bonds investigated, specifically the OH bond in an isolated water molecule and the two OH bonds in the donor water molecule in $(H_2O)_2$, we plot the difference between the vector components of the calculated dipole moment and their values in the reference structure. For this analysis we define the $x-$axis to lie along the OH bond that is being displaced, while the $y-$axis lies in the symmetry plane of the system. It should be noted that these definitions result in different coordinate systems for the two OH bonds in $(H_2O)_2$. The $x-$ and $y-$ components of the dipole moment that are obtained using these fixed charges with other coordinates constrained to their values in the reference structure are plotted as a function of r_{OH} with white squares and dashed black lines in Figure 4.4. For comparison, we also plot the changes in the vector components of the dipole moment calculated at the MP2/aug-cc-pVTZ level of theory/basis with white circles and solid black lines. The pink lines provide the values of the dipole moment when it is approximated by a linear expansion in the displacement of r_{OH} from its value in the reference structure (see Table 4.2). In $(H_2O)_2$ both of the OH vectors are rotated by the same amount, so as not to change the value of the angle between the bisector of θ_{HOH} for the donor water molecule and the vector along the OO axis.

For isolated water and the free OH in $(H_2O)_2$ (Figure 4.4 (a), (b), (d) and (e)), the fixed charge model overestimates the slope of the dipole moment, which is consistent with

a decrease in the partial charges of the hydrogen atoms as the OH bond dissociates to form a hydrogen atom and an OH radical, both of which are neutral. Additionally, the dipole components closely follow the linear approximation (shown by comparing the white circles to the pink line). When we consider the bound OH in $(H_2O)_2$ (Figure 4.4(c) and (f)), we find that the fixed charge on the bound OH is larger than on the free OH. In this case, the fixed-charge model underestimates the slope of the dipole moment, and the cut through the dipole surface shows greater deviations from linearity than are seen for the free OH in $(H_2O)_2$ and the OH bond in an isolated water. The partial charge on the hydrogen atom in the bound OH increases as r_{OH} is increased, as the extension of this OH bond can result in proton transfer.

While these observations can be used to rationalize the increased intensity of the $\Delta v_{\mathrm{OH}} = 1$ transition involving the bound OH with increased hydrogen-bond strength, they do not explain the observation that the intensity of the corresponding stretch-bend transition does not show a strong correlation to the strength of the hydrogen-bond. To address this question we need to consider the change in the slope of the cuts through the dipole surface along r_{OH} as we change the value of θ_{HOH}. These results are plotted with red and blue circles and solid lines for displacements of θ_{HOH} by $+16^\circ$ and -16°, respectively. The corresponding results obtained using the fixed-charge model are shown with squares and dashed lines of the same colors. The fixed-charge model predicts cuts through the dipole surface that are shifted, all of which have the same slope. Comparing the slopes of cuts through the dipole surface to those obtained using the fixed-charge model shows that $\partial\vec{\mu}/\partial r_{\mathrm{OH}}$ decreases non-linearly with increasing θ_{HOH}. This decrease in the value of the slope with θ_{HOH} reflects the balance of two factors. Specifically, as θ_{HOH} in an isolated water molecule approaches 180° the dipole moment will approach 0, by symmetry. At the same time, the partial charges on the hydrogen atoms increase with increasing θ_{HOH}. Since the calculated dipole moment increases more with θ_{HOH} than is predicted by the fixed-charge model, the changes in the charge distribution provides the leading contribution to the θ_{HOH} dependence of the dipole moment.

The situation is slightly more complicated for the bound OH and the $y-$component of the dipole moment for the free OH bond in $(H_2O)_2$ as displacement of θ_{HOH} breaks the hydrogen bond, leading to additional factors that will affect the size of the dipole moment. This can be seen most clearly in Figure 4.4(c), where the slope of the cuts through the dipole moment also increase with increased θ_{HOH}. Breaking the hydrogen bond will decrease the partial charge on the hydrogen atom in the bound OH, partially canceling the increase in this partial charge with θ_{HOH} in an isolated water molecule. It is the cancellation of these effects that leads to the observed lowered sensitivity of the intensity of stretch-bend transitions compared to the transitions to states with one quantum of excitation in the OH stretch. Previously, the effect of the change in the charge distribution with change in θ_{HOH} has been studied in the context of the effects on the transition to the state with one quantum of excitation in the θ_{HOH} bend.[99] This work led to the incorporation of a nonlinear dipole moment surface into the TTM3-F potential surface.[100]

4.3.3 Mode Coupling

The above analysis focused on the coupling between local OH stretching and HOH bending vibrations. If we consider the normal modes of a water molecule, the vibrations are often collective. Even when we only consider the quadratic expansion of the Hamiltonian for an isolated water molecule the OH stretching normal modes contain some bend character while the bend normal mode contains some OH stretching character. As we move from a single water molecule to water clusters, the situation is further complicated as stretching and bending vibrations from two or more water molecules can contribute to a single normal mode. The limitations of using a local mode model to analyze the role of mode couplings can be seen in the results of a study of the transition frequencies and intensities of transitions in water and water dimer with up to three and two quanta of excitation, respectively, reported by Kjærgaard *et. al.*[17] In that work, the authors compared frequencies and intensities obtained using a harmonically coupled anharmonic oscillator (HCAO) model in which the quadratic couplings between the OH stretches and the HOH bends were not included to those

Table 4.5: Frequencies (in cm^{-1}) and Intensities (in km mol^{-1}) of the Transitions Analyzed in This Study Using Various Coupling Models[a] for H_2O.

	lm		OH		nm	
Mode[b]	ν	I	ν	I	ν	I
B	1648.54	68.84	1648.53	68.84	1628.38	71.68
S1	3887.85	40.26	3828.00	6.05	3821.87	5.56
S2	3887.85	40.26	3947.69	75.46	3947.69	75.46
S1 + B	5536.39	1.16	5476.54	0.13	5450.25	0.11
S2 + B	5536.39	1.16	5596.22	2.15	5576.07	2.28

[a] See text for details.
[b] S and B represent OH stretches and HOH bend; modes are numbered in increasing frequency.

obtained from VPT2 calculations. When they considered the intensities of the stretch-bend transitions in $(H_2O)_2$, they found that the HCAO model predicts that the oscillator strength for the stretch-bend transition involving the free OH to be larger than the corresponding transition that involves the bound OH. This result is in contrast to the results of VPT2 calculations, also reported in that study, and the results we obtain from the fully-coupled two-dimensional model. This leads us to expect that the mixing of the OH stretching and HOH bending vibrations will contribute to the intensities of the stretch-bend transition. Indeed we find that there are small changes in the calculated intensities of the stretch-bend transitions for an isolated water molecule obtained when only the OH stretches are coupled (OH) compared to the results of a normal mode calculation (nm) (see Table 4.5).

To explore the effects of mode-mixing, we focus on calculations based on quadratic expansions of the potential and dipole surfaces, where the expansions are preformed in the $3n_w$ intramolecular vibrations (OH stretching and HOH bending) of each water molecule, the OO distances and six coordinates that describe the spacial orientations of the water molecules in the cluster. In performing this analysis, we selectively remove some of quadratic coupling terms in the Hamiltonian. The results of this analysis for $(H_2O)_2$ are presented in Figure 4.5.

Focusing on the upper and lower panels of Figure 4.5, we can compare the harmonic spectra in the stretch-bend region when all of the vibrations are decoupled (local mode, or lm) and when we include all quadratic couplings (normal mode, or nm). There are clear differences, mainly resulting from forming the in- and out-of-phase combinations of the two OH stretching vibrations on the same water molecule. As for an isolated water molecule, the stretch-bend transition involving out-of-phase combination of the OH stretching vibrations has larger intensity than the one involving the in-phase combination of these two vibrations. This leads to the increase in intensity of the highest frequency transition and the very weak feature near 5420 cm^{-1}, both of which correspond to the middle peak in the turquoise spectrum (lm) and reflect stretch-bend transitions in the acceptor water molecule. While the two OH bonds in the donor water molecule are not equivalent, the highest frequency vibration can be considered to mainly involve the free OH bond, in an out-of-phase combination with the bound OH bond. This explains the increase in intensity of this transition when the coupling between these two OH stretching vibrations is considered. Finally, the lowest frequency peak in the normal mode spectrum (blue spectrum, nm) primarily reflects motions of the bound OH bond, in an in-phase combination with the free OH bond, explaining the decrease in the intensity of this transition compared to the local mode spectrum.

The remaining four panels illustrate what happens when only some of the quadratic terms that couple the local mode vibrations are considered. For example, in the second plot, we only consider couplings between the OH stretching vibrations in the same water molecule (OH, magenta spectrum). This spectrum is remarkably similar to the one obtained using the full normal mode treatment. On the other hand, if we couple the bending vibrations among all of the water molecules (bnd, yellow spectrum), while leaving the OH stretching vibrations decoupled, the spectrum reproduces the one obtained using the local mode treatment. The remaining two spectra reflect the results of analyses when we include terms that couple stretching and bending vibrations within the individual water molecules (HOH, red spectrum) and when we include the couplings between all of the high frequency stretching and bending vibrations (intra, green spectrum). For $(H_2O)_2$, these two spectra are both

nearly identical to the normal mode spectrum plotted in blue. Closer examination of the intensities, show that when only the OH stretching vibrations are allowed to couple, the peak associated with the stretch-bend transition involving the free OH has a larger intensity compared to the corresponding transition involving the bound OH, which is consistent with the results of the HCAO calculations reported by Kjærgaard *et. al.*[17]

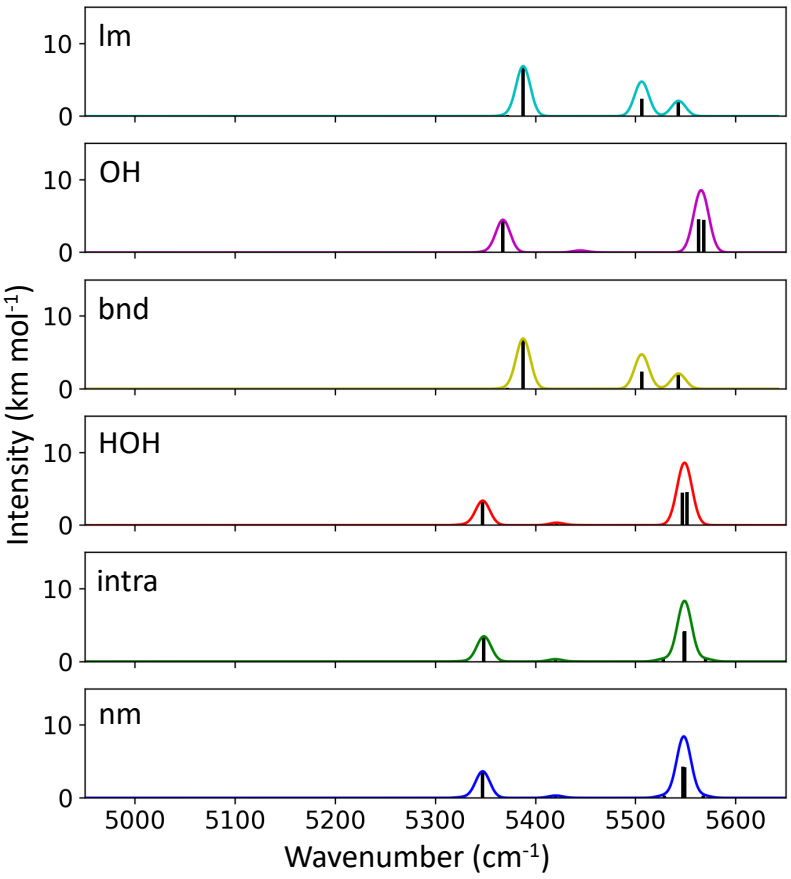

Figure 4.5: Calculated spectra of the stretch-bend region for $(H_2O)_2$ using varying levels of coupling in the vibrational Hamiltonian. From top to bottom: local mode model (lm), vibrational coupling between the OH stretches only (OH), vibrational coupling between bends only (bnd), vibrational coupling within an individual water molecule (HOH), vibrational coupling of all 6 high frequency modes (stretches and bends) (intra), normal mode model (nm). All calculated transitions are plotted as sticks and then convoluted with Gaussian functions with a width of 10 cm^{-1}.

We have repeated this analysis for larger clusters, and in Figures 4.6 and 4.7 we present the simulated spectra in the stretch-bend region for several isomers of $(H_2O)_4$ and $(H_2O)_6$, respectively. In these plots we sum the spectra for multiple isomers to illustrate the general trends and the structures of the isomers can be found in Figure 4.2. Comparing the spectra obtained using different models, we notice the spreading of the intensity when we include the couplings of the OH stretching and HOH bending vibrations within a singular molecule (HOH, red spectrum), although the largest difference in intensity comes from the inclusion of the couplings among OH stretching and HOH bending vibrations of different water molecules. This leads to a broadening and merging of the individual peaks and results in a spectrum that more closely resembles the spectrum of liquid water in the stretch-bend region (see Figure 4.1). In the local mode model (lm, turquoise spectrum) there are often near-degeneracies, which result in narrower more intense peaks in the calculated spectrum. As couplings are added these degeneracies are lifted and the intensity becomes more evenly distributed over the spectral region. On the other hand, the total integrated intensity remains roughly constant, providing further validation for the use of the local mode model for exploring the leading contributions to the intensity in the stretch-bend region of the spectrum.

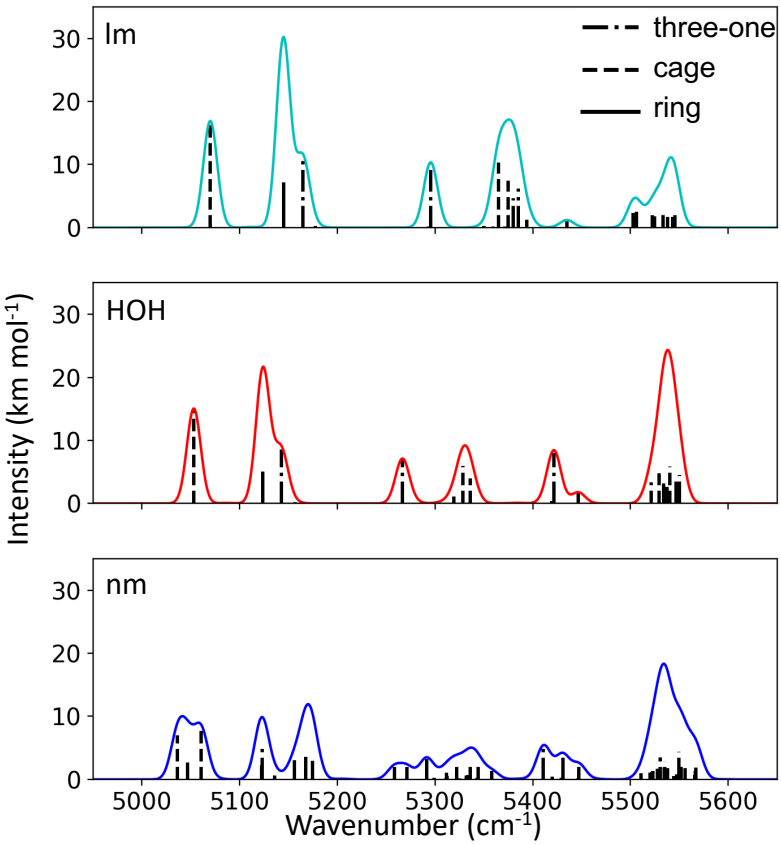

Figure 4.6: Calculated spectra of the stretch-bend region for $(H_2O)_4$ using varying levels of coupling in the vibrational Hamiltonian. Here we show the spectra of three isomers of $(H_2O)_4$ (three-one, cage, and ring as shown in Figure 4.2), plotted in different line styles in each panel. From top to bottom: local mode model (lm), vibrational coupling within an individual water molecule (HOH), and normal mode model (nm). All calculated transitions are plotted as sticks and then convoluted with Gaussian functions with a width of 10 cm^{-1}.

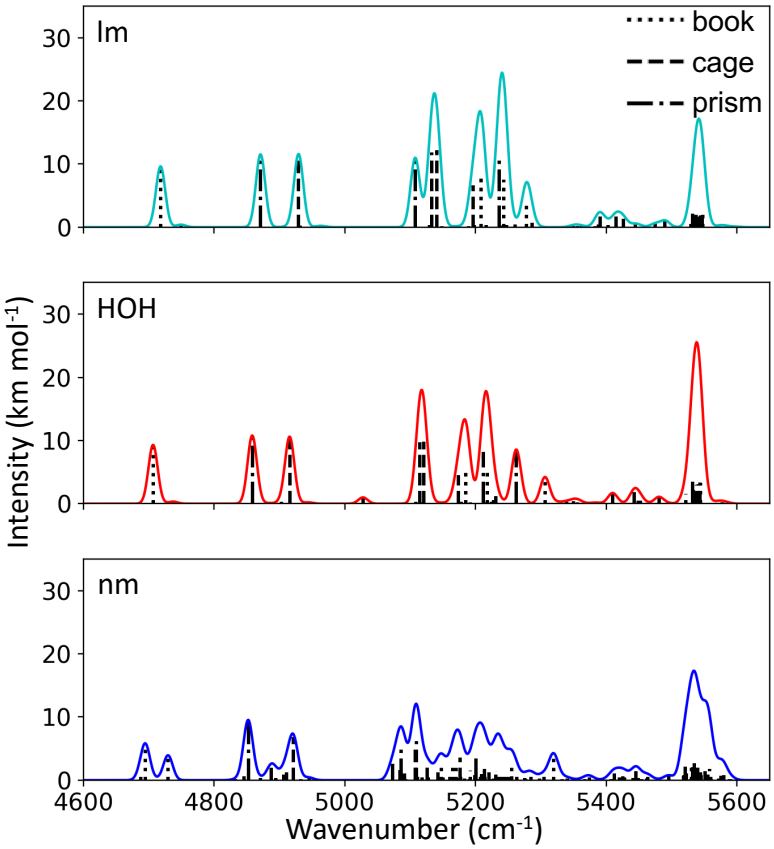

Figure 4.7: Calculated spectra of the stretch-bend region for $(H_2O)_6$ using varying levels of coupling in the vibrational Hamiltonian. Here we show the spectra of three isomers of $(H_2O)_6$ (book, cage, and prism as shown in Figure 4.2), plotted in different line styles in each panel. From top to bottom: local mode model (lm), vibrational coupling within an individual water molecule (HOH), and normal mode model (nm). All calculated transitions are plotted as sticks and then convoluted with Gaussian functions with a width of 10 cm^{-1}.

4.4 Conclusions

In this study, we explored the origins of the intensity of transitions to states with one quantum of excitation in the OH stretch and one in the HOH bend in the same water molecule. The intensity of this transition has been shown to be much less sensitive to the hydrogen-bonding environment compared to the transition to the state with one quantum in the same OH stretching vibration. We confirmed that the leading contribution to the intensity of this transition comes from the second derivative of the dipole moment with respect to r_{OH} and θ_{HOH}. There are also notable contributions to the intensity from the $\partial\vec{\mu}/\partial r_{\mathrm{OH}}$ and $\partial\vec{\mu}/\partial\theta_{\mathrm{HOH}}$ terms in the expansion of the dipole moment. These corrections reflect the anharmonicity in the vibrational wave function. The magnitude of the $\partial\vec{\mu}/\partial r_{\mathrm{OH}}$ contribution increases significantly with hydrogen-bond strength. It is also partially cancelled by contributions from the corresponding $\partial^2\vec{\mu}/\partial r_{\mathrm{OH}}^2$ term in the expansion of the dipole moment. This partial cancellation has similar origins to the loss of intensity of the first overtone in the bound OH stretching vibrations compared to the intensity of transitions that involve the free OH.[96] While this helps to explain the observed insensitivity of the intensity of the stretch-bend transition to the hydrogen-bonding environment, it does not explain why $\partial^2\vec{\mu}/\partial r_{\mathrm{OH}}\partial\theta_{\mathrm{HOH}}$ also appears to be relatively insensitive to the hydrogen-bonding environment.

To address this question, we explored the changes in the charge distribution in H_2O and $(H_2O)_2$ when r_{OH} and θ_{HOH} are displaced from their values in their reference structures. We showed that there is a partial cancellation between the increase of the partial charges on the hydrogen atoms with increased values of θ_{HOH} and the decrease in the partial charge on the bound hydrogen atom when the hydrogen bond is broken when θ_{HOH} is changed. Finally, we explore how mode couplings affect the above observations.

As noted above, looking at the impact of hydrogen bonding on multiple regions of the spectrum of water and water clusters provides complementary insights into the distributions of hydrogen-bonding environments that are sampled by the system. The stretch-bend region, which is the focus of the present study, is of particular interest due to the weak correlation

between the intensity of the individual transitions in this region and the hydrogen-bonding environment. This allows one to extract the distribution of hydrogen-bonding geometries directly from the contour of the band in the 5200 cm^{-1} region of the vibrational spectrum.

Chapter 5

ACTION SPECTROSCOPY OF *TERT*-BUTYL HYDROPEROXIDE AND A HYDROPEROXYALKYL RADICAL ($^{\bullet}$QOOH) WITH THEORETICAL INSIGHTS INTO THE COUPLING OF TORSION AND OH-STRETCHING

Reproduced in part from [Anne S. Hansen, Rachel M. Huchmala, Emil Vogt, Mark A. Boyer, Trisha Bhagde, Michael F. Vansco, Casper V. Jensen, Alexander Kjærsgaard, Henrik G. Kjærgaard, Anne B. McCoy, and Marsha I. Lester. Coupling of Torsion and OH-Stretching in Tert-Butyl Hydroperoxide. I. The Cold and Warm first OH-Stretching Overtone Spectrum. *J. Chem. Phys.* **2021**, 154 (16), 164306.] and [Anne S. Hansen, Trisha Bhagde, Yujie Qian, Alyssa Cavazos, Rachel M. Huchmala, Mark A. Boyer, Coire F. Gavin-Hanner, Stephen J. Klippenstein, Anne B. McCoy, and Marsha I. Lester. Infrared Spectroscopic Signature of a Hydroperoxyalkyl Radical ($^{\bullet}$QOOH). *J. Chem. Phys.* **2022**, 156 (1), 014301] with the permission of AIP Publishing.

5.1 Introduction

Oxidation of volatile organic compounds (VOC) in the atmosphere and hydrocarbon fuels in low temperature combustion (<1000 K) proceeds through a well-established series of radical reactions shown in Figure 5.1.[101–103] These reactions are generally initiated by hydroxyl radicals (OH) via abstraction or addition to form an alkyl radical ($R^{\bullet}$) that reacts rapidly with O_2 to produce an alkylperoxy radical ($ROO^{\bullet}$). $ROO^{\bullet}$ can undergo internal hydrogen abstraction (H-shift) to form a transient carboncentered hydroperoxyalkyl radical intermediate, commonly known as $^{\bullet}$QOOH, composed of a hydroperoxide group (-OOH) and a new carbon radical center ($^{\bullet}$Q).[5,101,102,104–108] The $^{\bullet}$QOOH intermediate can isomerize back to $ROO^{\bullet}$, decay to release OH radical and cyclic ether products (chain-propagation), or

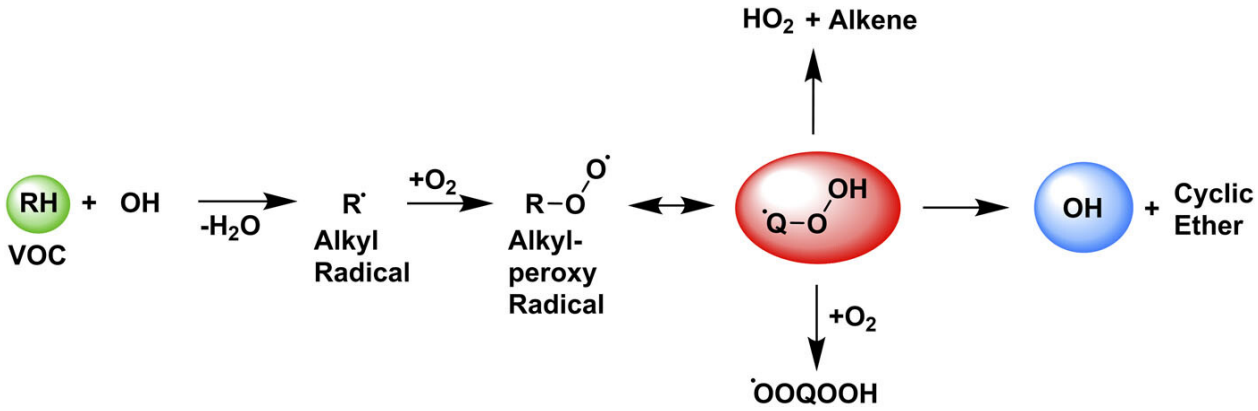

Figure 5.1: Oxidation of volatile organic compounds (VOC, RH) can consume and regenerate OH radicals. An alkyl radical ($R^{\bullet}$), generally formed by OH abstraction or addition, subsequently reacts with O_2 to produce an alkylperoxy radical ($ROO^{\bullet}$), which undergoes an internal hydrogen shift (reversible) to produce the carbon-centered hydroperoxyalkyl radical ($^{\bullet}QOOH$). Unimolecular decay of the $^{\bullet}QOOH$ radical yields OH radical and cyclic ether or HO2 and alkene products. Alternatively, $^{\bullet}QOOH$ can react with O_2 to produce $^{\bullet}OOQOOH$.

form HO_2 and alkene products (chain-termination).[5,104,107,109–114] In addition, the $^{\bullet}QOOH$ radical reacts readily with O_2 to produce $^{\bullet}OOQOOH$, a reaction that typically competes with unimolecular decay of $^{\bullet}QOOH$. $^{\bullet}OOQOOH$ can undergo internal hydrogen abstraction (H-shift) and repeated dissociations to ultimately produce several OH radicals (chainbranching).[5,101,112,115–117] Alternatively, the addition of O_2 to the hydroperoxyalkyl radical, producing $^{\bullet}OOQOOH$, and subsequent intramolecular H-shift can be repeated multiple times to generate more highly-oxygenated organic molecules relevant to the formation of secondary organic aerosols.[101,118] Despite the central role of $^{\bullet}QOOH$ radicals in the oxidation mechanism, experimental studies of $^{\bullet}QOOH$ are extremely limited. Most prior experimental studies have focused on product detection and/or indirect kinetic measurements, such as the rate of appearance of OH products.[104,105,109,119–122] By contrast, theoretical investigations have mapped out possible decay channels and the associated transition state (TS) barriers for a wide range of $^{\bullet}QOOH$ radicals.[5,104–107,123,124]

Three conformers of $^{\bullet}$QOOH (Figure 5.2) are predicted with relative energies of $^{\bullet}$QOOH1 (0 kcal mol^{-1}), $^{\bullet}$QOOH2 (0.5 kcal mol^{-1}), and $^{\bullet}$QOOH3 (0.7 kcal mol^{-1}).[4] COOH torsion (τ) connects $^{\bullet}$QOOH1 and $^{\bullet}$QOOH2 with an isomerization barrier of only 0.9 kcal mol^{-1}, while CCOO torsion connects all three conformers with barriers of 5.4–5.7 kcal mol^{-1}. Because our 2+1 model includes the COOH torsion and not the CCOO torsion, we focus on the $^{\bullet}$QOOH1 and $^{\bullet}$QOOH2 conformers in this work.

We present the infrared (IR) spectroscopic fingerprint of the stabilized $^{\bullet}$QOOH radical 2-hydroperoxy-2-methylprop-1-yl [$^{\bullet}CH_2(CH_3)_2COOH$], which is transiently formed in the oxidation of isobutane or other branched hydrocarbons.[5,104,119,123,124] Recently, this laboratory demonstrated that this $^{\bullet}$QOOH radical, when generated by H-atom abstraction from *tert*-butyl hydroperoxide (TBHP), could be stabilized and cooled in a supersonic jet expansion.[4] The $^{\bullet}$QOOH radical was activated via IR excitation, which provided sufficient energy for $^{\bullet}$QOOH to surmount or tunnel through the TS barrier leading to OH and cyclic ether products. Due to this, we also compare the spectrum in the first-overtone OH-stretching ($2v_{OH}$) region, collected using under jet-cooled conditions using multiphoton infrared (IR) excitation which forms OH radical products that are then detected by laser-induced fluorescence (LIF).[32] Since TBHP is a precursor to $^{\bullet}$QOOH, we use both to develop the models used in the theoretical studies of the OH-stretching and COOH-torsion motions of the molecules.

The model used for analysis of the spectroscopic signals of TBHP and $^{\bullet}$QOOH is analogous to a two dimensional model previously used to explain higher overtone spectra of the OH stretch, which provided a consistent interpretation of the observed spectra and predicted previously unobserved transitions.[125] The picture that emerged based on the adiabatic model was that the many features observed in OH overtone spectra of hydroperoxides could be understood based on only these two vibrations, even for molecules the size of TBHP, which has 42 vibrational modes. This model follows the empirical adiabatic two dimensional local mode (LM) model that includes the high frequency OH stretch and low frequency COOH torsion presented in Likar *et. al.*[126]

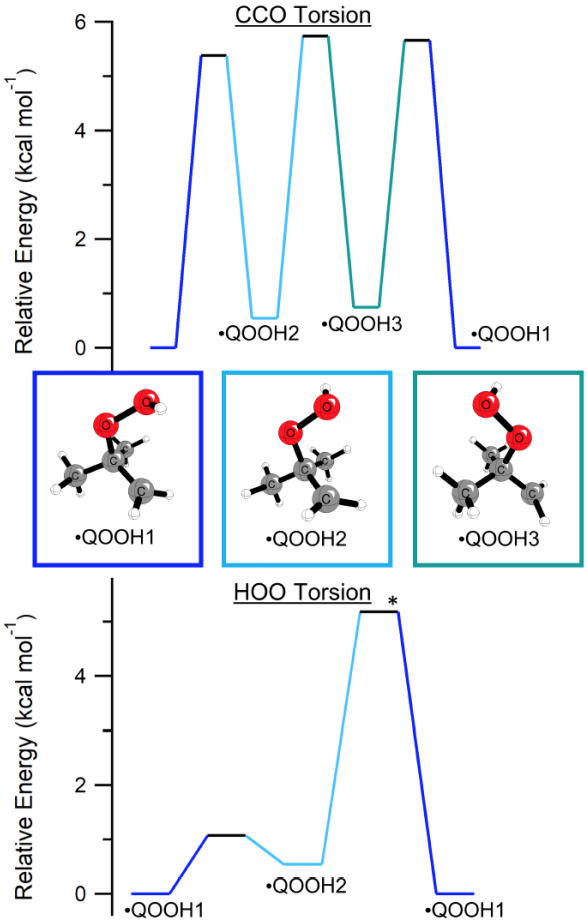

Figure 5.2: Torsional landscape for •QOOH conformers. Stationary points for •QOOH conformers with relative energies of •QOOH1 (0 kcal mol^{-1}), •QOOH2 (0.5 kcal mol^{-1}), and •QOOH3 (0.7 kcal mol^{-1}) are connected via torsion about the CO (left) and OO (right) bonds.[4] The torsional motion around the CO bond connects all three •QOOH conformers, while that around the OO bond connects •QOOH1 and •QOOH2. Energies are calculated with the UCCSD(T)-F12/cc-pVTZ-F12//B2PLYP-D3/cc-pVTZ method/basis except for the transition state marked with * where CCSD(T)-F12/AVDZ is used. Energies are reproduced from Hansen *et al.*[4] and Moore *et al.*[5]

The potential for the COOH torsion of TBHP is a symmetric double well potential with two identical minimum energy configurations where the OH group points toward one of the methyl groups. The barrier separating the two minima is sufficiently low ($\sim$300 cm^{-1}) to cause the torsional energy levels to appear as doublets due to tunneling splittings.[126] The present study builds on the previous model to analyze the coupled OH stretch and COOH torsion vibrations observed in the $\Delta v_{\mathrm{OH}} = 2$ region using a 1+1 model.[127] In $^{\bullet}$QOOH, the potential of the COOH torsion is an asymmetric double well with the minimum where the OH group is centered over the radical center and the second minima is $\sim$200 cm^{-1} higher in energy, corresponding to were the OH group points towards the CH_3 group.

The OH-stretching overtone spectrum of TBHP is examined experimentally in the $2v_{\mathrm{OH}}$ region under jet-cooled ($\sim$10 K) and thermal (300 K, 3 Torr) conditions. Under jet-cooled conditions, OO bond breakage of TBHP is induced by multiphoton IR excitation forming OH radical products, which are detected by LIF. Under thermal conditions, direct absorption of the OH stretch is detected. Here, we focus on the $\Delta \mathrm{v}_{\mathrm{OH}} = 2$ region and use the calculated transition frequencies and relative intensities to explain the underlying transitions that could be contributing the the breadth of the features seen in the experimental spectra. The observed $^{\bullet}$QOOH features are compared to a theoretically predicted IR absorption spectrum obtained from a 2+1 model, differing from the model used in TBHP in that it starts with a two-dimensional description of the potential in the low-frequency COOH torsion and CH_2 rotation, then adds the OH stretch.[32,34] This spectral range encompasses fundamental and overtone transitions for CH and OH stretch vibrations, along with combination bands involving either the OH stretch or the asymmetric CH stretch of the $^{\bullet}CH_2$ radical center. Finally, the spectral features of $^{\bullet}$QOOH are compared to corresponding IR transitions of the TBHP precursor.

5.2 Theory

Both the 1+1 and 2+1 models are based on an overall reaction path model that focuses on the coupling of the OH stretch and COOH torsion (1+1) or the COOH torsion and the rotation of the CH_2 group (2+1) while treating the remaining vibrations as harmonic oscillators. In the reaction path approach, the potential energy surface is calculated as either a one-dimensional function of the COOH torsion (τ) or a two-dimensional function of the COOH (τ) and the rotation of the CH_2 group (ϕ) at the B2PLYP-D3/cc-pVTZ level of theory/basis using the Gaussian16 program package.[3] In this calculation, the other internal coordinates are adjusted to minimize the electronic energies. At each point in the scan, a harmonic calculation is performed to obtain the Hessian of the potential, and the reaction-path normal mode approach of Miller, Handy, and Adams is used to obtain the harmonic zero-point energies in each of the other degrees of freedom, with the exception of the OH-stretch.[33] These zero-point energies are added to the electronic energies to generate an effective torsional (TBHP) or torsion/rotational ($^{\bullet}$QOOH) potential. As the OH-stretching frequency is an order of magnitude larger than that of either τ or ϕ, a vibrational adiabatic separation of these motions is used to evaluate the energies and wave functions.[50] In this calculation, adiabatic surfaces corresponding to the ground state ($v_{\mathrm{OH}} = 0$) and second excited state ($v_{\mathrm{OH}} = 2$) are obtained using a discrete variable representation (DVR) based on an evenly spaced grid of points on the $-\infty$ to ∞ interval to evaluate energies of the $v_{\mathrm{OH}} = 0$ and 2 levels in the OH stretch at each value of τ, or in the case of $^{\bullet}$QOOH at each value of τ and ϕ.[50] For TBHP, the wave functions and energies are evaluated in a particle-on-a-ring (POR) basis by fitting the adiabatic potential energy surfaces (PESs) and the Wilson G-matrix element for the torsion to an expansion in $\cos(k\tau)$ for $k \leq 6$, and 31 POR basis functions are used in the representation of the Hamiltonian.[8,128] In this chapter we focus on the 2+1 model, but additional information on the 1+1 model can be found in Chapter 6 and in Vogt *et al.*[34]

In the 2+1 model, we perform an adiabatic separation of the τ and ϕ from the OH stretch (r). We write the full model Hamiltonian as

$$\hat{H}_{3d} = \frac{1}{2}p_\tau G_{\tau\tau} p_\tau + \frac{1}{2}p_\phi G_{\phi\phi} p_\phi + \frac{1}{2}p_\tau G_{\tau\phi} p_\phi + \frac{1}{2}p_\phi G_{\tau\phi} p_\tau + \frac{1}{2\mu_{\mathrm{OH}}}p_r^2 + V(r_{\mathrm{OH}}, \tau, \phi) \qquad (5.1)$$

where μ_{OH} is the reduced mass of an OH bond, and $G_{\tau\tau}$, $G_{\phi\phi}$, and $G_{\tau\phi}$ are the coordinate dependent Wilson G-matrix elements.[8,128] Formally, there is kinetic coupling between r_{OH} and τ, but through the adiabatic separation it is implicitly included. Finally, $V(r_{\mathrm{OH}}, \tau, \phi)$ is the potential energy surface, evaluated at the B2PLYP-D3/cc-pVTZ level of theory/basis as implemented in Gaussian16.[3] The potential is constructed in two parts. First, we optimize the geometry every 10° for τ ranging from 0 to 360° and ϕ ranging from 0 to 180°. In performing this scan, we take advantage of the fact that $V(r_{\mathrm{OH}}, \tau, \phi) = V(r_{\mathrm{OH}}, \tau, \phi + \pi)$. Next, we evaluate the OH stretch potential for 30° increments in τ and ϕ, by displacing the optimized OH bond length by -0.2 Å to 1.0 Å in increments of 0.02 Å with all other internal coordinates constrained to their optimized values at these angles. Due to the order of magnitude difference between the frequencies of the OH stretch and two torsional modes, we approximate the wave functions by

$$\Psi = \psi_n\left(r_{\mathrm{OH}}; \tau, \phi\right) \chi_m^n(\tau, \phi) \qquad (5.2)$$

where the n index specifies the OH-stretching quantum number and m indicates the torsion/rotation quantum state. The vibrational wave functions and energies are obtained by first solving the one-dimensional Schrödinger equation in the OH stretch, at specified values of τ and ϕ, in increments of 30°.

$$\hat{H}_{1d}\psi_n(r_{\mathrm{OH}}; \tau, \phi) = \left[\frac{1}{2\mu_{\mathrm{OH}}}p_r^2 + V(r_{\mathrm{OH}}, \tau, \phi)\right]\psi_n(r_{\mathrm{OH}}; \tau, \phi) = \epsilon_n(\tau, \phi)\psi_n(r_{\mathrm{OH}}; \tau, \phi) \qquad (5.3)$$

The Schrödinger equation in Equation 5.3 was solved using one-dimensional discrete variable representations (DVR) as described by Colbert and Miller[50] with 1000 evenly-spaced grid points over the scanned range. A cubic spline was used to interpolate the OH-stretching potential. The energies obtained from these one-dimensional calculations are used to create the two-dimensional adiabatic potentials as functions of τ and ϕ. In the second part of the calculation, we use the adiabatic potentials, $\epsilon_n(\tau, \phi)$ to evaluate the two-dimensional wave functions in τ and ϕ based on:

$$\begin{aligned} \hat{H}_{2d}\chi_m^n(\tau,\phi) &= \left[\tfrac{1}{2}p_\tau G_{\tau\tau}p_\tau + \tfrac{1}{2}p_\phi G_{\phi\phi}p_\phi + \tfrac{1}{2}p_\tau G_{\tau\phi}p_\phi + \tfrac{1}{2}p_\phi G_{\tau\phi}p_\tau + \epsilon_n(\tau,\phi)\right]\chi_m^n(\tau,\chi) \\ &= E_m^n\chi_m^n(\tau,\chi) \end{aligned} \tag{5.4}$$

For this calculation the two-dimensional adiabatic potentials are interpolated to a (51, 51) grid using a cubic spline and the energies and wave functions are obtained using a two-dimensional DVR on the 0 to 2π domain.[50] The two-dimensional transition dipole moments were calculated using the dipole moments obtained from the electronic structure calculations, which have been rotated to the Eckart frame based on the $^{\bullet}$QOOH1 optimized geometry (see Figure 5.2). The intensity of a transition in km mol^{-1} is given by:[32,94]

$$f = 2.506[\text{cm D}^{-2}\ \text{km mol}^{-1}]\tilde{\nu}\left|\left\langle\chi_m^n\right|\left\langle\psi_n\right|\mu\left|\psi_n'\right\rangle\left|\chi_m'^n\right\rangle\right|^2 \tag{5.5}$$

where $\tilde{\nu}$ is the transition frequency and μ is the dipole moment.

5.3 Results & Discussion

5.3.1 Comparison of Spectral Features of TBHP and $^{\bullet}$QOOH

The vibrational overtone spectrum of TBHP in the $2v_{OH}$ region is investigated under jet-cooled conditions (∼10 K) by scanning the optical parametric oscillator from 7000 to 7220 cm^{-1} at a power of 15 mJ/pulse and a scan speed of 0.05 cm^{-1}/s, with UV LIF detection of the resultant OH radical products on the $A^2\Sigma^+ - X^2\Pi(1,0)Q_1(3)$ transition at an IR–UV time delay of 660 ns. A single unstructured feature is observed with the peak centered at 7017.8 cm^{-1} and a FWHM of 12.2 cm^{-1}.

In recent work, the $2v_{OH}$ transition of the TBHP precursor was observed at 7017.8 cm^{-1} by multi-photon IR excitation with OH LIF detection (Figure 5.3a).[32,126] This required absorption of at least three IR photons to promote TBHP above the OO dissociation limit and yield OH products.[129] The resultant IR action spectrum of TBHP obtained with pure Ar carrier gas at an IR-UV time delay of 660 ns is shown in Figure 5.3a. Figure 5.3b shows the $2v_{OH}$ feature of $^{\bullet}$QOOH1 centered at 6971.5 cm^{-1} along with the weaker $^{\bullet}$QOOH2 and/or $^{\bullet}$QOOH3 feature at 7017.5 cm^{-1} under experimental conditions optimized for $^{\bullet}$QOOH production and detection, specifically with photolysis of Cl_2 to generate Cl atoms and an IR–UV time delay of 10 ns.

The OH overtone features of TBHP and $^{\bullet}$QOOH2 and/or $^{\bullet}$QOOH3 are clearly overlapped and separated as described above. Under $^{\bullet}$QOOH optimized conditions, the contribution from the TBHP $2v_{OH}$ feature is significantly reduced (by a factor of 6), in part due to the TBHP reaction with Cl atoms and minor UV photolysis at 355 nm.[130] Most importantly, the short IR–UV time delay (10 ns) favors detection of $^{\bullet}$QOOH ($2v_{OH}$) that rapidly dissociates ($\leq$ 4 ns) to OH products,[4] while IR multi-photon excitation of TBHP slowly releases (∼660 ns) OH products.[32] The $2v_{OH}$ transitions of $^{\bullet}$QOOH1 and TBHP are clearly distinct from one another, differing in peak positions by ∼46 cm^{-1}, which agrees reasonably well with the spacing predicted by the models (∼42 cm^{-1}).

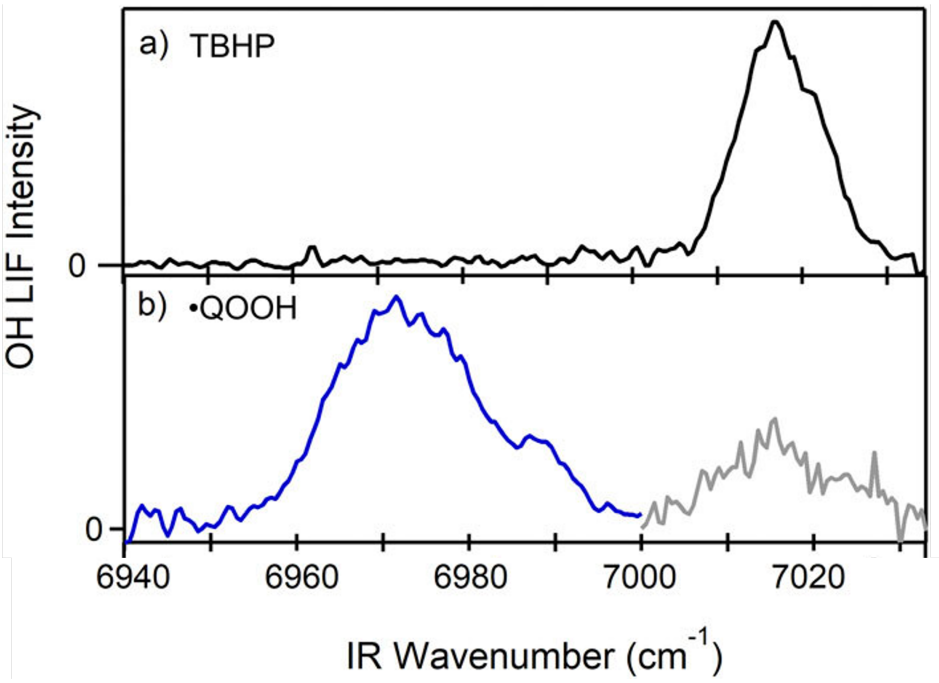

Figure 5.3: •QOOH and TBHP transitions observed and predicted in the first overtone OH stretch ($2v_{\mathrm{OH}}$) region. All experimental spectra are recorded using UV LIF detection of OH products. The LIF intensities are in arbitrary units and are only approximate in scaling between different color-coded segments. (a) IR action spectrum of TBHP recorded at an IR–UV time delay of 660 ns. (b) IR action spectrum of •QOOH obtained at an IR–UV time delay of 10 ns. The 7000 to 7035 cm^{-1} region (gray) was acquired using an alternate 355 nm photolysis ON–OFF subtraction scheme to remove the overlapping TBHP ($2v_{\mathrm{OH}}$) feature.

5.3.2 COOH Torsion (τ) in TBHP

The torsional potential about the OO bond of TBHP (τ) is a symmetric double well potential, containing two identical minimum energy configurations (gauche) [see Figure 5.4a]. In these geometries, the OH group points toward one of the methyl groups, which correspond to τ angles of about 113° and 247°. At the transition state that separates these minima, the OH group is in the COO plane (trans) with $\tau = 180°$.[126] As the trans-barrier for internal rotation of TBHP is roughly a factor of 1.5 larger than the frequency associated with the torsional motion around the OO bond [Figure 5.4a], we expect that the vibrational energies associated with the torsion will exhibit tunneling splittings. In order to accurately describe the tunneling splittings and therefore the vibrational spectrum of TBHP, we employ the 1+1 model described in detail in Vogt *et al.*[34] This model uses adiabatic separations of the high (OH-stretching) and low frequency vibrations to calculate effective torsion potential that include the effect of other vibrational modes. The calculated barrier height from this model for $v_{\mathrm{OH}} = 0$ is 335 cm^{-1}, which is in agreement with the fitted value of 275 ± 25 cm^{-1} from the earlier study of Likar *et al.*[126] Figure 5.4a shows the lower and upper tunneling doublets for both the OH-stretching vibrational ground state ($v_{\mathrm{OH}} = 0$) and the second excited state ($v_{\mathrm{OH}} = 2$). The pair of states that correspond to the ground torsional states are identified as $|0_+\rangle$ (red) and $|0_-\rangle$ (blue), abbreviated as $|0_\pm\rangle$, while the first excited torsional states are identified as $|1_+\rangle$ (green) and $|1_-\rangle$ (purple), abbreviated as $|1_\pm\rangle$. Transitions between the vibrational ground and second excited OH-stretching states are referred to as $|0_+\rangle \rightarrow |0_+\rangle$, $|0_+\rangle \rightarrow |0_-\rangle$, etc., where the first ket represents the torsion level for $v_{\mathrm{OH}} = 0$ and the second provides the torsion level for $v_{\mathrm{OH}} = 2$. Calculated values of these transitions can be found in Table 5.1. It is important to note at this point, that transitions between torsional states of the same symmetry will be a combination of A- and B-type and transitions between torsional states of different symmetry will be purely C-type.

The torsional barrier height increases with OH vibrational excitation and results in an associated increase in the torsion frequency. For $v_{\mathrm{OH}} = 2$, the barrier height is 432 cm^{-1},

Table 5.1: Calculated transition frequencies ($\tilde{\nu}$), relative intensities (RI), and transition types for the torsional transitions of TBHP in the $2v_{\mathrm{OH}}$ region using the 1+1 model.

Transition	$\tilde{\nu}$ (cm^{-1})	RI	Type
$\|0_-\rangle \rightarrow \|0_+\rangle$	7053.6	0.48	C
$\|0_-\rangle \rightarrow \|0_-\rangle$	7054.0	1.00	A/B
$\|0_+\rangle \rightarrow \|0_+\rangle$	7055.5	1.00	A/B
$\|0_+\rangle \rightarrow \|0_-\rangle$	7056.0	0.47	C
$\|0_-\rangle \rightarrow \|1_+\rangle$	7268.8	0.0001	C
$\|0_-\rangle \rightarrow \|1_-\rangle$	7285.0	0.09	A/B
$\|0_+\rangle \rightarrow \|1_+\rangle$	7270.6	0.11	A/B
$\|0_+\rangle \rightarrow \|1_-\rangle$	7286.8	0.003	C
$\|1_-\rangle \rightarrow \|1_+\rangle$	7042.2	0.29	C
$\|1_-\rangle \rightarrow \|1_-\rangle$	7058.5	0.97	A/B
$\|1_+\rangle \rightarrow \|1_+\rangle$	7083.1	1.00	A/B
$\|1_+\rangle \rightarrow \|1_-\rangle$	7099.3	0.21	C
$\|1_-\rangle \rightarrow \|2_+\rangle$	7193.8	0.03	C
$\|1_-\rangle \rightarrow \|2_-\rangle$	7280.5	0.15	A/B
$\|1_+\rangle \rightarrow \|2_+\rangle$	7234.6	0.25	A/B
$\|1_+\rangle \rightarrow \|2_-\rangle$	7321.3	0.004	C

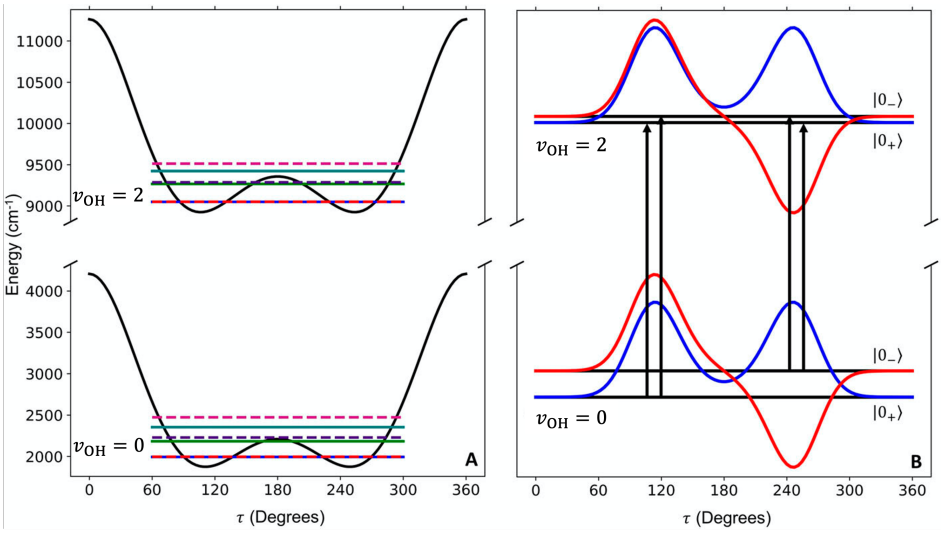

Figure 5.4: (a) Torsional potentials of TBHP for the vibrational ground ($v_{OH} = 0$) and second excited OH-stretching states ($v_{OH} = 2$). The $|0_{\pm}\rangle$ (red and blue), $|1_{\pm}\rangle$ (purple and green), and $|2_{\pm}\rangle$ (cyan and pink) tunneling doubles are shown. (b) The wave functions of the lower energy torsion doublet in $v_{OH} = 0$ and 2. The four transitions between these states are also shown.

which is 97 cm^{-1} larger than the barrier for $v_{OH} = 0$. This increase in barrier height can be attributed to the increase in the energy of the $v_{OH} = 2$ state at the *trans*-barrier compared to its value in the minimum energy configuration. This increase in barrier height leads to a steeper potential in τ, which is consistent with the increase in the torsion frequency with excitation of the OH-stretch. Additionally, $\langle r_{OH} \rangle$ increases with increasing vibrational excitation to v_{OH} leading to an increase in the effective mass of the torsion with OH-stretching excitation. Taken alone, this increase in the effective mass would result in a decrease in the torsion frequency by 5 cm^{-1}, but when both the potential energy and the kinetic energy variations are considered, the calculations show an overall increase in the torsion frequency by 30 cm^{-1} for $v_{OH} = 2$ compared to $v_{OH} = 0$.

The $|0_{\pm}\rangle$ states are calculated to have a splitting of 1.9 cm^{-1} for $v_{OH} = 0$, while the analogous pair of states for $v_{OH} = 2$ have a smaller tunneling splitting (0.42 cm^{-1}) due to the higher torsional barrier (see Table 5.1 and Figure 5.4). The pair of states that correspond

to the first excited state in the torsion ($|1_{\pm}\rangle$) lie close to the top of the barrier on the corresponding adiabatic potential, shown as green and purple energy levels in Figure 5.4(a). The lower barrier on the $v_{\mathrm{OH}} = 0$ potential leads to a larger calculated tunneling splitting of 40.9 cm^{-1} for $|1_{\pm}\rangle$ compared to a tunneling splitting of 16.2 cm^{-1} when $v_{\mathrm{OH}} = 2$. Finally, the second excited torsional states $|2_{\pm}\rangle$ (cyan and pink in Figure 5.4) are predicted to exhibit even larger tunneling splittings.

Four spectroscopic transitions are predicted between the lowest tunneling split torsional states of $v_{\mathrm{OH}} = 0$ and 2, which are shown in Figure 5.4(b) and reported in Table 5.1 along with their relative intensities and transition types. These four transitions contribute to the $2v_{\mathrm{OH}}$ vibrational overtone feature observed at 7017.8 cm^{-1} in the cold spectrum and span a range of 2.5 cm^{-1} based on the calculations, which results in overlapping rotational band contours. At room temperature, excited torsional states, specifically $|1_{\pm}\rangle$ for $v_{\mathrm{OH}} = 0$, will be significantly populated, and additional transitions (e.g., ones to the $|1_{\pm}\rangle$ states with $v_{\mathrm{OH}} = 2$) will contribute to the $2v_{\mathrm{OH}}$ vibrational overtone feature shown in the room temperature spectrum in Figure 5.3(a). At room temperature, states with $n_{\mathrm{tor}} \geq 2$ account for less than 10% of the population. Unlike the $|0_{\pm}\rangle$ states, which display a small tunneling splitting, the splitting between the $|1_{\pm}\rangle$ states are 40.9 and 16.2 cm^{-1} for the $v_{\mathrm{OH}} = 0$ and 2 levels, respectively. The four transitions associated with $n_{\mathrm{tor}} = 1$ carry intensity and span around 60 cm^{-1}. Their contribution to the $2v_{\mathrm{OH}}$ feature at room temperature will increase the breadth of the band profile compared to the corresponding feature at 10 K. The room temperature spectrum shows a second feature near 7203 cm^{-1}, which is assigned to a OH-stretch-torsion combination band with two quanta in the OH stretch and an increase in the torsional quantum number by one (i.e., $v_{\mathrm{OH}} = 2 + \Delta n_{\mathrm{tor}} = 1$). Since both the $|0_{\pm}\rangle$ and the $|1_{\pm}\rangle$ states with $v_{\mathrm{OH}} = 0$ are populated at room temperature, the observed spectral feature at $\sim$7203 cm^{-1} includes contributions from transitions originating from both sets of states. The energy differences associated with the four transitions between the $|0_{\pm}\rangle$ states for $v_{\mathrm{OH}} = 0$ and the $|1_{\pm}\rangle$ states for $v_{\mathrm{OH}} = 2$ span a 18 cm^{-1} range (Table 5.1), which is significantly broader than the $2v_{\mathrm{OH}}$ feature ($\sim$5 cm^{-1}). The spectral breadth of the combination feature

compared to the pure OH-stretching ($2v_{\mathrm{OH}}$) feature increases because the torsional states with $n_{\mathrm{tor}} = 1$ display a larger tunneling splitting than the $n_{\mathrm{tor}} = 0$ states, as described above. As a result, the four $|0_{\pm}\rangle \rightarrow |0_{\pm}\rangle$ transitions are all close in frequency, whereas the $|0_{\pm}\rangle \rightarrow |1_{\pm}\rangle$ transitions are more spread out. This effect is even larger when considering the $|0_{\pm}\rangle \rightarrow |2_{\pm}\rangle$ transitions as the second excited torsional states are split even more than the states with $n_{\mathrm{tor}} = 0$ or 1.

Under jet-cooled conditions, we anticipate that only the lowest torsional states ($|0_{\pm}\rangle$) will have significant population. As a result, only two weak transitions ($|0_{-}\rangle \rightarrow |1_{-}\rangle$ and $|0_{+}\rangle \rightarrow |1_{+}\rangle$), separated by about 15 cm^{-1}, are predicted to contribute significantly to the OH-stretch-torsion combination band (Table 5.1). The predicted intensities for each of these transitions is at least a factor of 20 weaker than the combined intensity of the four closely spaced transitions that give rise to the pure $2v_{\mathrm{OH}}$ feature. Thus, these combination bands are predicted to be too weak to be detected under jet-cooled conditions, as found experimentally. In addition, the multi-photon absorption leading to OH radical products could be less favorable at the combination band compared to the pure OH-stretching overtone region. Transitions between the $|1_{\pm}\rangle$ states for $v_{\mathrm{OH}} = 0$ and $|2_{\pm}\rangle$ states for $v_{\mathrm{OH}} = 2$ also contribute to the $\sim$7203 cm^{-1} feature in the room temperature spectrum. These four hot band transitions have transition intensities that are roughly twice as large as those for the corresponding transitions from the $|0_{\pm}\rangle$ states. Accounting for the relative thermal populations of these states, the contributions from the $|0_{\pm}\rangle \rightarrow |1_{\pm}\rangle$ and $|1_{\pm}\rangle \rightarrow |2_{\pm}\rangle$ transitions are roughly equal in the $\sim$7203 cm^{-1} feature in the room temperature spectrum. The surprisingly large intensities of these hot band transitions reflect the greater delocalization of the torsion wave functions for the $|1_{\pm}\rangle$ and $|2_{\pm}\rangle$ states compared to the $|0_{\pm}\rangle$ states.[32]

5.3.3 Simulating Experimental Features of TBHP and $^{\bullet}$QOOH

Likar *et al.* explored the breadth of the OH-stretching overtone feature of TBHP using an adiabatic separation of the OH stretch and the COOH torsion followed by a calculation of the intensities based on a Franck–Condon treatment.[126] Within this approximation, four transi-

tions predominantly contribute to the band of the OH-stretching feature. These transitions are between the lowest four torsional states ($|0_{\pm}\rangle$ and $|1_{\pm}\rangle$) of $v_{\mathrm{OH}} = 0$ and the corresponding torsional states with the same symmetry within the excited state (i.e., $|0_{+}\rangle \rightarrow |0_{+}\rangle$, $|0_{-}\rangle \rightarrow |0_{-}\rangle$, $|1_{+}\rangle \rightarrow |1_{+}\rangle$, and $|1_{-}\rangle \rightarrow |1_{-}\rangle$). However, as pointed out by Matthews *et al.*[131] for CH_3OOH, although two of the components of the torsional transition moment are symmetric about $\tau = 180°$, the third component is antisymmetric. Remember that transitions between torsional states of the same symmetry will be a combination of A- and B-type, and transitions between torsional states of different symmetry will be purely C-type. The model used in the present study includes the torsional dependence of the dipole moment function, and thus, the transitions between states of different symmetry [e.g., $|1_{+}\rangle \rightarrow |1_{-}\rangle$, Figure 5.4] carry intensity, and unlike the $|1_{+}\rangle \rightarrow |1_{+}\rangle$ and $|0_{-}\rangle \rightarrow |0_{-}\rangle$ transitions, which occur at roughly the same energy, $|1_{+}\rangle \rightarrow |1_{-}\rangle$ and $|1_{-}\rangle \rightarrow |1_{+}\rangle$ transitions are shifted from the $|1_{+}\rangle \rightarrow |1_{+}\rangle$ by the tunneling splitting. As seen in Table 5.1, the transitions between torsional states of different symmetry carry enough intensity to affect the shape of the $2v_{\mathrm{OH}}$ band. Here, we compare the rotational profiles of the $2v_{\mathrm{OH}}$ features of TBHP and $^{\bullet}$QOOH, as well as investigate the breadth of two other features of the $^{\bullet}$QOOH spectrum.

Simulations in the $2v_{\mathrm{OH}}$ region of TBHP at 10 K are composed of four overlapping contributions as shown in Figure 5.5. Each of the four transitions is composed of P-, Q-, and R-branch structure at a rotational temperature of ∼10 K, which is typical for the present jet-cooled conditions.[132,133] The resultant rotational band structure is then broadened to account for the IR laser resolution (0.9 cm^{-1}, Gaussian) in the green traces. Adding an empirical Lorentzian broadening of 6 cm^{-1} and summing the four components yields a broadened feature (gray trace) that well represents the experimental feature for the $2v_{\mathrm{OH}}$ transition of TBHP. Without Lorentzian broadening, the four components together result in a FWHM of ∼6 cm^{-1}, which is only about half of that observed in the experimental spectrum (12.2 cm^{-1}). The increased breadth of the experimental TBHP spectrum, beyond that in the simulation of the four overlapping rotational band contours at 10 K, likely arises from coupling between bright and dark states. At $v_{\mathrm{OH}} = 2$, the density of states is already quite high ($\sim 4 \times 10^{7}$

states/cm^{-1} at ∼7017 cm^{-1}), and intramolecular vibrational redistribution (IVR) will occur fast enough to result in spectral broadening.[132,133] Upon absorption of a second IR photon, a much higher density of states will be accessible by IVR, enabling further coupling to a dense manifold of dark states at ∼14 000 cm^{-1}. More generally, the coupling matrix elements are expected to increase with the increasing OH stretch quantum number, and low frequency torsional modes are known to accelerate IVR.[134] Thus, the observed Lorentzian broadening (6 cm^{-1}) of the experimental $2v_{OH}$ spectrum of jet-cooled TBHP is attributed to the states accessed by IVR in the IR multi-photon excitation process.

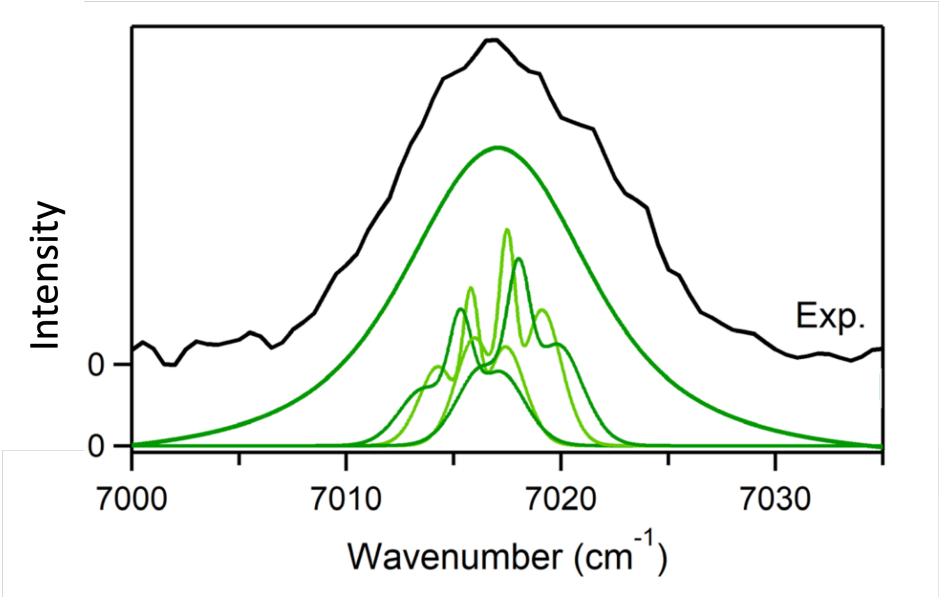

Figure 5.5: Infrared overtone spectrum of TBHP in the $2v_{OH}$ region (black trace) obtained with OH LIF detection at a fixed IR-UV time delay of 660 ns. Simulated rotational band contour (performed using PGOPHER[6] rotational structure simulation program and 1+1 Model in green) for TBHP is shown at a rotational temperature of 10 K and a laser linewidth (Gaussian) of 0.9 cm^{-1}. An empirical Lorentzian broadening (8 cm^{-1}) is added to the simulation to match the breadth of the experimental spectrum, which arises from intramolecular vibrational redistribution (IVR) in the IR multi-photon excitation process. The four underlying transitions ($|0_-\rangle \rightarrow |0_+\rangle$, $|0_-\rangle \rightarrow |0_-\rangle$, $|0_+\rangle \rightarrow |0_+\rangle$, $|0_+\rangle \rightarrow |0_-\rangle$, Table 5.1) are also simulated independently with a laser linewidth (Gaussian) of 0.9 cm^{-1}. The calculated frequencies are red-shifted by 38 cm^{-1} to facilitate comparison with experiment.

Many of the •QOOH features (v_{OH}, $v_{OH}+\delta_{OOH}$, and $2v_{OH}$) observed by IR action spectroscopy arise from a single vibrational transition and exhibit rotational band contours spanning ∼15 $cm^{-1}$with a full width at half maximum (FWHM) of ∼5.5 cm^{-1}(Table 5.2). Figure 5.6 shows an expanded view of the v_{OH} (3579.5 cm^{-1}), $v_{OH}+\delta_{OOH}$ (4880 cm^{-1}), and $2v_{OH}$ (6971.5 cm^{-1}) features along with simulations of their underlying rotational band contours. The simulations are performed with PGOPHER[6] using rotational constants and a transition type calculated using standard VPT2 (as implemented in Gaussian16[3] at the B2PLYP-D3/cc-pVTZ[135] level of theory and basis) and a rotational temperature of 10 K. The band contour is illustrated with the Gaussian laser linewidth (0.9 cm^{-1}, gray) and with addition of a Lorentzian linewidth (1.7 cm^{-1}, black) arising from homogeneous broadening. The latter is primarily attributed to rapid (∼3 ps) IVR, consistent with the density of vibrational states (∼105–108 states/cm^{-1}), although some power broadening cannot be excluded. The homogeneous broadening washes out any detail of the rotational structure or transition type. For the v_{OH} and $v_{OH}+\delta_{OOH}$ transitions, the breadth of the rotational band contour is primarily determined by the rotational temperature of 10 K. In general, the typical breadth of •QOOH rotational band contours for isolated vibrational transitions under jet-cooled conditions can be well represented by a Gaussian function with a FWHM of ∼5.5 cm^{-1}; this simplification is used in simulating the IR spectra based on standard VPT2 calculations. The rotational band contours of features involving CH vibrations of the methyl group, which are composed of multiple transitions arising from sequential absorption of two (or more) photons, are not simulated in the present study. By contrast, the experimentally observed $2v_{OH}$ feature at 6971.5 cm^{-1} is significantly broader (∼15 cm^{-1} FWHM) than other features and much broader than its simulated rotational band contour at 10 K (Figure 5). The breadth of the •QOOH $2v_{OH}$ feature could arise from multiple transitions associated with coupling between the OH stretch and low frequency torsions, as previously found for hydrogen peroxide and TBHP.[125,126] The 2+1 model was used to determine if a similar mechanism applies to •QOOH to those invoked in TBHP. However, in this case, the loss of symmetry between the •QOOH1 and •QOOH2 structures (see Figure 5.2) eliminates the tunneling splittings found

in TBHP. While there are splittings associated with the CH_2 rotation, the spacing between the associated peaks is predicted to be less than 0.1 cm^{-1} and undetectable at the resolution of the present experiments. As with TBHP, we predict coupled OH stretch-torsion states of $^{\bullet}$QOOH with a strong intensity. However, these lie ∼250 cm^{-1} higher in energy than the pure $2v_{OH}$ transition (Table 5.3), and cannot contribute to the breadth of the $2v_{OH}$ feature shown in Figure 5.6.

Table 5.2: Observed IR transitions (cm^{-1}) for $^{\bullet}$QOOH and calculated anharmonic frequencies (ν) in $cm^{-1}$and intensities (I) in km mol^{-1} for $^{\bullet}$QOOH1, $^{\bullet}$QOOH1, and $^{\bullet}$QOOH3 using standard VPT2 at the B2PLYP-D3/cc-pVTZ level of theory and basis.

	Observed	Standard VPT2					
		$^{\bullet}$QOOH1		$^{\bullet}$QOOH2		$^{\bullet}$QOOH3	
State	Frequency	ν	I	ν	I	ν	I
$2v_{OH}$	7015.5		7012	5.0	7021	5.1	
	6971.5	6984	4.8				
$2\nu_{CH_2}$	6187.0	6209	0.3	6243	0.3	6230	0.4
$2\nu_{CH_3}$	5932.0	5942	0.4	5935	0.4	5944	0.3
		5921	0.3	5921	0.3	5917	0.2
$\nu_{OH} + \delta_{OOH}$	4879.0	4880	0.6	4888	0.5	4884	0.5
v_{OH}	3597.8						
	3579.5	3580	19				
ν_{CH_2}	3025	3049	21				
ν_{CH_3}	2986	3000	20				

5.3.4 QOOH conformers

Predominately, the IR transitions captured experimentally can be contributed to the most stable conformer of $^{\bullet}$QOOH ($^{\bullet}$QOOH1) based on the remarkable agreement between the experiment and standard VPT2 calculations for their vibrational frequencies (see Table 5.2). In the v_{OH} region, however, two spectral features are observed in close proximity. The strong feature at 3579.5 $cm^{-1}$is readily assigned to the fundamental OH stretch of $^{\bullet}$QOOH1, predicted at 3580 cm^{-1} with a large intrinsic intensity (19 km mol^{-1}), while the adjacent weaker

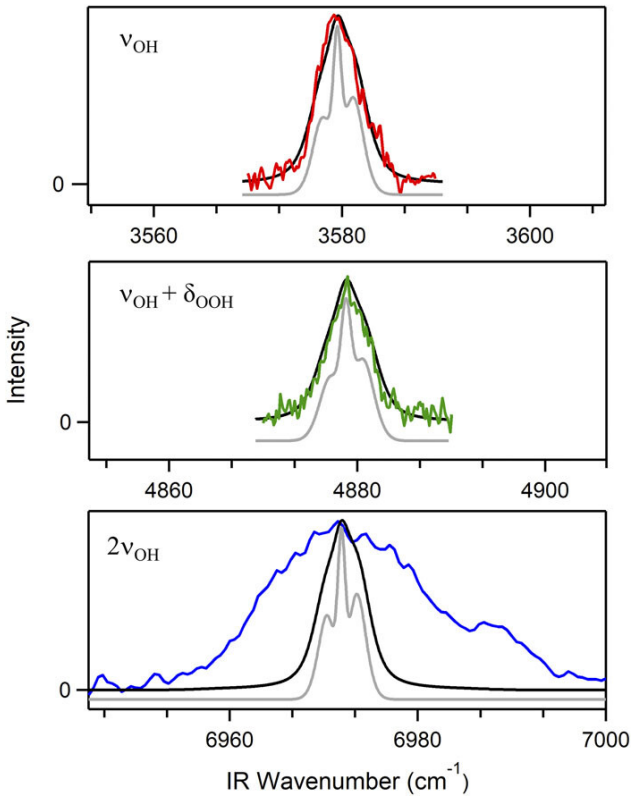

Figure 5.6: The fundamental OH stretch (v_{OH}, 3579.5 cm^{-1}; top), a combination band of the OH stretch and OOH bend (v_{OH}+δ_{OOH}, 4879.0 cm^{-1}; middle), and the first overtone OH stretch ($2v_{\mathrm{OH}}$, 6971.5 cm^{-1}; bottom) with intensities in arbitrary units. Simulated rotational band contours at $T_{rot} \sim 10K$ for $^{\bullet}$QOOH1 are overlaid with the experimental IR action spectrum. Simulations are shown at the laser linewidth (0.9 cm^{-1}, gray) and with added contribution from homogeneous broadening (1.7 cm^{-1}, black). The latter is primarily attributed to rapid (∼3 ps) intramolecular vibrational redistribution (IVR), although some power broadening cannot be excluded. Rotational constants (A: 4.62 GHz, B: 2.87 GHz, and C: 2.80 GHz) and transition type obtained from the anharmonic standard VPT2 calculation of $^{\bullet}$QOOH1 are used in the simulations.

feature at 3597.8 cm^{-1}, blue-shifted by 18 cm^{-1}, is likely due to the v_{OH} transition for one or both of the higher energy conformers.[4] Calculations using the 2+1 model support this assignment, showing a separation of 18 cm^{-1} between the v_{OH} transitions of $^{\bullet}$QOOH1 and $^{\bullet}$QOOH2 (Table 5.3). The standard VPT2 calculations also predict that the v_{OH} transitions of the $^{\bullet}$QOOH2 and $^{\bullet}$QOOH3 conformers should appear 12–17 cm^{-1} to higher energy with a slightly larger intrinsic intensity than $^{\bullet}$QOOH1. The observed signal of the v_{OH} transition for $^{\bullet}$QOOH2 (and/or $^{\bullet}$QOOH3) compared to that for $^{\bullet}$QOOH1, along with the computed intrinsic intensities for these transitions, yields an estimated abundance of 15% for these low-lying conformers of $^{\bullet}$QOOH. In the $2v_{OH}$ region, an additional weak feature is observed at 7015.5 cm^{-1}, shifted ∼44 cm^{-1} from the strong feature attributed to $^{\bullet}$QOOH1 at 6971.5 cm^{-1}. Again, the weak feature is likely due to the $2v_{OH}$ transitions of $^{\bullet}$QOOH2 and/or $^{\bullet}$QOOH3 conformers, which are predicted to appear 28–37 cm^{-1} to higher energy with a similar intrinsic intensity based on standard VPT2 calculations (see Table 5.2) This assignment is also consistent with the 2+1 model, which shows a separation of ∼45 cm^{-1} between the $2v_{OH}$ transitions of $^{\bullet}$QOOH1 and $^{\bullet}$QOOH2 (Table 5.3). The weak feature at 7015.5 cm^{-1}, shown in Figure 5.3(b), was recorded at 7017.8 cm^{-1}. No other IR signals are readily attributed to higher energy conformers.

Table 5.3: Calculated transition frequencies (cm^{-1}) and intensities (km mol^{-1}) for the of the OH stretch (OH), OH stretch with CH_2 rotation (OH + CH_2) and OH stretch with COOH torsion (OH + COOH) transitions in the fundamental OH stretch (v_{OH}) and the first OH stretch overtone ($2v_{OH}$) for $^{\bullet}$QOOH1 and $^{\bullet}$QOOH2 using the 2+1 model.

		$^{\bullet}$QOOH1		$^{\bullet}$QOOH2	
Parity	State	Frequency (cm^{-1})	Intensity (km mol^{-1})	Frequency (cm^{-1})	Intensity (km mol^{-1})
		v_{OH}			
+	OH	3598.5	21.22	3616.9	28.17
+	OH + CH_2	3715.3	0.22	3690.8	28.17
+	OH + COOH	3835.5	3.21	3817.3	1.99
-	OH	3598.5	21.21	3616.9	28.16
-	OH + CH_2	3715.7	0.22	3682.5	28.16
-	OH + COOH	3835.5	2.88	3815.7	1.89
		$2v_{OH}$			
+	OH	7020.8	4.14	7066.2	4.56
+	OH + CH_2	7142.4	0.09	7140.3	0.0004
+	OH + COOH	7263.3	0.31	7277.4	0.16
-	OH	7020.8	4.14	7066.2	4.56
-	OH + CH_2	7142.4	0.08	7132.0	0.0005
-	OH + COOH	7263.4	0.25	7271.9	0.08

5.4 Conclusions

The IR spectrum of TBHP has been recorded in the $2v_{OH}$ region under jet-cooled (10 K) and thermal (300 K, 3 Torr) conditions. A strong feature is observed at ∼7017 cm^{-1} in both experiments and assigned to the first overtone OH-stretching vibration of TBHP. Multiple transitions contribute to the ∼7017 cm^{-1} feature due to tunneling split energy levels within $v_{OH} = 0$ and 2, which arise from the coupling of OH-stretch and COOH torsional motions of TBHP. An additional weak feature is observed at ∼7203 cm^{-1} under thermal conditions and is assigned to the combined excitation of two quanta of OH-stretch and one quantum of torsion. The 1+1 model includes the essential coupling of the OH stretch and COOH torsion while incorporating the zero-point energy from the remaining vibrations at the harmonic level which qualatatively reprodcues the experimental spectrum. The $2v_{OH}$ feature at 10 K is derived from four transitions with overlapping rotational band contours. The spectral broadening observed likely arises from IVR associated with the IR multiphoton excitation process. The theoretical models also agree with the relative intensities for the $2v_{OH}$ and $2v_{OH} + \Delta n_{tor} = 1$ transitions at 300 K. Transitions from thermally populated torsional states increase the breadth of the room temperature spectrum.

Additionally, the IR action spectrum of the $^{\bullet}CH_2(CH_3)_2COOH$ radical ($^{\bullet}$QOOH) obtained using LIF detection of OH products. $^{\bullet}$QOOH features are observed across the 2950–7050 cm^{-1} spectral region and include vibrational transitions at energies both below and above the TS barrier (∼3600 cm^{-1}). Most of the IR transitions ascribed to $^{\bullet}$QOOH are distinct and/or readily separated from those of the TBHP precursor. The experimental spectra and the theoretically predicted (VPT2) IR absorption spectra are in very good agreement with observed features shifted to lower energy by ∼1–30 cm^{-1}, facilitating assignment of these features. The analysis of a 2+1 model Hamiltonian provided further insights into the nature of the transitions that are accessed experimentally. In most regions, a single feature is observed, which arises from a single vibrational transition. The breadth of most features is reproduced by rotational band contour simulations at 10 K with homogeneous

broadening of 1.7 cm^{-1} that originates from rapid IVR. The fundamental CH-stretch feature is much broader due to many overlapping strong CH-stretch transitions arising from sequential absorption of two (or more) photons, while the unexpectedly broad $2v_{OH}$ feature likely reflects coupling between the state with two quanta in the OH stretch and one or more nearby dark states. The experimental and theoretical IR fingerprint presented here for the $^{\bullet}$QOOH radical transiently formed in the oxidation of isobutane can be used to guide the detection of additional $^{\bullet}$QOOH radicals relevant to atmospheric and combustion chemistry.

We investigated the essential couplings between the OH-stretch and the low-frequency torsion of the COOH and the hindered rotation of $^{\bullet}CH_2$ (when applicable). These studies showed that the breadth of the $2v_{OH}$ transition seen in both TBHP and $^{\bullet}$QOOH experimentally, is not conclusively coming from the same source. In TBHP, the model shows that their are multiple transitions of the tunneling split states of the double well torsional potential contributing to the breadth, as well as experimental effects. In the case of $^{\bullet}$QOOH, the asymmetric double well torsional potential eliminates most of the tunnelling splitting causing most of the features in the spectrum to be attributed to just one transition.

Chapter 6

COUPLING OF TORSION AND OH-STRETCHING IN *TERT*-BUTYL HYDROPEROXIDE

Reproduced in part from [Emil Vogt, Rachel M. Huchmala, Casper V. Jensen, Mark A. Boyer, Jens Wallberg, Anne S. Hansen, Alexander Kjærsgaard, Marsha I. Lester, Anne B. McCoy, and Henrik G. Kjærgaard. Coupling of Torsion and OH-Stretching in Tert-Butyl Hydroperoxide. II. The OH-Stretching Fundamental and Overtone Spectra. *J. Chem. Phys.* **2021**, 154 (16), 164307] with the permission of AIP Publishing.

6.1 Introduction

Atmospheric oxidation of volatile organic compounds invariably leads to formation of organic peroxy radicals. Under low NO_x conditions, bimolecular reactions with HO_2 and autoxidation reactions of these peroxy radicals lead to formation of large quantities of hydroperoxides.[136,137] These organic hydroperoxides are central to the formation of highly oxygenated organic molecules which are known to contribute to particle formation and growth.[138–141] Direct atmospheric spectroscopic observations of trace species like hydroperoxides are difficult and rely on accurate laboratory reference spectra.[142,143] There have been a number of laboratory based measurements of vibrational spectra of hydroperoxides in the fundamental and overtone OH-stretching regions.[125,126,144–149] From a theoretical perspective, analysis of spectra of hydroperoxides have previously been largely based on empirical models rather than *ab initio* calculations.[126,147]

Interpretation of experimental vibrational spectra can be difficult, and both empirical and *ab initio* models are often needed to provide a coherent interpretation. Widely available approaches for solving the vibrational Schrödinger equation, such as generalized second-order

vibrational perturbation theory (GVPT2), have been tremendously successful for rigid and semi-rigid molecules of increasing dimension.[150,151] However, for floppy molecules with more than one energy minimum on the potential energy surface connected by small barriers, the local polynomial expansions of the potential energy surface used in most of these calculations are insufficient. Vibrational models specifically tailored to address the encountered difficulties are needed for these systems. Historically, empirical models with parameters either directly derived or fitted based on different spectroscopic regions have been used to explain spectroscopic features that are otherwise inaccessible. For example, the empirical model developed by Likar *et al.* for *tert*-butyl hydroperoxide (TBHP),[126] which is based on an adiabatic separation of the OH-stretch and the COOH torsion, was used to explain spectroscopic features in the OH-stretching overtone regions. With this model, Likar *et al.* were able to quantify the height of the barrier that connects the two equivalent minima on the potential surface that describes the COOH torsion in TBHP, and its variation with the OH-stretching quantum number, v_{OH}. Similar empirical models have been successfully applied to other hydroperoxides such as hydrogen peroxide, methyl hydroperoxide, and ethyl hydroperoxide.[145,147,148,152] The fact that a single empirical model can explain a range of spectroscopic features across a class of molecules, gives confidence in the validity of the underlying assumptions of the model. Nevertheless, the model ignores the contributions from the other degrees of freedom, as well as the coordinate dependence of the dipole moment function. However, for hydroperoxides, there is evidence that the dependence of the dipole moment on the torsional angle needs to be included for more quantitative spectroscopic predictions.[148]

In general, the coupling between the XH-stretching (where X=O, C, N, etc.) modes and the torsional mode leads to complicated spectra that, at room temperature, consist of multiple transitions from thermally excited torsional states. The spectral complexity does not always decrease with increasing torsional barrier, although the molecules become more rigid and a local expansion of the potential energy surface becomes more valid. For HOONO, the stretch-torsion coupling significantly complicates the OH-stretching regions, and within

each OH-stretching region multiple features of comparable intensity are observed.[153,154]

Within the adiabatic approximation, the XH-stretching regions can be explained based on the change in the torsional potential and the shape of the dipole moment function. In Chapter 5, we showed how a vibrational model built on the reaction path (RP) formalism provides a coherent interpretation of the $\Delta v_{\mathrm{OH}} = 2$ region of TBHP with results in good agreement with both jet-cooled and room temperature experimental spectra.[32] It includes one local mode (LM) OH-stretching coordinate, one torsional RP coordinate, and a harmonic treatment of the remaining 40 normal modes based on a quadratic expansion of the potential surface along the RP.

Likar *et al.* successfully applied a 2D adiabatic empirical model, which included the OH stretch and the COOH torsion, and a Franck-Condon treatment of transition intensities, to understand the dominant features in the $\Delta v_{\mathrm{OH}} = 4 - 6$ regions as well as to obtain the torsional barrier on the effective torsional potentials for $v_{\mathrm{OH}} = 0, 4, 5$ and 6.[126] The similarity of the experimental spectra and the calculated transition wavenumbers and intensities from the empirical model, showed that the coarse spectral features could be accounted for with a model based only on the OH stretch and the COOH torsion. Furthermore, the model clearly showed the importance of transitions from excited torsional states to the features observed in the different OH-stretching overtone regions.

In Figure 6.1, we present measured room temperature gas phase spectra of TBHP in the $\Delta v_{\mathrm{OH}} = 1 - 5$ regions. Within each OH-stretching region, a dominant OH-stretching feature is observed along with a weaker OH stretch torsion combination feature ∼180-250 cm^{-1} higher in wavenumbers than the maximum of the pure OH-stretching feature. The measured pure OH-stretching feature has approximately the same width for the different OH-stretching regions, however, the rotational fine structure is not observed for $\Delta v_{\mathrm{OH}} > 1$. This is due to both lower experimental resolution ($\Delta v_{\mathrm{OH}} = 4 - 5$) and the rapidly increasing density of states with increasing v_{OH}, which results in more rapid intramolecular vibrational energy redistribution (IVR).[32] The combination feature blueshifts and increases in intensity relative to that of the pure OH-stretching feature with increasing Δv_{OH}. Based on a Franck-

Condon treatment of intensities, the appearance of the combination feature suggests that the effective torsion potentials are different, and the increasing relative intensity suggests larger changes for higher v_{OH} (*vide infra*). This observation provided the basis of previous empirical models on hydroperoxides.[126,147]

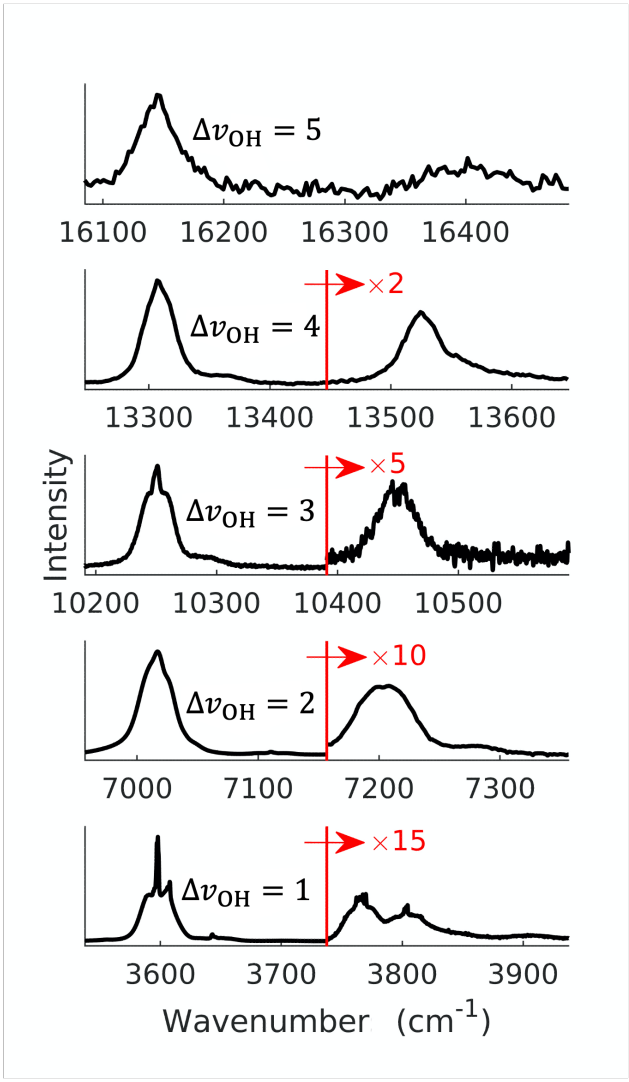

Figure 6.1: Experimental room temperature spectra of TBHP in the $\Delta v_{\mathrm{OH}} = 1 - 5$ regions. The maxima of the OH-stretching features (left features) have been aligned and the wavenumber range is equivalent for all spectra. The portions of the spectra to the right of the red lines have been multiplied by the factors given in the figure to show the structure of the OH stretch torsion combination feature.

In this chapter, we investigate the room temperature spectra for the $\Delta v_{\mathrm{OH}} = 1-5$ regions of TBHP (shown in Figure 6.1 and use theoretical models to highlight features arising from a breakdown of a Franck-Condon treatment. We find that inclusion of the dipole moment function is important to describe the relative intensity of the two major features observed within the OH-stretching regions for $\Delta v_{\mathrm{OH}} \leq 3$, and show how the OH-stretching regions of TBHP are complicated by multiple transitions at room temperature.

6.2 Theory

At the heart of the vibrational models used in this study is the adiabatic separation of the COOH torsional mode from the other vibrational modes. We write the Hamiltonian for the OH stretch and torsion as

$$\hat{H}_{\mathrm{tor,OH}}\Psi(r,\tau) = \left[\frac{1}{2}p_\tau G_{\tau\tau}(r,\tau)p_\tau + \frac{p_r^2}{2\mu_{\mathrm{OH}}} + V(r,\tau)\right]\Psi(r,\tau) \tag{6.1}$$

where r is the OH bond length, τ is the COOH torsional angle, $p_r = \frac{\hbar}{i}\frac{\partial}{\partial r}$, $p_\tau = \frac{\hbar}{i}\frac{\partial}{\partial \tau}$, μ_{OH} is the reduced mass for an OH group, and $G_{\tau\tau}(r,\tau)$ is the coordinate-dependent Wilson G-matrix element for the torsion,[8] and $V(r,\tau)$ is the potential energy surface. The order of magnitude difference between the OH-stretching and COOH torsion frequencies motivates the use of an adiabatic separation of these degrees of freedom, i.e., we write the wave functions as

$$\Psi(r,\tau) = \phi_{v_{\mathrm{OH}}}(r;\tau)\chi_{n_{\mathrm{tor}}}^{(v_{\mathrm{OH}})}(\tau) \tag{6.2}$$

where the upper index on the torsional wave function specifies its dependence on the OH-stretching quantum number, v_{OH}. The number of quanta in the torsion is represented by n_{tor}. This product form is denoted by $|v_{\mathrm{OH}}\rangle|n_{\mathrm{tor}}\rangle$, while the $(r;\tau)$ notation indicates a parametric dependence on τ. The OH-stretching wave functions and energy levels for different torsional

angles are obtained by solving

$$\begin{aligned}\hat{H}_{\mathrm{OH}}\phi_{v_{\mathrm{OH}}}(r;\tau) = & \left[\frac{p_r^2}{2\mu_{\mathrm{OH}}} + V(r,\tau)\right]\phi_{v_{\mathrm{OH}}}(r;\tau) \\ = & \; V^{\mathrm{eff}}_{v_{\mathrm{OH}}}(\tau)\phi_{v_{\mathrm{OH}}}(r;\tau)\end{aligned} \tag{6.3}$$

where $V^{\mathrm{eff}}_{v_{\mathrm{OH}}}(\tau)$ contains several contributions. The largest contribution is $E_{v_{\mathrm{OH}}}(\tau)$, which is the vibrational energy in the OH stretch for the $|\mathrm{v_{OH}}\rangle$ state (referenced to $V(0,\tau)$) that shows a weak, but significant, dependence on τ. The leading contribution to the torsion dependence of $V^{\mathrm{eff}}_{v_{\mathrm{OH}}}(\tau)$ comes from τ-dependence of the electronic energy, $V(0,\tau)$. Inclusion of only $E_{v_{\mathrm{OH}}}(\tau)$ and $V(0,\tau)$ in the definition of $V^{\mathrm{eff}}_{v_{\mathrm{OH}}}(\tau)$ leads to the approach that will be referred to as the 2D model in the discussion that follows. The reaction path (RP) model used in this study includes the harmonic zero-point energies for the other degrees of freedom in $V^{\mathrm{eff}}_{v_{\mathrm{OH}}}(\tau)$. The τ-dependent effective torsional potentials, $V^{\mathrm{eff}}_{v_{\mathrm{OH}}}(\tau)$, provide a set of adiabatic potential curves, one for each of the OH-stretching vibrational levels. The torsional energy levels and wave functions are obtained by solving

$$\begin{aligned}&\langle v_{\mathrm{OH}}|\hat{H}_{\mathrm{tor,OH}}|v_{\mathrm{OH}}\rangle|n_{\mathrm{tor}}\rangle \\ &= \left[\frac{1}{2}p_\tau\langle v_{\mathrm{OH}}|G_{\tau\tau}(r,\tau)|v_{\mathrm{OH}}\rangle p_\tau + V^{\mathrm{eff}}_{v_{\mathrm{OH}}}(\tau)\right]|n_{\mathrm{tor}}\rangle \\ &= E_{v_{\mathrm{OH}},\mathrm{n_{tor}}}|n_{\mathrm{tor}}\rangle\end{aligned} \tag{6.4}$$

where $E_{v_{\mathrm{OH}},n_{\mathrm{tor}}}$ is the energy of the torsional state on a given effective potential, including the energy of the associated OH-stretching state.

All electronic structure calculations for the 2D and RP models were performed at the B2PLYP-D3/cc-pVTZ level of theory/basis as implemented in Gaussian16.[3] In the RP model, cuts through the potential and dipole surfaces were evaluated as functions of the COOH torsion angle, where the other 41 internal coordinates were relaxed to minimize the electronic energy. The coordinates and energy were collected at each point in the scan, and a harmonic calculation was performed to obtain the gradient and Hessian at each geometry. In

addition, one-dimensional OH-stretching cuts in the potential around each of these geometries were evaluated. For these cuts, the remaining 41 internal coordinates were constrained to the values obtained in the original torsion scan.

The remaining 41 vibrations were accounted for by a RP analysis as described by Miller, Handy, and Adams.[33] This approach yields $3N$-7 normal modes and corresponding frequencies. Within this treatment, the excluded vibrational mode is defined by the normalized gradient vector in mass-weighted coordinates and describes the reaction coordinate at that geometry.[33] It should be noted that the vibration with the largest associated frequency is the OH stretch, and this mode is removed from the remainder of the RP analysis. After removing the COOH torsion and OH stretch, the remaining 40 harmonic frequencies were summed and divided by two to obtain the harmonic zero-point energy of these vibrations ($V_{\mathrm{ZPVE}}(\tau)$). This zero-point vibrational energy was added to the electronic energy ($V(0,\tau)$) leading to

$$V^{\mathrm{eff}}_{v_{\mathrm{OH}}}(\tau) = E_{v_{\mathrm{OH}}}(\tau) + V(0,\tau) + V_{\mathrm{ZPVE}}(\tau) \tag{6.5}$$

For each torsional angle, OH-stretching potentials were obtained by displacing the OH bond length from the equilibrium bond length ($r_e(\tau)$) by -0.2 to 1.0 Å, in increments of 0.02 Å, at the given value of τ. The OH vibrational energies and wave functions were evaluated using one-dimensional discrete variable representations (DVR) as described by Colbert and Miller[50] to solve Equation 6.3. A total of 2000 DVR points within the range of -0.35 to 1.15 Å were used, and a cubic spline was used to obtain the values of $V(r,\tau)$ at the desired geometries. The torsional wave functions were obtained by solving Equation 6.4 in a particle on a ring (POR) basis, where $G_{\tau\tau}(r,\tau)$ is the Wilson G-matrix element for the COOH torsion.[8] To facilitate this calculation, $V^{\mathrm{eff}}_{v_{\mathrm{OH}}}(\tau)$ and $\langle v_{\mathrm{OH}}|G_{\tau\tau}(r,\tau)|v_{\mathrm{OH}}\rangle$ were fit to expansions in $\cos(k\tau)$ with $k \leq 6$.

The transition dipole moments were calculated by first embedding the raw dipole moments in an Eckart frame with the $\tau = 180°$ geometry as the reference structure.[155,156] In this study, the $\tau = 180°$ geometry was chosen to capture the symmetry of the double-well po-

tential along the torsion coordinate.[157,158] The intensity (oscillator strength) of a transition ($|v_{\mathrm{OH}}\rangle|n_{\mathrm{tor}}\rangle \rightarrow |v'_{\mathrm{OH}}\rangle|n'_{\mathrm{tor}}\rangle$) is given by[94]

$$f = 4.702 \cdot 10^{-7}[\mathrm{cm} \cdot \mathrm{D}^{-2}]\tilde{\nu}_{v_{\mathrm{OH}},n_{\mathrm{tor}}\rightarrow v'_{\mathrm{OH}},n'_{\mathrm{tor}}} \left|\langle n_{\mathrm{tor}}|\vec{M}_{v_{\mathrm{OH}}\rightarrow v'_{\mathrm{OH}}}(\tau)|n'_{\mathrm{tor}}\rangle\right|^2 \tag{6.6}$$

where

$$\vec{M}_{v_{\mathrm{OH}}\rightarrow v'_{\mathrm{OH}}}(\tau) = \langle v_{\mathrm{OH}}|\vec{\mu}(r,\tau)|v'_{\mathrm{OH}}\rangle \tag{6.7}$$

describes the transition dipole moment as a function of τ, $\vec{\mu}(r,\tau)$ is the dipole moment function, and $\tilde{\nu}_{v_{\mathrm{OH}},n_{\mathrm{tor}}\rightarrow v'_{\mathrm{OH}},n'_{\mathrm{tor}}}$ is the transition wavenumber. Within a Franck-Condon treatment, the components of $\vec{M}_{v_{\mathrm{OH}}\rightarrow v'_{\mathrm{OH}}}(\tau_e)$ depend only on the OH-stretching wave functions associated with the transition, and the intensity is given by

$$f_{\mathrm{FC}} = 4.702 \cdot 10^{-7}[\mathrm{cm} \cdot \mathrm{D}^{-2}]\tilde{\nu}_{v_{\mathrm{OH}},n_{\mathrm{tor}}\rightarrow v'_{\mathrm{OH}},n'_{\mathrm{tor}}} \left|\vec{M}_{v_{\mathrm{OH}}\rightarrow v'_{\mathrm{OH}}}(\tau_e)\langle n_{\mathrm{tor}}|n'_{\mathrm{tor}}\rangle\right|^2 \tag{6.8}$$

6.3 Results & Discussion

For hydroperoxides, the torsional barrier connecting the minima on the potential energy surface, with torsion around the OO bond (C-O-O-H dihedral), is comparable to the torsional frequency and the thermal energy at room temperature.[126,145,147,148,152] As a result, multiple torsional states will be populated and the associated wave functions will be delocalized among these minima. The normal mode vibrational models that are implemented in quantum chemistry programs, are in general not expected to give an accurate representation of such delocalized vibrations. In Figure 6.2, we present a torsion potential for TBHP with labelled energy levels. The TBHP torsion potential is a symmetric double-well potential with a barrier at $\tau = 180°$ of around 300 cm^{-1}, connecting two equivalent minima at $\tau = 113°$ and 247°. The $\tau = 180°$ geometry corresponds to the OH group pointing straight down in between the two CH_3 groups. The tunneling split torsional states are either symmetric (+) or asymmetric (-) around $\tau = 180°$, and members of the pairs of torsional states (e.g. $|0_+\rangle$ and $|0_-\rangle$) have different energies. The tunneling splitting becomes larger with increasing

excitation of the torsion, with the tunneling splitting of the torsional ground state pair being only a few cm^{-1}, while the pairs of torsional states above the barrier are significantly split. Previously, the accuracy of the adiabatic approximation with respect to the tunneling splitting associated with the torsion has been investigated for the simplest hydroperoxide, HOOH, by comparing results obtained with a full-dimensional non-adiabatic model and an adiabatic model, in which the torsion was separated from all other vibrational modes.[159] In this case, good agreement between tunneling splittings for the fundamental states of the six different modes were found.

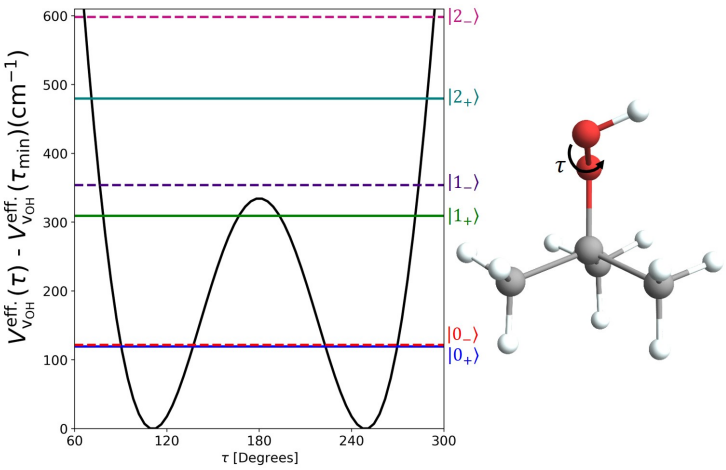

Figure 6.2: Effective potential as a function of the COOH torsion angle (τ) and energy levels for the v_{OH}=0 state of TBHP.

Within this adiabatic model, the simplest approach to obtain the intensities of OH stretch torsion transitions is to invoke an approximation that is analogous to the Franck-Condon approximation used to describe electronic transitions (Equation 6.8). Within this treatment, the relative intensities of various transitions with the same value of Δv_{OH} are proportional to $|\langle n_{tor}|n'_{tor}\rangle|^2$. While the torsion levels that are based on the same effective potential are orthogonal, this need not be the case for states with the same symmetry that are evaluated from different $V^{eff}_{v_{OH}}(\tau)$. The Franck-Condon approximation anticipates multiple torsion

transitions for a given Δv_{OH}, and the OH stretching feature will be comprised of several OH stretch torsion transitions. In particular, a combination feature (with the same quantum of excitation in the OH stretch and one additional quantum of excitation in the COOH torsion) should appear at slightly higher wavenumbers than the pure OH stretching feature, depending on the frequency of the torsional mode ($\sim$200 cm^{-1} for TBHP). The relative intensity of this combination feature and the OH stretching feature will depend on the change in the effective torsional potentials with v_{OH}. Combination bands with additional quanta in the torsional mode are also possible, but are expected to decrease in intensity with increasing torsional excitation.

6.3.1 The 2D Model

To begin this analysis, we calculated the OH stretching and torsional transitions with a 2D adiabatic Franck-Condon model that considers only the OH stretch and the COOH torsion. In Table 6.1, we present calculated and observed transition wavenumbers and relative intensities (combination feature compared to OH stretching feature) for $\Delta v_{\mathrm{OH}} = 1 - 5$, evaluated at the B2PLYP/cc-pVTZ level of electronic structure theory/basis. As seen from Table 6.1, the OH stretching transition wavenumbers calculated from the B2PLYP/cc-pVTZ surface is larger than the corresponding experimental transition wavenumbers. The smallest difference between the OH stretching transition wavenumbers is seen for $\Delta v_{\mathrm{OH}} = 1$ and the difference increases with increasing Δv_{OH}. The relative intensities, which are calculated using the Franck-Condon approach described by Equation 6.8 are denoted as $\mathrm{RI_{FC}}$. This approach predicts increasing relative intensities of the combination features with increasing Δv_{OH}, in agreement with the experimental spectra in Figure 6.1 and the results of the 2D empirical model used by Likar *et al.*[126] However, the relative intensity of the stretch-torsion combination feature is underestimated with the largest deviation of an order of magnitude found for the $\Delta v_{\mathrm{OH}} = 1$ transitions.

Table 6.1: Experimental and calculated OH stretching ($|0\rangle|0_+\rangle \rightarrow |v_{\mathrm{OH}}\rangle|0_+\rangle$) transition wavenumbers ($\tilde{\nu}$ in cm^{-1}) and relative intensities (RI in %) of the combination feature, compared to the OH stretching feature. These are evaluated with the 2D model within the Franck-Condon approximation ($\mathrm{RI_{FC}}$) and using the full dipole moment surface ($\mathrm{RI_{DMS}}$).Calculated values are denoted by (DFT) and are evaluated at the B2PLYP/cc-PVTZ level of theory/basis.

Δv_{OH}	$\tilde{\nu}_{\mathrm{OH}}$ (DFT)	$\tilde{\nu}_{\mathrm{OH}}$ (Expt.)[a]	$\mathrm{RI_{FC}}$ (DFT)[b]	$\mathrm{RI_{DMS}}$ (DFT)[b]	RI (Expt.)[a]
1	3615	3597	0.84	13.3	11.0±2.8
2	7056	7017[d]	4.05	9.96	13.3±1.2[d]
3	10323	10246	10.8	15.6	16.8±1.3
4	13421	13307[d]	21.2	24.3	47.4±1.8[d]
5	16356	16145[d]	33.5	34.9	-

[a] From this study (Figure 6.1). The experimental transition wavenumbers are the maximum of the OH stretching features and RI is the ratio of the integrated intensities.

[b] The ratio is calculated from summations over all transitions that contribute to the two features at $T = 300$ K.

[c] The $\Delta v_{\mathrm{OH}} = 2$ feature has also been observed under jet-cooled conditions with a maximum at 7017.8 cm^{-1}.[32]

[d] The $\Delta v_{\mathrm{OH}} = 4$ and $\Delta v_{\mathrm{OH}} = 5$ features have been observed at room temperature at 13300 and 16155 cm^{-1}, respectively.[126,146]

[d] Transitions related to the CH-groups in both TBHP and decane likely cause an increase the relative intensity due to absorption near the combination feature.

To understand the origins of the underestimation of the relative intensities at low Δv_{OH} based on the Franck-Condon treatment (Equation 6.8), we next consider how the calculated relative intensities change when the full dipole surface is used in the calculations (Equation 6.6). As can be seen from the $\mathrm{RI_{DMS}}$ values reported in Table 6.1, the agreement between experiment and calculation is significantly improved compared with the $\mathrm{RI_{FC}}$ values. Interestingly, while the use of the full transition dipole moment surface in the calculation of the intensities greatly increases the ratio of the intensities of the transitions of the combination feature to the OH stretching feature for the $\Delta v_{\mathrm{OH}} = 1$ region, the relative intensity for the $\Delta v_{\mathrm{OH}} = 5$ region displays only a modest change. The questions naturally arise as to why the relative intensity for $\Delta v_{\mathrm{OH}} = 1$ is most sensitive to the shape of the transition dipole surface and why this sensitivity decreases with OH stretching excitation. To explore this, we focus on the transitions between the states with $v_{\mathrm{OH}} = 0$ and $n_{\mathrm{tor}} = 0_{\pm}$ and the higher energy OH stretching states with either $n_{\mathrm{tor}} = 0_{\pm}$ or $1_{\pm}$, where the $\pm$ on the torsional states corresponds to either the symmetric (+) or asymmetric (-) component of the tunneling split pair. These are the dominant transitions in the OH stretching or combination feature, respectively. While the intensities of individual transitions differ, the sum of intensities of the transitions to the $0_{\pm}$ levels (OH stretching feature) differ by less than 7% when calculated with or without the Franck-Condon approximation. The total intensity of the transitions to the $1_{\pm}$ levels (combination feature) show greater variation. The intensities of transitions that do not change the value of n_{tor} depend primarily on the overlap of the torsional wave functions for the two v_{OH} states, with the magnitude of the intensity determined by $|\langle 0|\vec{\mu}(r,\tau_e)|v_{\mathrm{OH}}\rangle|^2$ (see Equation 6.8). The transitions that change n_{tor} by one reflect both the overlaps, which are captured in the Franck-Condon treatment, and the slope of the transition dipole moment at τ_e that arise from the next term in the expansion of $\langle n_{\mathrm{tor}}|\langle 0|\vec{\mu}(r,\tau)|v_{\mathrm{OH}}\rangle|n'_{\mathrm{tor}}\rangle$ in Equation 6.6.

In Figure 6.3, we report components of the torsion-dependent transition dipole moments for the $\Delta v_{\mathrm{OH}} = 1$ and $\Delta v_{\mathrm{OH}} = 5$ transitions for the B2PLYP/cc-pVTZ method, which has been evaluated at more torsional angles. Based on the symmetry of the components of the

transition dipole moment, transitions between states of the same symmetry will be A/B-type, whereas transitions between states of different symmetry will be C-type. The relative contribution of the Franck-Condon term and the next term in the expansion of the transition dipole moment depends on the ratio of the slope of the transition dipole moment to its value. This ratio near τ_e (dashed vertical line) is larger for the $\Delta v_{\mathrm{OH}} = 1$ than $\Delta v_{\mathrm{OH}} = 5$ transition for the A-component, which dominates the intensity of the combination feature.

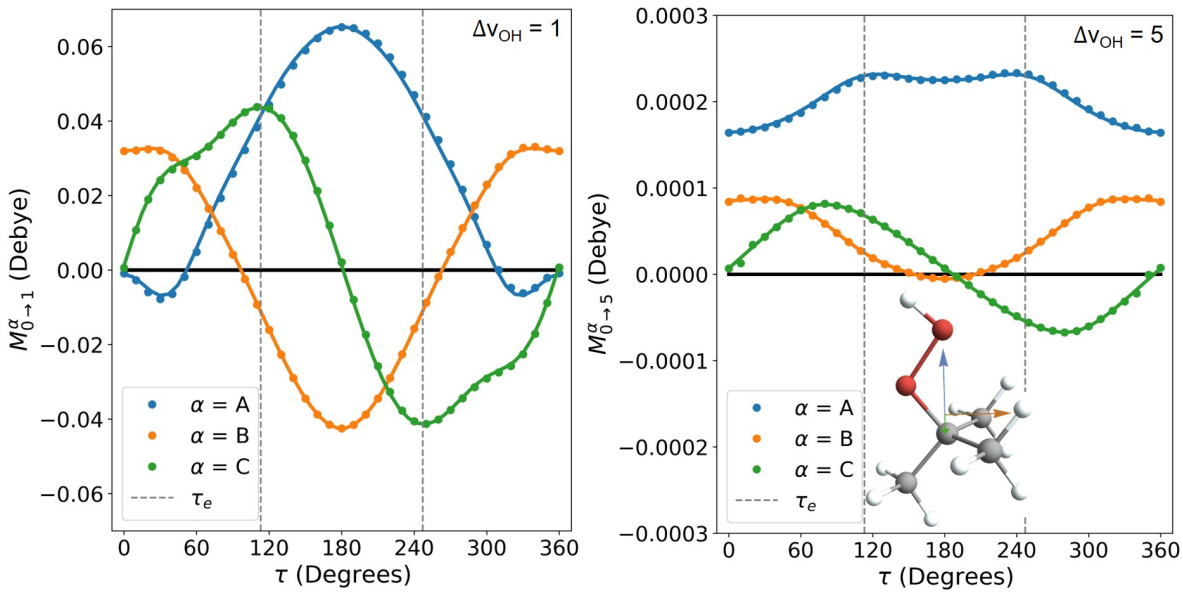

Figure 6.3: Components of the OH stretching transition dipole moment, $\vec{M}_{v_{\mathrm{OH}} \to v'_{\mathrm{OH}}}(\tau)$ in Equation 6.7 are plotted as functions of the torsional angle for $\Delta v_{\mathrm{OH}} = 1$ (left) and 5 (right). The A- and B-components of the transition dipole moment are symmetric around $\tau = 180°$, whereas the C-component is antisymmetric. The inset in the right panel shows the principal axis system. As can be seen, the OO bond is rotated by less than 30° off of the A-axis (blue axis)

6.3.2 The Reaction Path and Local Mode Models

While the above discussion explains the deviations in intensities, there are also differences between the measured and calculated vibrational frequencies. This reflects the omission of 40 of the vibrational modes by the 2D treatment and/or deficiencies in the electronic structure

approaches. It is not obvious which of the other vibrational modes to include to improve the 2D model. Intuitively, modes involving the atoms that comprise the OH bond likely affects the OH stretch. For alcohols (ROH), the inclusion of just the CO stretch and the COH bend led to OH stretching transition wavenumbers and intensities in excellent agreement with experiments for $\Delta v_{\mathrm{OH}} = 1 - 5$.[160] The RP results can be used to address the question of which modes perturbs the OH stretch and the COOH torsion. In Figure 6.4, we show the changes in the harmonic zero point vibrational energies (ΔZPVE) for selected local modes as functions of the OH bond length (left panel) and torsion angle (right panel), over the ranges sampled by the wave functions for the states of interest.

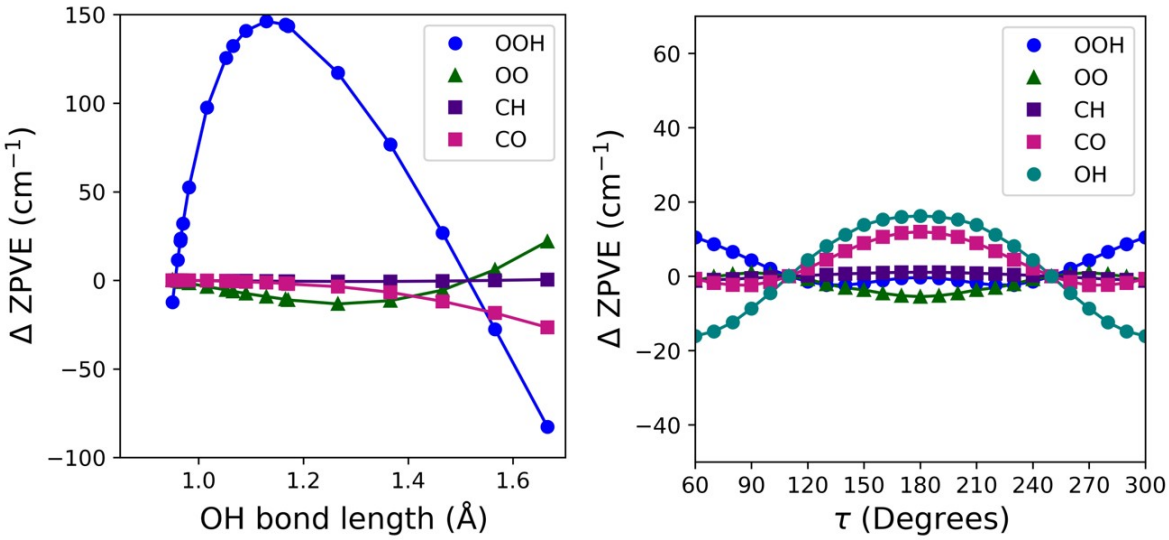

Figure 6.4: Variation of B2PLYP/cc-pVTZ local mode harmonic frequencies plotted as functions of the OH stretching bond length (left) and torsional angle (right).

From the left panel of Figure 6.4, it is seen that the frequency of the OOH bend changes significantly as the OH bond length is extended. A smaller but still noticeable change is also seen for the OO stretch, with the CO and CH stretches being practically unaffected. As can be seen from the right panel of Figure 6.4, the frequency of the OH stretch is most sensitive to the value of τ. When we consider $V_{\mathrm{ZPVE}}(\tau)$ in Equation 6.5 over the range plotted in Figure

6.4, we find that $|V_{\mathrm{ZPVE}}| \leq 7.5$ cm^{-1}. Based on this $V_{\mathrm{ZPVE}}(\tau)$ provides a small correction to the shape of the effective torsion potentials and the results for the RP model should not deviate significantly from those obtained with the 2D model. Due to this, we present a comparison of the RP Model to a Local Mode (LM) Model. The LM Model includes a total of four vibrational modes: the COOH torsion, the OH stretch, the OO stretch, and the OOH bend. The latter three modes were defined with internal curvilinear coordinates and with a kinetic energy operator corresponding to the three-dimensional contribution to the exact kinetic energy operator and pairwise potential energy coupling.[8,160,161] The single points and optimizations used in the LM calculations were all performed with CCSD(T)-F12a/cc-pVDZ-F12 with the recommended CCSD(T)-F12 correlation factor of $\beta = 0.9$ using the Molpro 2012.1 program.[26,162,163] Additional details of the LM model can be found in Vogt *et. al.*[34]

In Table 6.2, we present barrier heights, transition wavenumbers, and relative intensities calculated using the RP and LM models with the full transition dipole moment included in the evaluation of the intensities (Equation 6.6). As expected, the transition wavenumbers and relative intensities obtained from the RP treatment are nearly identical to those obtained from the 2D model. Compared with the 2D model, OH stretching transition wavenumbers calculated with the LM model are significantly improved by including the effect of the OO stretch and OOH bend on the OH stretching energies. It is clear from the left panel in Figure 6.4 that the OH stretch is affected mostly by the OOH bending mode, and to a lesser degree by the OO stretch. Apart from $\Delta v_{\mathrm{OH}} = 5$, the calculated wavenumbers are within 20 cm^{-1} of the corresponding experimental values. The larger discrepancy in this region is not surprising as the states that are accessed by the $\Delta v_{\mathrm{OH}} = 5$ transitions have energies that likely exceed the energy needed for direct OO bond fission.[126,146,164–169] The relative intensity of the combination feature compared to the OH stretching feature is in good agreement between the RP and LM model, and with the 2D model with inclusion of the full dipole moment surface.

Table 6.2: Calculated torsional barrier heights (V_τ in cm^{-1}), calculated and experimental OH stretching ($|0\rangle|0_+\rangle \rightarrow |v_{\mathrm{OH}}\rangle|0_+\rangle$) transition wavenumbers ($\tilde{\nu}$ in cm^{-1}) and relative intensities (RI in %) of the combination feature compared to the OH stretching feature. The calculated values are presented for both the RP and LM model.

Δv_{OH}	V_τ (RP)[a]	V_τ (LM)[a]	$\tilde{\nu}_{\mathrm{OH}}$ (RP)	$\tilde{\nu}_{\mathrm{OH}}$ (LM)	$\tilde{\nu}_{\mathrm{OH}}$ (Expt.)[b]	$\mathrm{RI}_{\mathrm{DMS}}$ (RP)[c]	$\mathrm{RI}_{\mathrm{DMS}}$ (LM)[c]	RI (Expt.)[b]
1	377	323	3615	3597	3597	13.7	12.9	11.0±2.8
2	432	370	7055	7021	7017[d]	9.92	10.6	13.3±1.2[f]
3	505	430	10322	10261	10246	15.5	17.0	16.8±1.3
4	595	505	13419	13326	13307[e]	24.0	28.3	47.4±1.8[f]
5	704	600	16354	16208	16145[e]	34.3	39.5	-

[a] The ground state barrier calculated with the LM and RP model is 286 and 335 cm^{-1}, respectively.

[b] From this study (Figure 6.1). The experimental transition wavenumbers are the maxima of the OH stretching features and RI is the ratio of the integrated intensities.

[c] The ratio is calculated from summations over all transitions that contribute to the two features at $T = 300$ K.

[d] The $\Delta v_{\mathrm{OH}} = 2$ feature has also been observed under jet-cooled conditions with a maximum at 7017.8 cm^{-1}.[32]

[e] The $\Delta v_{\mathrm{OH}} = 4$ and $\Delta v_{\mathrm{OH}} = 5$ features have been observed at room temperature at 13300 and 16155 cm^{-1}, respectively.[126,146]

[f] Transitions related to the CH-groups in both TBHP and decane likely cause an increase the relative intensity due to absorption near the combination feature.

6.3.3 Modelled Spectra

The results of the RP model are in good qualitative agreement with experimental findings as seen in Figure 6.5. The simulated spectra were obtained using PGOPHER and Boltzmann weighted torsional states.[6] Albeit shifted, the features of the spectra are comparable in intensity and structure.

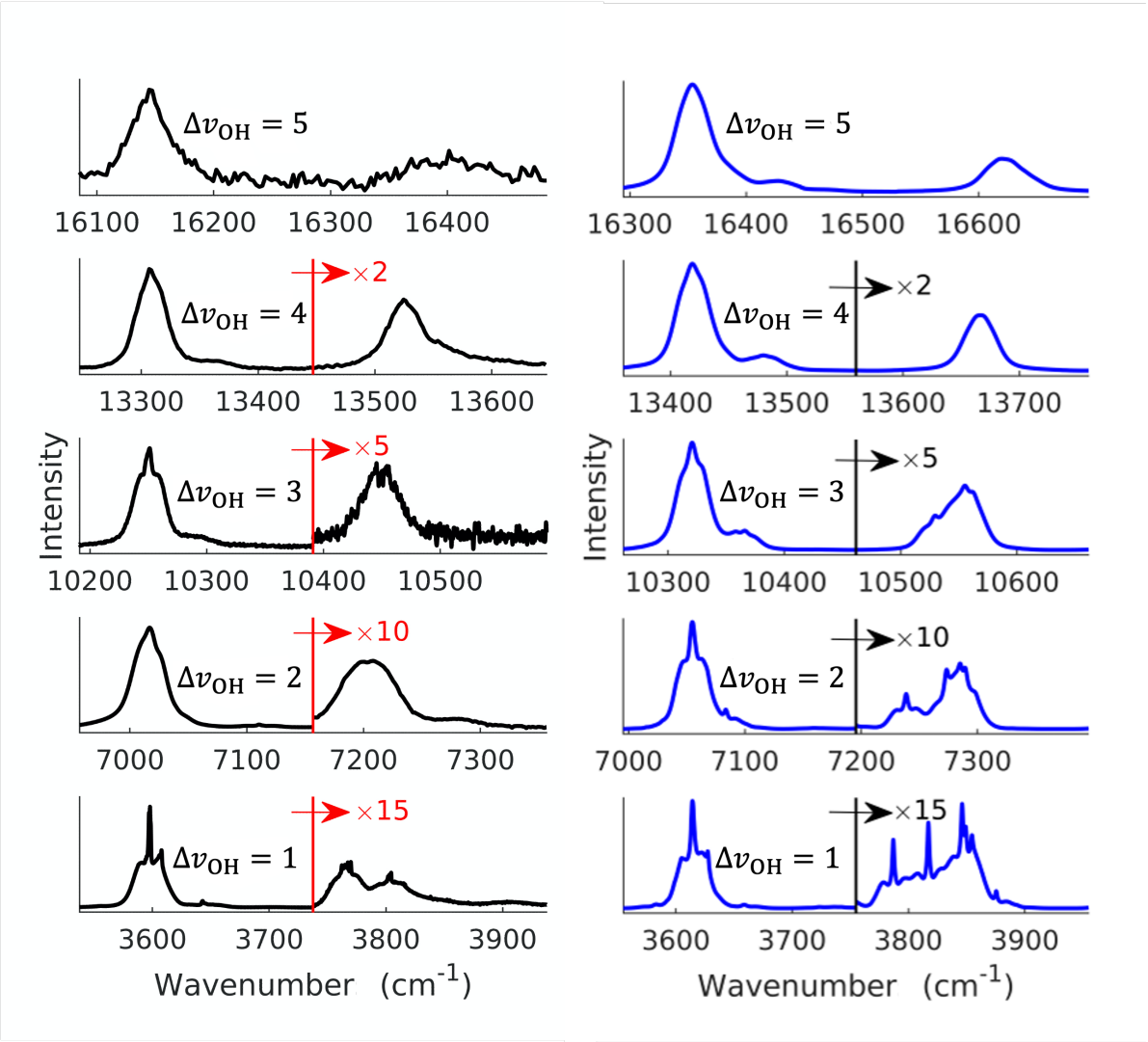

Figure 6.5: Left: Experimental room temperature ($T = 300$ K) spectra (same as shown in Figure 6.1 Right: Calculated room temperature ($T = 300$ K) spectra of the $\Delta v_{\mathrm{OH}} = 1 - 5$ regions of TBHP based on the parameters obtained from the RP model. In both, the maxima of the OH stretching features (left features) have been aligned and the wavenumber range is equivalent for all spectra. The portions of the spectra to the right of the red (left) and black (right) lines have been multiplied by the factors given in the figure to show the structure of the OH stretch torsion combination feature.

6.4 Conclusions

We have presented room temperature vibrational spectra of gas phase *tert*-butyl hydroperoxide (TBHP) in the $\Delta v_{\mathrm{OH}} = 1 - 5$ regions. The $\Delta v_{\mathrm{OH}} = 1 - 3$ regions were obtained with Fourier transform infrared spectroscopy, and the $\Delta v_{\mathrm{OH}} = 4 - 5$ regions with cavity ring-down spectroscopy. The features observed in the OH-stretching regions originate from transitions involving the OH stretch and the COOH torsion. Based on the results of a reaction path model, we found that the COOH torsion is most strongly affected by the OH-stretch, which in turn is affected by the OOH-bend and to a lesser extent by the OO-stretch. These findings validate previous empirical models used to explain spectral features in the OH-stretching region of TBHP, and form the basis for the choice of modes used in the LM model.

In each OH-stretching region, we observe two distinct features: the OH-stretching feature, and a combination feature with the OH stretch and one additional quantum of excitation in the COOH torsion. The double-well nature of the COOH torsion potential leads to tunneling splitting of the energy levels, and at room temperature several vibrational transitions contribute to each feature. Analysis of the calculated spectra illustrate the importance of the torsion dependence of the transition dipole moments in capturing the intensities of the OH stretch torsion combination transitions, especially for $\Delta v_{\mathrm{OH}} \leq 3$.

Based on the vibrational models, we predicted that the double-well nature of the COOH torsion potential should lead to a splitting of the central Q-branches for each OH-stretching feature. In the $\Delta v_{\mathrm{OH}} = 1$ region, we observe a splitting of the strongest Q-branches for the OH-stretching feature. The observed splitting of the Q-branches is an unambiguous spectroscopic evidence for the double-well nature of the COOH torsion and its strong coupling with the OH-stretch.

Chapter 7

SUMMARY AND FUTURE WORK

The work in this dissertation investigates how chemical structure informs vibrational spectroscopy. A major goal of this work was to examine how effective the use of reduced dimensional models is in providing qualitative understanding of the chemical physics of hydrogen bonding while simultaneously providing good agreement with experimental findings. Using the methods developed within this work, the origin of the intensities of transitions to states associated with excitation of the motions of OH bonds has been thoroughly investigated. Throughout this work, it has been shown that a linear expansion of the transition dipole moment fails in capturing the intensity of the transitions investigated. To address this issue, multiple different expansions of the dipole moment have been investigated to understand the origins of the intensity and by exploring which terms are necessary to calculate intensities that capture what is seen in experimental, gas-phase spectra.

In Chapter 2, an investigation into how the anharmonicities and couplings between the OO stretch and OH stretch of a hydronium ion solvated with 1-3 water molecules is conducted. A two-dimensional adiabatic model is developed that is in qualitative agreement with a full two-dimensional study of the systems of interest. More importantly, the adiabatic model allows for deeper investigation into the intensity of the transition to the state with one quantum of excitation in the OH stretch and one quantum of excitation in the OO stretch. This work shows that the largest contributions to the intensity are from the terms in the expansion of the dipole moment function that are porportional to changes in the OH bond length. This finding not only informs the degree to which the dipole expansion must be carried out, but also shows that the intensities of these transitions encode information about the strength of the ionic hydrogen bond.

In Chapters 3 and 4, the transition to the state with one quantum of excitation in the OH stretch and one quantum of excitation in the HOH bend (stretch-bend) is explored. Experimentally this transition is of interest its vibrational band contour in liquid water does not look like a convolution of the two fundamental transitions which it is made up of, which is what one would assume the profile of a multi-quanta transition to look like. In order to better understand this, the experimental profile of the OH stretch in the $H^+(H_2O)_{21}$ cluster was divided by the calculated transitions in that region. Surprisingly, the resulting spectrum was in good agreement with the stretch-bend band profile. This raised many questions into why there was a difference in profile and what structural information could be encoded in this difference. To answer these questions, numerous models were established and tested. This work shows that the largest contribution to the intensity comes from the mixed second derivative of the dipole surface ($\partial^2\mu/\partial\theta_{\mathrm{HOH}}\partial r_{\mathrm{OH}}$), which is insensitive to the hydrogen-bond strength. To further understand this insensitivity, the changes in the charge distribution in H_2O and $(H_2O)_2$ when the OH bond length (r_{OH}) and HOH angle (θ_{HOH}) are displaced from a reference structure. The insensitivity was traced to a partial cancellation between the increase of the partial charges on the hydrogen atoms with increased HOH angle and the decrease in the partial charge on the bound hydrogen atom when the hydrogen bond is broken. In addition to this cancellation of effects, this work also shows that by mode coupling in the vibrational Hamiltonian introduces frequency splittings that lead to spreading of intensity across the region.

In the Chapters 5 and 6, similar reduced dimensional models are applied to the studies of the OH stretching overtones in *tert*-butyl hydroperoxide (TBHP) and a carbon-center hydroperoxyalkyl radical ($^\bullet$QOOH), ie TBHP with a hydrogen removed from one of the methyl groups. Due to the number of vibrations in these molecules, 42 for TBHP and 39 for $^\bullet$QOOH, the reduced dimensional model developed to study these systems also included a reaction path treatment of the remaining vibrations in order to better approximate the potential energy of the molecule. It was concluded that while the breadth of the OH stretch first overtone ($2v_{\mathrm{OH}}$) was present in both TBHP and $^\bullet$QOOH, it was not coming from the

same source. In TBHP, the model showed multiple transitions of the tunneling split states of the double well torsional potential contributing to the breadth, as well as experimental effects. In the case of $^{\bullet}$QOOH, the asymmetric double well torsional potential eliminates most of the tunnelling splitting leading to only one transition that could be making up the $2v_{\mathrm{OH}}$ feature.

While each model used in the studies described in this dissertation is unique to the specific question driving the research of the study, they all have a similar structure. Every model is reduced to the two (or three for $^{\bullet}$QOOH) vibrational degrees of freedom such that the origins of the intensity of a specific multi-quanta transition can be probed. This work shows in cases which a vibrational mode includes a hydrogen-bound OH stretch, a linear dipole approximation does not recover the intensity of the transition. Although in most cases, inclusion of the quadratic terms in the dipole is enough to recover intensity in agreement with experimental findings.

Moving forward, these models can be used to inform work on other multi-quanta transitions involving hydrogen-bonded systems. The insights gained into the necessary terms in the expansions of the potential and dipole surfaces could prove useful in future studies of spectral signatures of hydrogen-bond strength. The various harmonic approaches used in the studies of the stretch-bend transition (Chapter 4) are an excellent example of utilizing electronic structure data to its full potential. Finally, the reaction path formalization presented in the studies of TBHP and $^{\bullet}$QOOH could be applied to other large, atmospherically relevant molecules with the intent of studying the molecule's vibrational spectrum without having to do costly full-dimensional calculations.

The choice of vibrational coordinates and dimensions to be included is an important aspect of this work. Other models created to study vibrations such as the ground state probability amplitude method established in DiRisio *et. al*[48] also show a strong dependence on coordinate choice. Not only is the choice of coordinates used in a study important but also the number of dimensions a model is reduced to. For TBHP the reaction path model presented is qualitatively accurate but studies of a four-dimensional local mode model

produces quantitative results.[34] This is in part due to the increased degrees of freedom in the model, but the model is conducted at the CCSD(T) level of theory which is known to be more accurate then the hybrid-DFT (B2PLYP) level that the reaction path model uses. This presents the question: is the robustness of the vibrational model or the level of theory/basis more important to quantitative accuracy? It would be interesting to understand how the models presented in this dissertation perform when the potential energy and dipole surfaces are obtained using a higher level of theory such as CCSD(T).

This work tests the importance of the inclusion of mechanical and electrical anharmonicities through higher order terms in the potential energy and dipole surface on the simulation of vibrational spectra, particularly with transitions involving OH groups or hydrogen-bonded networks. In every study presented, moving past the linear dipole approximation to account for at least the quadratic terms of the dipole is necessary. Expanding these findings past the systems included in this work, using computations that include this term will yield more accurate results than studies done with a linear approximation. This should also be considered in the development of other methods for simulating spectra. A basis of understanding in the ways in which an intricate problem can be broken down into pieces is established with the primary goal of gaining insights into where post-harmonic treatments are necessary. In a broader sense, these ideas can be applied to a multitude of spectroscopic problems from verification of assignments to predictions of spectral signatures from molecular spectra to predictions of molecular composition from spectral signatures.

BIBLIOGRAPHY

[1] Hale, G. M.; Querry, M. R. *Appl. Opt.* 1973 *12*, 555.

[2] Fournier, J. A.; Johnson, C. J.; Wolke, C. T.; Weddle, G. H.; Wolk, A. B.; Johnson, M. A. *Science* 2014 *344*(6187), 1009–1012.

[3] Frisch, M. J. *et al.* "Gaussian 16 Revision C.01", 2016 Gaussian Inc. Wallingford CT.

[4] Hansen, A. S.; Bhagde, T.; Moore, K. B.; Moberg, D. R.; Jasper, A. W.; Georgievskii, Y.; Vansco, M. F.; Klippenstein, S. J.; Lester, M. I. *Science* 2021 *373*, 679.

[5] Moore, K. B.; Turney, J. M.; Schaefer, H. F. *J. Chem. Phys.* 2017 *146*, 194304.

[6] Western, C. M. *J. Quant. Spectrosc. Radiat. Transf.* 2017 *186*, 221–242.

[7] de Grotthuss, C. J. T. *Ann. Chim. (Paris)* 1806 *LVIII*, 54– 74.

[8] Wilson, E. B.; Decius, J. C.; Cross, P. C. *Molecular Vibrations;* Dover: New York, 1955.

[9] Wolke, C. T.; Fournier, J. A.; Dzugan, L. C.; Fagiani, M. R.; Odbadrakh, T. T.; Knorke, H.; Jordan, K. D.; McCoy, A. B.; Asmis, K. R.; Johnson, M. A. *Science* 2016 *354*(6316), 1131–1135.

[10] McCoy, A. B.; Dzugan, L. C.; DiRisio, R. J.; Madison, L. R. *Faraday Discuss.* 2018 *212*, 443–466.

[11] Headrick, J. M.; Diken, E. G.; Walters, R. S.; Hammer, N. I.; Christie, R. A.; Cui, J.; Myshakin, E. M.; Duncan, M. A.; Johnson, M. A.; Jordan, K. D. *Science* 2005 *308*, 1765–1769.

[12] Napoli, J. A.; Marsalek, O.; Markland, T. E. *J. Chem. Phys.* 2018 *148*(22), 222833.

[13] Duong, C. H.; Yang, N.; Kelleher, P. J.; Johnson, M. A.; DiRisio, R. J.; McCoy, A. B.; Yu, Q.; Bowman, J. M.; Henderson, B. V.; Jordan, K. D. *J. Phys. Chem. A* 2018 *122*(48), 9275–9284.

[14] Xantheas, S. S.; Dunning, T. H. *J. Chem. Phys.* 1993 *99*(11), 8774–8792.

[15] Miliordos, E.; Aprà, E.; Xantheas, S. S. *J. Chem. Phys.* 2013 *139*(11), 114302.

[16] Lee, V. G. M.; Vetterli, N. J.; Boyer, M. A.; McCoy, A. B. *J. Phys. Chem. A* 2020 *124*(34), 6903–6912.

[17] Kjaergaard, H. G.; Garden, A. L.; Chaban, G. M.; Gerber, R. B.; Matthews, D. A.; Stanton, J. F. *J. Phys. Chem. A* 2008 *112*(18), 4324–35.

[18] Yang, N.; Khuu, T.; Mitra, S.; Duong, C. H.; Johnson, M. A.; DiRisio, R. J.; McCoy, A. B.; Miliordos, E.; Xantheas, S. S. *J. Phys. Chem. A* 2020 *124*(50), 10393–10406.

[19] Boyer, M. A.; Marsalek, O.; Heindel, J. P.; Markland, T. E.; McCoy, A. B.; Xantheas, S. S. *J. Phys. Chem. Lett.* 2019 *10*(5), 918–924.

[20] Perakis, F.; De Marco, L.; Shalit, A.; Tang, F. J.; Kann, Z. R.; Kuhne, T. D.; Torre, R.; Bonn, M.; Nagata, Y. *Chem. Rev.* 2016 *116*, 7590.

[21] Møller, C.; Plesset, M. S. *Phys. Rev.* 1934 *46*, 618–622.

[22] Norris, L. S.; Ratner, M. A.; Roitberg, A. E.; Gerber, R. B. *J. Chem. Phys.* 1996 *105*(24), 11261–11267.

[23] Dunning Jr., T. H. *J. Chem. Phys.* 1989 *90*(2), 1007–1023.

[24] McCoy, A. B. *J. Phys. Chem. B* 2014 *118*(28), 8286–8294.

[25] Boyer, M. A.; McCoy, A. B. *J. Chem. Phys.* 2022 *156*(5), 054107.

[26] Werner, H.-J. *et al.* "MOLPRO, version 2012.1, a package of ab initio programs", 2012.

[27] Finney, J.; Choi, T. H.; Huchmala, R.; Heindel, J.; Xantheas, S.; Jordan, K.; McCoy, A. *J. Phys. Chem. Lett.* 2023 *14*, 4666–4672.

[28] Hammer, N. I.; Diken, E. G.; Roscioli, J. R.; Johnson, M. A.; Myshakin, E. M.; Jordan, K. D.; McCoy, A. B.; Huang, X.; Bowman, J. M.; Carter, S. *J. Chem. Phys.* 2005 *122*(24), 244301.

[29] Duong, C. H.; Yang, N.; Johnson, M. A.; DiRisio, R. J.; McCoy, A. B.; Yu, Q.; Bowman, J. M. *J. Phys. Chem. A* 2019 *123*(37), 7965–7972.

[30] Huchmala, R. M.; McCoy, A. B. *J. Phys. Chem. A* 2022 *126*(8), 1360–1368 PMID: 35171593.

[31] Yang, N.; Huchmala, R. M.; McCoy, A. B.; Johnson, M. A. *J. Phys. Chem. Lett.* 2022 *13*(34), 8116–8121 PMID: 35998327.

[32] Hansen, A. S.; Huchmala, R. M.; Vogt, E.; Boyer, M. A.; Bhagde, T.; Vansco, M. F.; Jensen, C. V.; Kjærsgaard, A.; Kjaergaard, H. G.; McCoy, A. B.; Lester, M. I. *J. Chem. Phys.* 2021 *154*(16), 164306.

[33] Miller, W. H.; Handy, N. C.; Adams, J. E. *J. Chem. Phys.* 1980 *72*, 99–112.

[34] Vogt, E.; Huchmala, R. M.; Jensen, C. V.; Boyer, M. A.; Wallberg, J.; Hansen, A. S.; Kjærsgaard, A.; Lester, M. I.; McCoy, A. B.; Kjaergaard, H. G. *J. Chem. Phys.* 2021 *154*(16), 164307.

[35] Hansen, A. S.; Bhagde, T.; Qian, Y.; Cavazos, A.; Huchmala, R. M.; Boyer, M. A.; Gavin-Hanner, C. F.; Klippenstein, S. J.; McCoy, A. B.; Lester, M. I. *J. Chem. Phys.* 2022 *156*(1), 014301.

[36] Headrick, J. M.; Diken, E. G.; Walters, R. S.; Hammer, N. I.; Christie, R. A.; Cui, J.; Myshakin, E. M.; Duncan, M. A.; Johnson, M. A.; Jordan, K. D. *Science* 2005 *308*(5729), 1765–1769.

[37] Ishii, K.; Takeuchi, S.; Tahara, T. *J. Chem. Phys.* 2009 *131*(4), 044512.

[38] Zhou, S.; Wang, L. *Chem. Sci.* 2019 *10*, 7734–7745.

[39] McCoy, A. B.; Guasco, T. L.; Leavitt, C. M.; Olesen, S. G.; Johnson, M. A. *Phys. Chem. Chem. Phys.* 2012 *14*, 7205–7214.

[40] Roscioli, J. R.; Diken, E. G.; Johnson, M. A.; Horvath, S.; McCoy, A. B. *J. Phys. Chem. A* 2006 *110*(15), 4943–4952.

[41] Ayotte, P.; Weddle, G. H.; Kim, J.; Johnson, M. A. *J. Am. Chem. Soc.* 1998 *120*(47), 12361–12362.

[42] Verner, M. V.; Kuhn, O.; Sauer, J. *J. Chem. Phys.* 2001 *114*, 240–249.

[43] Myshakin, E. M.; Jordan, K. D.; Sibert, E. L.; Johnson, M. A. *J. Chem. Phys.* 2003 *119*(19), 10138–10145.

[44] Henderson, E. V.; Jordan, K. D. *J. Phys. Chem. Lett.* 2021 *12*(27), 6326–6329.

[45] Yang, N.; Duong, C. H.; Kelleher, P. J.; Johnson, M. A. *Nature Chemistry* 2020 *12*(2), 159–164.

[46] Douberly, G. E.; Walters, R. S.; Cui, J.; Jordan, K. D.; Duncan, M. A. *J. Phys. Chem. A* 2010 *114*(13), 4570–4579.

[47] Vendrell, O.; Gatti, F.; Meyer, H.-D. *J. Chem. Phys.* 2007 *127*, 184303.

[48] DiRisio, R. J.; Finney, J. M.; Dzugan, L. C.; Madison, L. R.; McCoy, A. B. *J. Phys. Chem. A* 2021 *125*(33), 7185–7197.

[49] Frisch, M. J. *et al.* "Gaussian 09 Revision D.01", Gaussian, Inc., Wallingford, CT 2009.

[50] Colbert, D. T.; Miller, W. H. *J. Chem. Phys.* 1992 *96*, 1982–1991.

[51] Hamm, P.; Stock, G. *J. Chem. Phys.* 2015 *143*(13), 134308.

[52] Relph, R. A.; Elliott, B. M.; Weddle, G. H.; Johnson, M. A.; Ding, J.; Jordan, K. D. *J. Phys. Chem. A* 2009 *113*(6), 975–981.

[53] Heine, N.; Kratz, E. G.; Bergmann, R.; Schofield, D. P.; Asmis, K. R.; Jordan, K. D.; McCoy, A. B. *J. Phys. Chem. A* 2014 *118*(37), 8188–8197.

[54] Gerardi, H. K.; DeBlase, A. F.; Su, X.; Jordan, K. D.; McCoy, A. B.; Johnson, M. A. *J. Phys. Chem. Lett.* 2011 *2*, 2437–2441.

[55] Mosley, J. D.; Cheng, T. C.; McCoy, A. B.; Duncan, M. A. *J. Phys. Chem. A* 2012 *116*(37), 9287–9294.

[56] Esser, T. K.; Knorke, H.; Asmis, K. R.; Schöllkopf, W.; Yu, Q.; Qu, C.; Bowman, J. M.; Kaledin, M. *J. Phys. Chem. Lett.* 2018 *9*(4), 798–803.

[57] Duong, C. H.; Gorlova, O.; Yang, N.; Kelleher, P. J.; Johnson, M. A.; McCoy, A. B.; Yu, Q.; Bowman, J. M. *J. Phys. Chem. Lett.* 2017 *8*(16), 3782–3789.

[58] Kananenka, A. A.; Skinner, J. L. *Phys. Chem. Chem. Phys.* 2020 *22*, 18124.

[59] Tainter, C. J.; Ni, Y.; Shi, L.; Skinner, J. L. *J. Phys. Chem. Lett.* 2013 *4*, 12.

[60] Medders, G. R.; Paesani, F. *J. Chem. Theory Comput.* 2015 *11*, 1145.

[61] Schmidt, J. R.; Roberts, S. T.; Loparo, J. J.; Tokmakoff, A.; Fayer, M. D.; Skinner, J. L. *Chem. Phys.* 2007 *341*, 143.

[62] Gruenbaum, S. M.; Tainter, C. J.; Shi, L.; Ni, Y.; Skinner, J. L. *J. Chem. Theory Comput.* 2013 *9*(7), 3109–3117 PMID: 26583990.

[63] Kananenka, A. A.; Skinner, J. L. *J. Chem. Phys.* 2018 *148*(24), 244107.

[64] Ohno, K.; Okimura, M.; Akai, N.; Katsumoto, Y. *Phys. Chem. Chem. Phys.* 2005 *7*, 3005–3014.

[65] Kebede, G. G.; Mitev, P. D.; Briels, W. J.; Hermansson, K. *Phys. Chem. Chem. Phys.* 2018 *20*, 12678.

[66] Yang, N.; Duong, C. H.; Kelleher, P. J.; Johnson, M. A.; McCoy, A. B. *Chem. Phys. Lett.* 2017 *690*, 159 – 171.

[67] Waggener, W. C. *Anal. Chem.* 1958 *30*, 1569.

[68] Libnau, F. O.; Kvalheim, O. M.; Christy, A. A.; Toft, J. *Vib. Spectrosc.* 1994 *7*, 243.

[69] Fournier, J. A.; Wolke, C. T.; Johnson, C. J.; Johnson, M. A.; Heine, N.; Gewinner, S.; Schöllkopf, W.; Esser, T. K.; Fagiani, M. R.; Knorke, H.; Asmis, K. R. *Proceedings of the National Academy of Sciences* 2014 *111*(51), 18132–18137.

[70] Perchard, J. P. *Chem. Phys.* 2001 *273*, 217.

[71] Wu, C. C.; Chaudhuri, C.; Jiang, J. C.; Lee, Y. T.; Chang, H. C. *J. Chin. Chem. Soc-Taip* 2002 *49*, 769.

[72] Nizkorodov, S. A.; Ziemkiewicz, M.; Nesbitt, D. J.; Knight, A. E. W. *J. Chem. Phys.* 2005 *122*, 194316.

[73] McDonald, D. C.; Wagner, J. P.; Duncan, M. A. *J. Chem. Phys.* 2018 *149*(3), 031105.

[74] Cyran, J. D.; Backus, E. H. G.; Nagata, Y.; Bonn, M. *J. Phys. Chem. B* 2018 *122*, 3667.

[75] Schaefer, J.; Backus, E. H. G.; Nagata, Y.; Bonn, M. *J. Phys. Chem. Lett.* 2016 *7*, 4591.

[76] Inoue, K.; Nihonyanagi, S.; Singh, P. C.; Yamaguchi, S.; Tahara, T. *J. Chem. Phys.* 2015 *142*, 212431.

[77] Nihonyanagi, S.; Kusaka, R.; Inoue, K.; Adhikari, A.; Yamaguchi, S.; Tahara, T. *J. Chem. Phys.* 2015 *143*, 124707.

[78] Du, Q.; Superfine, R.; Freysz, E.; Shen, Y. R. *Phys. Rev. Lett.* 1993 *70*, 2313.

[79] Yang, N.; Edington, S. C.; Choi, T. H.; Henderson, E. V.; Heindel, J. P.; Xantheas, S. S.; Jordan, K. D.; Johnson, M. A. *P. Natl. Acad. Sci. USA* 2020 *117*, 26047.

[80] Schulz, F.; Hartke, B. *ChemPhysChem* 2002 *3*, 98.

[81] Kirov, M. V.; Fanourgakis, G. S.; Xantheas, S. S. *Chem. Phys. Lett.* 2008 *461*, 180.

[82] Rakshit, A.; Bandyopadhyay, P.; Heindel, J. P.; Xantheas, S. S. *J. Chem. Phys.* 2019 *151*, 214307.

[83] Liu, J.; Yang, J.; Zeng, X. C.; Xantheas, S. S.; Yagi, K.; He, X. *Nat. Commun.* 2021 *12*, 6141.

[84] Hermansson, K. *Int. J. Quantum Chem.* 1993 *45*(6), 747–758.

[85] Paolo, T. D.; Bourdéron, C.; Sandorfy, C. *Can. J. Chem.* 1972 *50*, 3161.

[86] Howard, D. L.; Kjærgaard, H. G. *J. Phys. Chem. A* 2006 *110*, 10245.

[87] Hermansson, K. *J. Chem. Phys.* 1993 *99*(2), 861–868.

[88] Bakker, H. J.; Skinner, J. L. *Chemical Reviews* 2010 *110*(3), 1498–1517.

[89] Skinner, J. L.; Auer, B. M.; Lin, Y.-S. *Adv. Chem. Phys.* 2008 *142*, 59–103.

[90] Yang, N.; Duong, C. H.; Kelleher, P. J.; McCoy, A. B.; Johnson, M. A. *Science* 2019 *364*(6437), 275–278.

[91] Ni, Y.; Skinner, J. L. *J. Chem. Phys.* 2015 *143*(1) 014502.

[92] Fox, J. J.; Martin, A. E. *Proc. R. Soc. Lond. A* 1940 *174*(957), 234–262.

[93] Eisenberg, D. S.; Kauzmann, W. *The Structure and Properties of Water;* Oxford University Press: Oxford, United Kingdom, 1st ed.; 1969.

[94] Matthews, J.; Sinha, A.; Francisco, J. S. *J. Chem. Phys.* 2004 *120*, 10543–10553.

[95] Gardenier, G. H.; Johnson, M. A.; McCoy, A. B. *J. Phys. Chem. A* 2009 *113*(16), 4772–4779.

[96] Kjaergaard, H. G.; Low, G. R.; Robinson, T. W.; Howard, D. L. *J. Phys. Chem. A* 2002 *106*(38), 8955–8962.

[97] Whitney, E. S.; Haeber, T.; Schuder, M. D.; Blair, A. C.; Nesbitt, D. J. *J. Chem. Phys.* 2006 *125*(5) 054303.

[98] Kortyna, A.; Doney, K.; Nesbitt, D. J. *J. Chem. Phys.* 2020 *152*(13) 134305.

[99] Fanourgakis, G. S.; Xantheas, S. S. *The Journal of Chemical Physics* 2006 *124*(17) 174504.

[100] Fanourgakis, G. S.; Xantheas, S. S. *jcp* 2008 *128*(7), 074506.

[101] Zádor, J.; Taatjes, C. A.; Fernandes, R. X. *Prog. Energy Combust. Sci.* 2011 *37*, 371.

[102] Osborn, D. L. *Annu. Rev. Phys. Chem.* 2017 *68*, 233.

[103] Orlando, J. J.; Tyndall, G. S. *Chem. Soc. Rev.* 2012 *41*, 6294.

[104] Zádor, J.; Huang, H.; Welz, O.; Zetterberg, J.; Osborn, D. L.; Taatjes, C. A. *Phys. Chem. Chem. Phys.* 2013 *15*, 10753.

[105] Savee, J. D.; Papajak, E.; Rotavera, B.; Huang, H.; Eskola, A. J.; Welz, O.; Sheps, L.; Taatjes, C. A.; Zádor, J.; Osborn, D. L. *Science* 2015 *347*, 643.

[106] Bugler, J.; Power, J.; Curran, H. J. *Proc. Combust. Inst.* 2017 *36*, 161.

[107] Goldsmith, C. F.; Green, W. H.; Klippenstein, S. J. *J. Phys. Chem. A* 2012 *116*, 3325.

[108] Nozière, B.; Vereecken, L. *Angew.Chem. Int. Ed.* 2019 *58*, 13976.

[109] Carr, S. A.; Glowacki, D. R.; Liang, C.; Baeza-Romero, M. T.; Blitz, M. A.; Pilling, M. J.; Seakins, P. W. *J. Phys. Chem. A* 2011 *115*, 1069.

[110] Weidman, J. D.; Allen, R. T.; Moore, K. B.; Schaefer, H. F. *J. Chem. Phys.* 2018 *148*, 184308.

[111] Davis, M. M.; Weidman, J. D.; Abbott, A. S.; Douberly, G. E.; Turney, J. M.; F., S. H. *J. Chem. Phys.* 2019 *151*, 124302.

[112] Miyoshi, A. *J. Phys. Chem. A* 2011 *115*, 3301.

[113] Oguchi, T.; Miyoshi, A.; Koshi, M.; Matsui, H.; Washida, N. *J. Phys. Chem. A* 2001 *105*, 378.

[114] Sharma, S.; Raman, S.; Green, W. H. *J. Phys. Chem. A* 2010 *114*, 5689.

[115] Asatryan, R.; Bozzelli, J. W. *J. Phys. Chem. A* 2010 *114*, 7693.

[116] Wang, Z.; Zhang, L.; Moshammer, K.; Popolan-Vaida, D. M.; Shankar, V. S. B.; Lucassen, A.; Hemken, C.; Taatjes, C. A.; Leone, S. R.; Kohse-Höinghaus, K.; Hansen, N.; Dagaut, P.; Sarathy, S. M. *Combust. Flame* 2016 *164*, 386.

[117] Wang, Z.; Sarathy, S. M. *Combust. Flame* 2016 *165*, 364.

[118] Crounse, J. D.; Knap, H. C.; ørnsø, K. B.; Jørgensen, S.; Paulot, F.; Kjaergaard, H. G.; Wennberg, P. O. *J. Phys. Chem. A* 2012 *116*, 5756.

[119] Whelan, C. A.; Blitz, M. A.; Shannon, R.; Onel, L.; Lockhart, J. P.; Seakins, P. W.; Stone, D. *J. Phys. Chem. A* 2019 *123*, 10254.

[120] Scheer, A. M.; Welz, O.; Zádor, J.; Osborn, D. L.; Taatjes, C. A. *Phys. Chem. Chem. Phys.* 2014 *16*, 13027.

[121] Eskola, A. J.; Welz, O.; Zádor, J.; Antonov, I. O.; Sheps, L.; Savee, J. D.; Osborn, D. L.; Taatjes, C. A. *Proc. Combust. Inst.* 2015 *35*, 291.

[122] Koritzke, A. L.; Davis, J. C.; Caravan, R. L.; Christianson, M. G.; Osborn, D. L.; Taatjes, C. A.; Rotavera, B. *Proc. Combust. Inst.* 2019 *37*, 323.

[123] Chen, C. J.; Bozzelli, J. W. *J. Phys. Chem. A* 1999 *103*, 9731.

[124] DeSain, J. D.; Ho, A. D.; Taatjes, C. A. *J. Mol. Spectrosc.* 2003 *219*, 163.

[125] Ticich, T. M.; Likar, M. D.; Dübal, H.; Butler, L. J.; Crim, F. F. *J. Chem. Phys.* 1987 *87*(10), 5820–5829.

[126] Likar, M. D.; Baggott, J. E.; Crim, F. F. *J. Chem. Phys.* 1989 *90*(11), 6266–6274.

[127] Barone, V. *J. Chem. Phys.* 2005 *122*, 014108.

[128] Frederick, J. H.; Woywod, C. *J. Chem. Phys.* 1999 *111*(16), 7255–7271.

[129] Beames, J. M.; Liu, F.; Lu, L.; Lester, M. I. *J. Am. Chem. Soc.* 2012 *134*, 20045.

[130] Hsieh, S.; Vushe, R.; Tun, Y. T.; Vallejo, J. L. *Chem. Phys. Lett.* 2014 *591*, 99.

[131] Matthews, J.; Martínez-Avilés, M.; Francisco, J. S.; Sinha, A. *J. Chem. Phys.* 2008 *129*, 074316.

[132] Liu, F.; Beames, J. M.; Petit, A. S.; McCoy, A. B.; Lester, M. I. *Science* 2014 *345*(6204), 1596–1598.

[133] Liu, F.; Beames, J. M.; Lester, M. I. *J. Chem. Phys.* 2014 *141*, 234312.

[134] Barber, V. P.; Pandit, S.; Esposito, V. J.; McCoy, A. B.; Lester, M. I. *J. Phys. Chem. A* 2019 *123*, 2559.

[135] Grimme, S.; Antony, J.; Ehrlich, S.; Krieg, H. *J. Chem. Phys.* 2010 *132*, 154104.

[136] Hanst, P. L.; Gay, B. W. *Atmos. Environ. (1967)* 1983 *17*(11), 2259–2265.

[137] Crounse, J. D.; Nielsen, L. B.; Jørgensen, S.; Kjaergaard, H. G.; Wennberg, P. O. *J. Phys. Chem. Lett.* 2013 *4*(20), 3513–3520.

[138] Bonn, B.; von Kuhlmann, R.; Lawrence, M. G. *Geophys. Res. Lett.* 2004 *31*(10).

[139] Docherty, K. S.; Wu, W.; Lim, Y. B.; Ziemann, P. J. *Environ. Sci. Technol.* 2005 *39*(11), 4049–4059.

[140] Bianchi, F. *et al. Chem. Rev.* 2019 *119*(6), 3472–3509.

[141] Praske, E.; Otkjær, R. V.; Crounse, J. D.; Hethcox, J. C.; Stoltz, B. M.; Kjaergaard, H. G.; Wennberg, P. O. *Proc. Natl. Acad. Sci.* 2018 *115*(1), 64–69.

[142] Fu, D.; Millet, D. B.; Wells, K. C.; Payne, V. H.; Yu, s.; Guenther, A.; Eldering, A. *Nat. Commun.* 2019 *10*(1), 1–12.

[143] Brown, S. S. *Chem. Rev.* 2003 *103*(12), 5219–5238.

[144] Fry, J. L.; Matthews, J.; Lane, J. R.; Roehl, C. M.; Sinha, A.; Kjaergaard, H. G.; Wennberg, P. O. *J. Phys. Chem. A* 2006 *110*(22), 7072–7079.

[145] Closser, K. D.; Vogelhuber, K. M.; Hsieh, S. *J. Phys. Chem. A* 2008 *112*(6), 1238–1244.

[146] Chandler, D. W.; Farneth, W. E.; Zare, R. N. *J. Chem. Phys.* 1982 *77*(9), 4447–4458.

[147] Homitsky, S. C.; Dragulin, S. M.; Haynes, L. M.; Hsieh, S. *J. Phys. Chem. A* 2004 *108*(44), 9492–9499.

[148] Matthews, J.; Martínez-Avilés, M.; Francisco, J. S.; Sinha, A. *J. Chem. Phys.* 2008 *129*(7), 074316.

[149] Chuang, M.-C.; Baggott, J. E.; Chandler, D. W.; Farneth, W. E.; Zare, R. N. *Faraday Discuss. Chem. Soc.* 1983 *75*, 301–313.

[150] Barone, V. *J. Chem. Phys.* 2005 *122*(1), 014108.

[151] Barone, V.; Biczysko, M.; Bloino, J. *Phys. Chem. Chem. Phys.* 2014 *16*, 1759–1787.

[152] Dübal, H. R.; Crim, F. F. *J. Chem. Phys.* 1985 *83*(8), 3863–3872.

[153] Schofield, D. P.; Kjaergaard, H. G.; Matthews, J.; Sinha, A. *J.Chem. Phys.* 2005 *123*(13), 134318.

[154] McCoy, A. B.; Sprague, M. K.; Okumura, M. *J. Phys. Chem. A* 2010 *114*(3), 1324–1333.

[155] Eckart, C. *Phys. Rev.* 1935 *47*, 552–558.

[156] Krasnoshchekov, S. V.; Isayeva, E. V.; Stepanov, N. F. *J. Chem. Phys.* 2014 *140*(15), 154104.

[157] Pickett, H. M. *J. Chem. Phys.* 1972 *56*(4), 1715–1723.

[158] Lauvergnat, D.; Luis, J. M.; Kirtman, B.; Reis, H.; Nauts, A. *J. Chem. Phys.* 2016 *144*(8), 084116.

[159] Fehrensen, B.; Luckhaus, D.; Quack, M. *Chem. Phys.* 2007 *338*(2), 90–105.

[160] Vogt, E.; Bertran Valls, P.; Kjaergaard, H. G. *J. Phys. Chem. A* 2020 *124*(5), 932–942.

[161] Halonen, L.; Carrington, T. *J. Chem. Phys.* 1988 *88*(7), 4171–4185.

[162] Adler, T. B.; Knizia, G.; Werner, H.-J. *J. Chem. Phys.* 2007 *127*(22), 221106.

[163] Peterson, K. A.; Adler, T. B.; Werner, H.-J. *J. Chem. Phys.* 2008 *128*(8), 084102.

[164] Sahetchian, K.; Rigny, R.; Tardieu de Maleissye, J.; Batt, L.; Anwar Khan, M.; Mathews, S. *Proc. Combust. Inst.* 1992 *24*(1), 637–643.

[165] Wijaya, C. D.; Sumathi, R.; Green, W. H. *J. Phys. Chem. A* 2003 *107*(24), 4908–4920.

[166] Simmie, J. M.; Black, G.; Curran, H. J.; Hinde, J. P. *J. Phys. Chem. A* 2008 *112*(22), 5010–5016.

[167] Ryu, B.-G.; Park, C. R.; Lee, Y.; Shin, S. K.; Kim, H. L. *J. Photochem. Photobiol. A* 2002 *149*(1), 15–21.

[168] Bach, R. D.; Schlegel, H. B. *J. Phys. Chem. A* 2020 *124*(23), 4742–4751.

[169] Reints, W.; Pratt, D. A.; Korth, H.-G.; Mulder, P. *J. Phys. Chem. A* 2000 *104*(46), 10713–10720.